

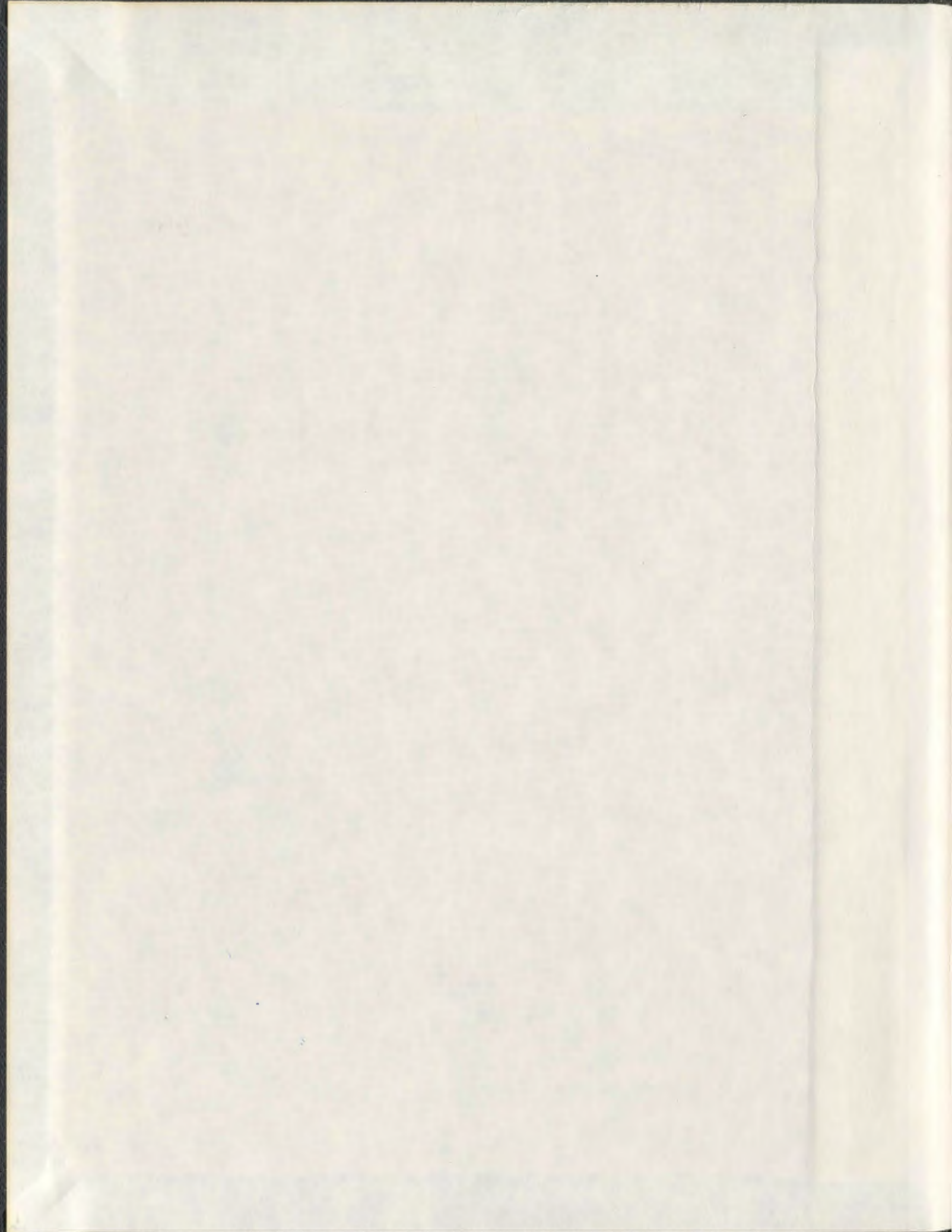
ELASTIC CONSTANTS OF PHASES III, V AND VI  
OF ICE BY BRILLOUIN SPECTROSCOPY

CENTRE FOR NEWFOUNDLAND STUDIES

**TOTAL OF 10 PAGES ONLY  
MAY BE XEROXED**

(Without Author's Permission)

CHRIS A. TULK



001311





## **INFORMATION TO USERS**

**This manuscript has been reproduced from the microfilm master. UMI films the text directly from the original or copy submitted. Thus, some thesis and dissertation copies are in typewriter face, while others may be from any type of computer printer.**

**The quality of this reproduction is dependent upon the quality of the copy submitted. Broken or indistinct print, colored or poor quality illustrations and photographs, print bleedthrough, substandard margins, and improper alignment can adversely affect reproduction.**

**In the unlikely event that the author did not send UMI a complete manuscript and there are missing pages, these will be noted. Also, if unauthorized copyright material had to be removed, a note will indicate the deletion.**

**Oversize materials (e.g., maps, drawings, charts) are reproduced by sectioning the original, beginning at the upper left-hand corner and continuing from left to right in equal sections with small overlaps. Each original is also photographed in one exposure and is included in reduced form at the back of the book.**

**Photographs included in the original manuscript have been reproduced xerographically in this copy. Higher quality 6" x 9" black and white photographic prints are available for any photographs or illustrations appearing in this copy for an additional charge. Contact UMI directly to order.**

# **UMI**

**A Bell & Howell Information Company  
300 North Zeeb Road, Ann Arbor MI 48106-1346 USA  
313/761-4700 800/521-0600**

**Elastic Constants of Phases III, V and VI  
of Ice by Brillouin Spectroscopy**

**By**

**© Chris A. Tulk, B.Sc. (Hons.)**

**A Thesis Submitted to the School of Graduate  
Studies in Partial Fulfillment of the  
Requirements for the Degree of  
Doctor of Philosophy**

**Department of Physics and Physical Oceanography  
Memorial University of Newfoundland**

**July 1996**

**St. John's**

**Newfoundland**



National Library  
of Canada

Acquisitions and  
Bibliographic Services

395 Wellington Street  
Ottawa ON K1A 0N4  
Canada

Bibliothèque nationale  
du Canada

Acquisitions et  
services bibliographiques

395, rue Wellington  
Ottawa ON K1A 0N4  
Canada

*Your file Votre référence*

*Our file Notre référence*

The author has granted a non-exclusive licence allowing the National Library of Canada to reproduce, loan, distribute or sell copies of this thesis in microform, paper or electronic formats.

The author retains ownership of the copyright in this thesis. Neither the thesis nor substantial extracts from it may be printed or otherwise reproduced without the author's permission.

L'auteur a accordé une licence non exclusive permettant à la Bibliothèque nationale du Canada de reproduire, prêter, distribuer ou vendre des copies de cette thèse sous la forme de microfiche/film, de reproduction sur papier ou sur format électronique.

L'auteur conserve la propriété du droit d'auteur qui protège cette thèse. Ni la thèse ni des extraits substantiels de celle-ci ne doivent être imprimés ou autrement reproduits sans son autorisation.

0-612-23110-0

## Abstract

Large ( $\sim 0.3 \text{ cm}^3$ ) high quality single crystal samples of  $\text{H}_2\text{O}$  ice III, Ice V, and Ice VI have been produced in a high pressure cell. The cell was pressurized by means of hydraulic fluid and specifically designed so that the samples could be rotated about the vertical without having to reduce the pressure. Liquid water was initially placed inside the sample containment cell and the pressure increased at room temperature. The temperature was then reduced to approximately  $-35^\circ\text{C}$ . After several hours the supercooled water sample froze directly into the desired phase, depending on the pressure. The frozen sample was then partially melted until only a small seed comprised of a few grains remained. After a controlled refreeze large grained polycrystals were produced; successive iterations of this process eventually yielded small single crystal seeds, from which large high quality single crystals were grown. Once produced, samples were kept under pressure at constant temperature and acoustic data collected using Brillouin spectroscopy at several crystallographic orientations. In all, measurements were collected from three single crystals of ice III (tetragonal), three single crystals of Ice V (monoclinic) and four single crystals of Ice VI (tetragonal).

The elastic constants were fitted to the acoustic data by making use of the Christoffel determinant and the Brillouin equation. Six independent elastic constants of ice III were determined between 2.2 and 3.0 Kbar. At  $-20^\circ\text{C}$ , and 2.2 Kbar the values were found to be  $C_{11}=15.37$ ,  $C_{12}=9.95$ ,  $C_{13}=6.51$ ,  $C_{33}=11.55$ ,  $C_{44}=4.46$ ,  $C_{55}=5.68$  ( $\times 10^4 \text{ bar}$ ). Thirteen independent elastic constants of ice V were determined at 3.0 kbar and  $-35^\circ\text{C}$ , and were

found to be  $C_{11}=21.4$ ,  $C_{22}=19.3$ ,  $C_{33}=21.1$ ,  $C_{44}=7.5$ ,  $C_{55}=3.7$ ,  $C_{66}=7.5$ ,  $C_{12}=12.2$ ,  $C_{13}=9.5$ ,  $C_{15}=0.17$ ,  $C_{23}=11.8$ ,  $C_{25}=0.1$ ,  $C_{35}=0.3$ ,  $C_{46}=2.1$  ( $\times 10^4$  bar). Six independent elastic constants of ice VI were determined between 6.2 and 8.2 kbar at  $-2^\circ\text{C}$ , the values at 7.2 kbar were found to be  $C_{11}=26.84$ ,  $C_{12}=14.52$ ,  $C_{13}=12.82$ ,  $C_{33}=26.21$ ,  $C_{44}=6.31$ ,  $C_{55}=10.38$  ( $\times 10^4$  bar).

The isotropic elastic properties of polycrystalline aggregates of ice III, V and VI were also calculated. The elastic constants were used to calculate the acoustic velocity in many crystallographic directions covering  $4\pi$  steradians, the average longitudinal acoustic velocity was then found by performing a weighted average over all crystallographic directions. The bulk modulus was calculated using either elastic constant values or the compliance constant values. The average longitudinal acoustic velocity and the bulk Modulus enabled the calculation of Young's modulus, Lamé constants, average transverse acoustic velocity and Poisson's ratio. These are easily compared with similar values calculated from the acoustic velocity and bulk modulus as measured directly from polycrystalline samples. In all cases the agreement is excellent.

## **Acknowledgements**

There are several individuals who have helped see this set of experiments through to completion and deserve my gratitude.

First of all I would like to thank my supervisory committee members, Drs. H. Kiefte, M. J. Clouter and R. E. Gagnon. They have been kind enough to share wisdom which helped solve problems that I thought could not be solved. They have shown patience when I made mistakes and built confidence with praise during my successes.

I would also like to thank Dr. E. Svensson and the Atomic Energy of Canada Limited for allowing me to share in neutron scattering experiments at Chalk River Laboratories.

The National Research Council of Canada / Institute for Marine Dynamics provided the water samples for these experiments. In the early stage of these experiments NRC provided a room at the Institute for Marine Dynamics so that I could work closely with Dr. R. E. Gagnon to develop the crystal growth technique.

Members of this research group have always given useful advice during our many intense discussions of our experimental problems. I would particularly like to thank, Mr. E. Grigoriantz, Mr. T. Andrews, Dr. R. Goulding, Mr. O. Vasquez, and Mrs. C. Fan.

Finally I would like to thank my family for their constant support. My parents Leo and Judy Tulk and my sister Natelle have always been there for me. For as long as I can remember they have encouraged me to pursue my interests. They have given me two of life's most important assets, the courage to face my fears, and the determination to forge ahead. My wife Kelly, in addition to proof reading this manuscript, has shown an understanding of the amount of time and effort required to finish this work. Kelly has always helped me, and sometimes made me, take the next step when taking the next step seemed impossible. Her patience has not gone unnoticed.

Without my family this work would have not been completed, this thesis is dedicated to them. They have my unending gratitude.

# Table of Contents

<b>Abstract</b>	ii
<b>Acknowledgements</b>	iv
<b>Table of Contents</b>	vi
<b>List of Tables</b>	viii
<b>List of Figures</b>	ix
<b>List of Symbols</b>	x
<b>1 Introduction to Water and Ice</b>	<b>1</b>
<b>1.1 Introduction</b>	1
1.1.1 Water Molecule	4
<b>1.2 High Pressure Phases of Ice</b>	8
1.2.1 Ice III	12
1.2.2 Ice V	15
1.2.3 Ice VI	15
<b>2 Elastic Theory, Brillouin Spectroscopy and Experimental Set-Up</b>	<b>18</b>
<b>2.1 Elastic Theory</b>	18
2.1.1 Stress and Strain	18
2.1.2 Equations of Motion	22
2.1.3 Polycrystalline Elastic Properties	27
<b>2.2 Brillouin Spectroscopy</b>	30
2.2.1 Introduction	30
2.2.2 Brillouin Equation	32
<b>2.3 Experimental Apparatus</b>	36
2.3.1 High Pressure Cell	41
2.3.2 Fabry-Perot Interferometer	49
<b>3 Single Crystal Growth and The Elastic Constants of Ice III</b>	<b>53</b>
<b>3.1 Determination of the Elastic Constants</b>	53
3.1.1 Density and Refractive Index of Ice III	54
3.1.2 Euler Angles	56
3.1.3 Determination of Sample Orientation	59
3.1.4 Fitting The Elastic Constants	63
<b>3.2 Growth of Single Crystal Samples</b>	70
3.2.1 Ice III	72

<b>3.3 Results of Ice III Studies</b>	75
3.3.1 Frequency Shift Data and The Elastic Constants of ice III	75
3.3.2 Derived Polycrystalline Elastic Properties	101
<b>4 Single Crystal Growth and the Elastic Constants of Ice V</b>	105
<b>4.1 Ice V</b>	105
4.1.1 Orientation Problems	105
4.1.2 Density and Refractive Index	108
<b>4.2 Crystal Growth and Results</b>	109
4.2.1 Growth of Ice V Single Crystals	109
4.2.2 Frequency Shift Data and The Elastic Constants of Ice V	114
4.2.3 Derived Polycrystalline Elastic Properties	131
<b>5 Single Crystal Growth and The Elastic Constants of Ice VI</b>	134
<b>5.1 Ice VI</b>	134
5.1.1 Introduction	134
<b>5.2 Density, Refractive Index and Euler Angles         of Ice VI</b>	136
5.2.1 Density and Refractive Index	136
5.2.2 Euler Angles	137
<b>5.3 Growth of Single Crystals of Ice VI</b>	145
5.3.1 Crystal Growth	146
<b>5.4 Results of Ice VI Studies</b>	148
5.4.1 Frequency Shift Data and The Elastic Constants of Ice VI	151
5.4.2 Derived Polycrystalline Elastic Properties	171
<b>6 Conclusions</b>	181
<b>6.1 Experimental Difficulties</b>	181
6.1.1 Determination of Crystal Growth Procedure	181
6.1.2 Efforts to Grow Single Crystals of Ice II	184
<b>6.2 Results</b>	188
<b>References</b>	194
<b>Appendix A</b>	A1
<b>Appendix B</b>	B1

## List of Tables

1.1 Structure Data of The Ice Polymorphs	13
3.1 Extinction Angle Versus Crystal Orientation, Ice III	64
3.2 Brillouin Frequency Shift Data, Ice III	81
3.3 Elastic Constants of Ice III	93
3.4 Elastic Constants, Density and Refractive Index at Various Pressures, Ice III	94
3.5 Elastic Properties of Isotropic Polycrystalline Ice III	102
4.1 Brillouin Frequency Shift Data, Ice V	117
4.2 Elastic Constants of Ice V	127
4.3 Elastic Properties of Isotropic Polycrystalline Ice V	132
5.1 Extinction Angle Verses Crystal Orientation, Ice VI	138
5.2 Brillouin Frequency Shifts, Ice VI	154
5.3 Elastic Constants of Ice VI	168
5.4 Elastic Constants, Density, and Refractive Index in the Pressure Range 6.2-8.2 kbar, Ice VI	170
5.5 Elastic Properties of Isotropic Polycrystalline Ice VI	174
6.1 Elastic Constants of Ice III, V and VI	189
A1 Extinction Angle Verses Crystal Orientation, Ice V	A2

## List of Figures

1.1 Bernal-Fowler Ice Rules	6
1.2 Phase Diagram of Ice	9
2.1 Elemental Volume Illustrating Stress Components	23
2.2 Bragg's Law	34
2.3 Experimental Set-Up	37
2.4 High Pressure Cell	42
2.5 Sample Containment Cell	45
3.1 Euler Angles Relating Laboratory Frame of Reference to Crystallographic Frame	57
3.2 Birefringent Extinction in Uniaxial Crystals	61
3.3 Extinction Angle Plotted Against $\Delta\phi$	65
3.4 Growth of a Single Crystal of Ice III	76
3.5 Typical Brillouin Spectrum Collected From Ice III	79
3.6 Frequency Shift Verses $\Delta\phi$ for Ice III, crystal #1 and #2	86
3.7 Frequency Shift Curves at 2.5, 2.8, and 3.0 kbar	90
3.8 Elastic Constants of Ice III as Function of Pressure	95
3.9 Acoustic Velocity in High Symmetry Planes of Ice III	98
4.1 Growth of Single Crystal of Ice V	111
4.2 Brillouin Spectrum Collected From Ice V	115
4.3 Frequency Shifts of Ice V verses $\Delta\phi$	122
4.4 Acoustic Velocity in High Symmetry Planes of Ice V	128
5.1 Extinction Angle Plotted Against $\Delta\phi$ , Ice VI	140
5.2 Growth of Single Crystal of Ice VI	149
5.3 Brillouin Spectrum Collected From Ice VI	152
5.4 Frequency Shift Versus $\Delta\phi$ , Ice VI	159
5.5 Pressure Dependence of the Elastic Constants of Ice VI	172
5.6 Acoustic Velocity in High Symmetry Planes in Ice VI	177
A1 Extinction Angle Plotted Against $\Delta\phi$ , Ice V	A4
B1 Neutron Scattering Data, Transverse Acoustic Peak	B6
B2 Excess Low Frequency Modes	B9

## List of Symbols

$C_{ij}$	elastic constant tensor element
$S_{ij}$	elastic compliance tensor element
$\Phi$	energy of crystal lattice
$\xi_i$	stress tensor element
$U_i$	linear displacement vector
$k_i$	wavevector in crystallographic frame
$V_L$	longitudinal acoustic velocity
$V_T$	transverse bulk velocity
$B_s$	Adiabatic bulk modulus
$\Delta$	volume change
$P$	pressure
$\lambda, \mu$	Lamé constants
$\rho$	density
$E$	Young's modulus
$\sigma$	Poisson's ratio
$\omega_s, \omega_o, \omega_q$	frequency of the incident, scattered and acoustic phonon respectively
$n$	refractive index
$\alpha$	scattering angle
$\Lambda$	wavelength of light
$\theta, \phi, \chi$	Euler angles
$\eta$	standard deviation of Brillouin frequency shift
$H$	error matrix
$L$	logitudinal Brillouin frequency shift
$T_i$	transverse Brillouin frequency shift
$\bar{V}_L$	average longitudinal acoustic velocity
$\bar{V}_T$	average transverse acoustic velocity

# CHAPTER I

## Introduction to Water and Ice

### *1.1 INTRODUCTION*

Throughout the universe water is thought to be an abundant substance. In addition to liquid and gas there are 13 known solid phases of water; ice Ih is the phase naturally occurring on Earth. Here the oceans contain approximately  $1.4 \times 10^{21}$  kg and the rock making up the crust contains another  $8.0 \times 10^{20}$  kg of liquid water. Water existed on Earth long before any form of living organism and it is widely accepted that early life evolved from the oceans. Water has, therefore, become an essential component of all living organisms. The human body, for instance, is approximately 65% water with some tissue such as the brain containing as high as 80%.<sup>1</sup> Water is the only naturally occurring chemical compound which occurs on earth in all three physical states: solid, liquid and gas.<sup>2</sup> Despite its natural abundance and biologic significance water is one of the simplest molecules, consisting merely of one oxygen atom and two hydrogen atoms. Yet water in condensed form exhibits many unique physical and chemical properties. For example, (i) liquid water is an excellent solvent of many compounds, (ii) it has an unusually high heat capacity<sup>3</sup> ( $C_p$  at 100°C is  $8.6 \text{ cal mole}^{-1} \text{ deg}^{-1}$  which is nearly constant between 0 to 100°C with a slight minimum near 35°C), (iii) as water is cooled below 4°C its density decreases, and (iv) upon freezing into ice Ih the density<sup>4</sup> drops from  $0.99987 \text{ g cm}^{-3}$  to  $0.9167 \text{ g cm}^{-3}$  (at 0°C) causing ice to float in its melt. (Solids that exhibit such a negative  $\Delta V$  upon melting exist as relatively open structures with low coordination numbers: melting increases the coordination number and hence the density.) The fact that water has

greater density than ice Ih causes lakes and oceans to freeze from the surface; this profoundly affected primitive organisms by forming a protective layer which trapped heat and sustained life.

Water, in the form of ices and clathrate hydrates,<sup>5</sup> is found to be a component of many bodies throughout the solar system.<sup>6</sup> Many geologic processes on extraterrestrial bodies are thought to depend on the rheology of the ice phases involved. Based on the predicted low density of the six inner satellites of Saturn it has been proposed that the moons of Saturn contain a high percentage of water ice.<sup>7</sup> Later it was shown by infrared photometry and infrared reflection spectroscopy that ice does exist on the satellites of Saturn and Jupiter.<sup>8-10</sup> In fact, many of the geological features of Mars appear to have formed by the release of ground water from beneath the surface and ice is the principal lithospheric component of most of the moons of the outer solar system.<sup>11</sup> In addition, the polar ice caps of Mars are made up of a combination of water and CO<sub>2</sub> ice.<sup>12,13</sup> Amorphous forms of ice and clathrates are thought to condense in interstellar molecular clouds and to constitute the bulk matter of comets.<sup>14-17</sup> It has been proposed that phase transitions in the ice making up comets cause larger amounts of gas production with respect to perihelions exhibited by some comets.<sup>18,19</sup>

H<sub>2</sub>O (water) molecules condense by forming clusters resulting in either liquid water or a crystal lattice through a process known as hydrogen bonding. In such a bonding process the hydrogen atom sits between two electronegative oxygen atoms.<sup>20</sup> The hydrogen bond

has been found in many organic materials and plays a large role in bonding water to other materials. The structure of proteins is largely due to hydrogen bonds formed between two nearby amino acids in the polypeptide chain which cause the chain to twist into a helix. In fact, the bonding between the two strands of double helix DNA is due to the formation of hydrogen bonds between bases.<sup>21</sup>

Advances in the techniques of molecular dynamics computer simulation and *ab initio* techniques<sup>22,23</sup> require, or lead to, interaction pair potentials which may be used to calculate the physical properties of water and ice.<sup>24,25</sup> Reviews of several water-water interaction potentials have been carried out in which gas, liquid and solid state properties of water are calculated and compared with experimental results. It was found that no one pair potential gives satisfactory account of all three phases.<sup>26-28</sup> Despite the apparent simplicity of the hydrogen bond this important fundamental interaction is not well understood. The elastic constants of ice Ih have recently been calculated to test the validity of the TIP4P potential (transferable intermolecular potential function)<sup>29</sup> in a molecular dynamics calculation which suggests that the pressure induced phase transformation from ice Ih to high density amorphous (hda) ice is driven by a mechanical softening of the  $C_{66}$  elastic constant.<sup>30</sup> Through such studies, it has become evident that detailed knowledge of the elastic properties of materials can provide extremely sensitive benchmark tests of a potential function which describes the molecular or atomic bonding. Until the present study, only the elastic constants of naturally occurring ice Ih<sup>31</sup> were available to provide such a bench mark test of the water-water potential in ice. The

present work should, therefore lead to more detailed understanding of hydrogen bonding.

### ***1.1.1 Water Molecule***

The study of the physical properties of liquid water and ice begins with a brief discussion of the general characteristics of the water molecule and includes the mechanisms of molecular bonding. The electronic structure of the oxygen atom is  $1s^2 2s^2 2p^4$  while the electronic structure of hydrogen is simply  $1s^1$ . The water molecule may be thought of as being made up of three nuclei surrounded by ten electrons. Two of the electrons fill the  $1s$  shell about the oxygen atom and the others form pairs in four directed orbitals. Two of the four electron orbitals are directed along the oxygen-hydrogen bond directions and form bonding orbitals. The others, on the opposite side of the oxygen atom, form lone pair orbitals. The resulting molecule is roughly tetrahedral with the oxygen nucleus at the centre, the hydrogen atoms at two vertices, and the lone pair orbitals along opposite vertices. Calculations based on the above idea have assumed a particular form of the electronic wavefunction for which the energy is then minimized by letting the wavefunction vary. Other calculations have been based on linear combinations of the atomic orbitals.<sup>32-36</sup> The results agree well with the experimental values of the bond angle,  $104.523^\circ$ , and equilibrium bond length,  $0.95718 \text{ \AA}$ <sup>37</sup>. The water molecule is therefore polar with dipole moment contributions from the lone pair orbitals in addition to contributions from the protons. The total dipole moment of the water molecule<sup>38</sup> is  $(6.10 \pm 0.02) \times 10^{-30}$  C.m.

Water molecules tend to hydrogen bond in a tetrahedral coordination geometry to four other water molecules. In such an arrangement the OH group of one molecule is generally along the direction of the lone pair of the neighbouring molecule. It has been shown by x-ray diffraction that the water molecules in ice Ih bond to form a hexagonal lattice,<sup>39</sup> with unit cell dimensions  $a = 4.5190 \text{ \AA}$ ,  $c = 7.3616 \text{ \AA}$  at  $-10^\circ\text{C}$ , and the lattice constants have been shown to be almost constant<sup>40</sup> down to  $-260^\circ\text{C}$ . The space group was found by single crystal neutron diffraction to be  $P6_3/mmc$ ; the oxygen-oxygen distance is  $2.74 \text{ \AA}$  and the angle formed by three oxygen molecules is  $109 \pm 0.2^\circ$ .<sup>41</sup>

The fact that the infrared spectra of liquid water, ice Ih, and water vapour are essentially the same indicates that the structures of the water molecules is the same in all three phases.<sup>42</sup> The symmetric and anti-symmetric vibrations of the water molecule (at  $\sim 3300 \text{ cm}^{-1}$ ) are slightly decreased in frequency and the bending vibration slightly increased in frequency due to molecular bonding, however, it is clear that the water molecules have not been destroyed. This is true for almost all high pressure phases of ice. One exception is thought to be ice X, which forms at a pressure on the order of 50 GPa and in which it is thought that the hydrogen atom lies at the midpoint between the oxygen atoms.<sup>43</sup> This behaviour of ice Ih led Bernal and Fowler<sup>44</sup> to postulate that the hydrogen atom must be approximately along the line connecting the two oxygen atoms. The distance of the hydrogen from one oxygen atom is approximately  $1 \text{ \AA}$  and therefore the distance to the other oxygen atom is about  $1.76 \text{ \AA}$ . Such a bonding scheme indicates that the H-O-H angle of the water molecule only deviates slightly from the vapour phase value of  $105^\circ$ .

### **Figure 1.1 Bernal-Fowler Ice Rules**

The Bernal-Fowler *ice rules* <sup>44</sup> indicating the six possible orientations of a water molecule tetrahedrally bonded to four other water molecules. The oxygen and hydrogen atoms are represented by open and solid circles respectively. Hydrogen bonds are indicated by dotted lines.

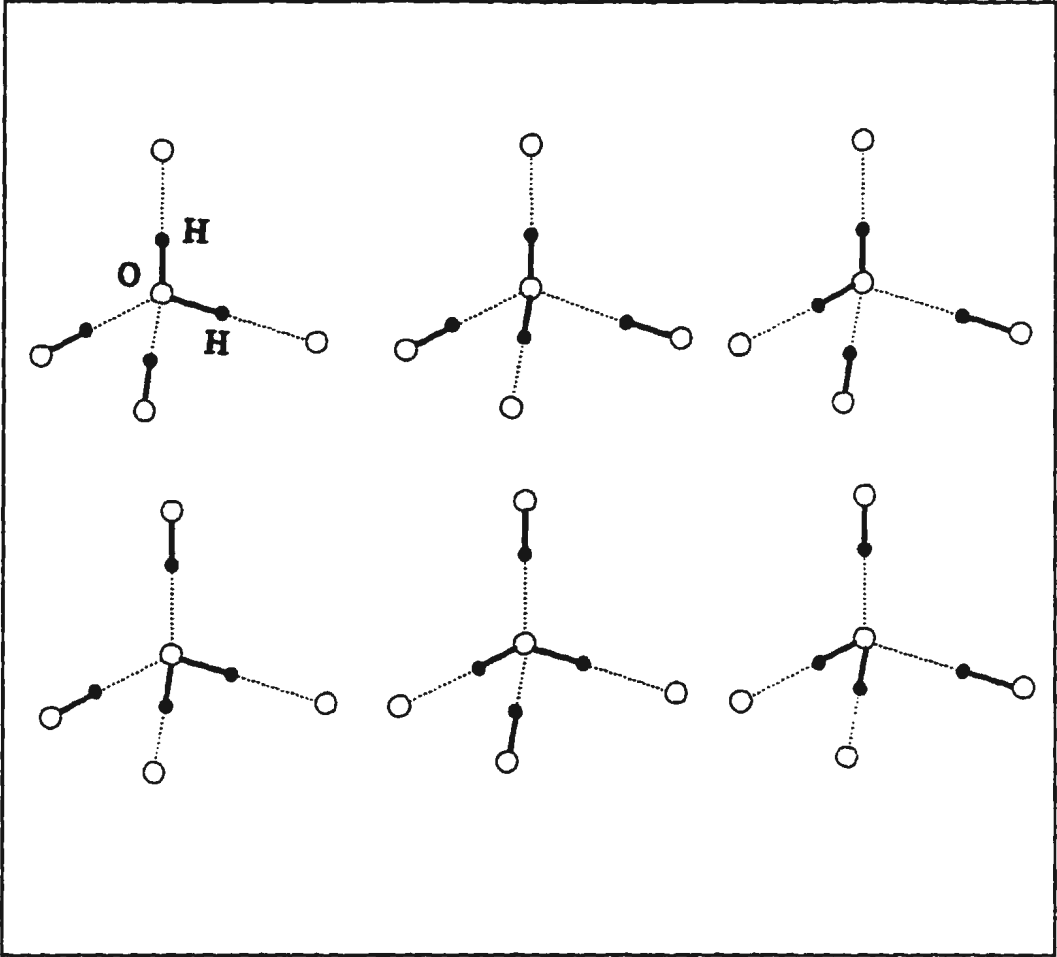


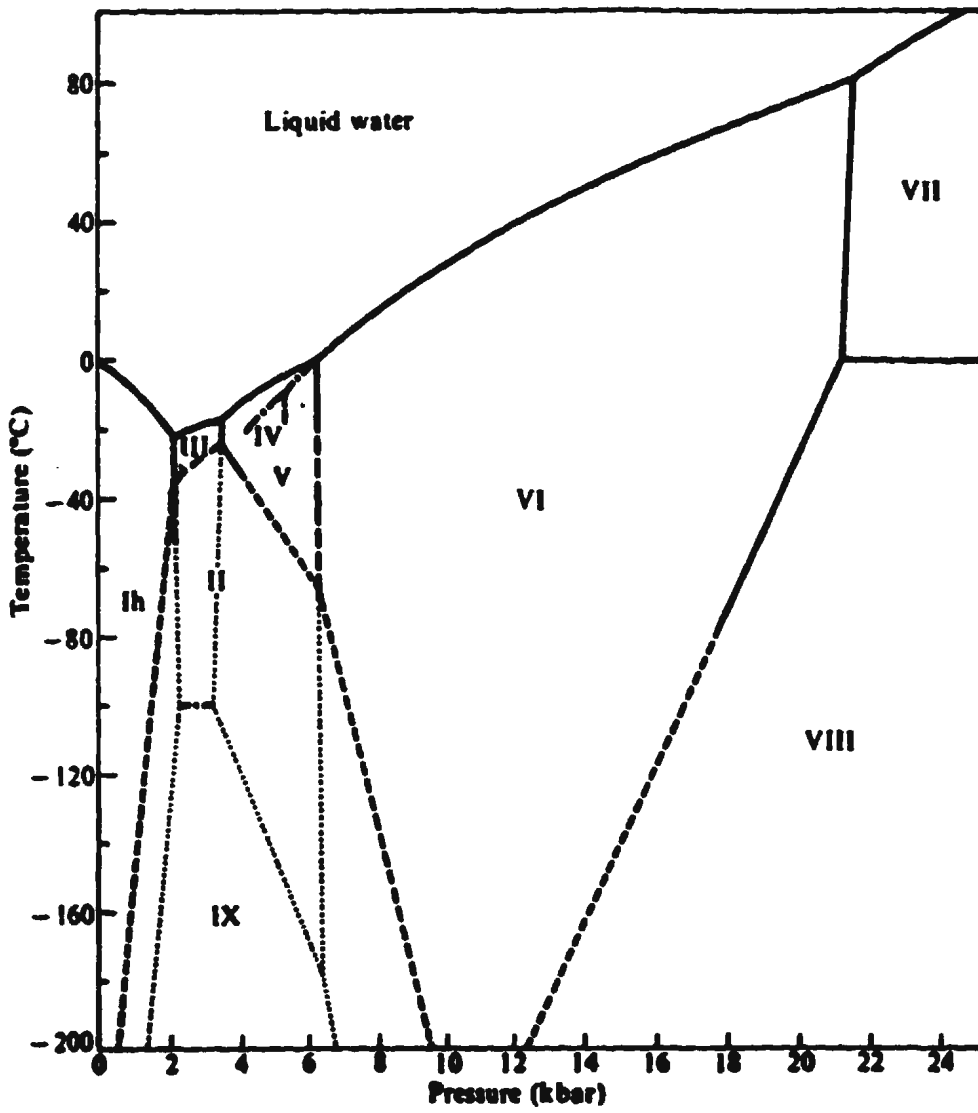
Fig. 1.1 illustrates the six possible orientations of a water molecule bonding to four others in a tetrahedral arrangement. It is evident that a large number of structures may be built up from this bonding arrangement, most of which are disordered with respect to hydrogen atom positions. The Bernal-Fowler rules may be stated as: 1) Each oxygen atom has two hydrogen atoms attached to form an intact water molecule. 2) Each water molecule is oriented so that its two hydrogen atoms are directed approximately toward two of the four oxygen atoms which surround it tetrahedrally. 3) The orientations of adjacent molecules are such that only one hydrogen atom lies along each hydrogen bond. This has been essentially confirmed for the case of D<sub>2</sub>O using neutron diffraction by Peterson and Levy.<sup>45</sup>

## ***1.2 HIGH PRESSURE PHASES***

The above tetrahedral bonding geometry of naturally occurring ice Ih leads to a very open structure formed by large hexagonal rings. Application of pressure causes the bond geometries to change by bending the O-O-O angle and changing the hydrogen bond length. This eventually leads to phase transitions in which the packing of water molecules lowers the lattice energy and results in higher density. The solid phases of water are therefore diverse and complex. As pressure and temperature are varied, ice exhibits no less than 13 distinct solid phases, the most of any known substance. The pressure-temperature phase diagram showing 9 polymorphs of ice has been reproduced<sup>46</sup> in Fig.

## **Figure 1.2 Phase Diagram of Ice**

**The phase diagram indicating 9 high pressure phases of ice. The solid lines indicate well defined phase transitions, the long dashed lines indicate meta-stable phase boundaries and the short dashed and dotted lines indicate extrapolated or estimated phase boundaries. Reproduced from reference 46.**



1.2. All of the phases shown in the Figure follow the Bernal-Fowler *ice rules* discussed above. The solid lines of the phase diagram indicate well established phase boundaries. It is, however, well documented that neighboring phases of ice may be superheated or cooled well into the stability field of another. Other phases of ice form at higher pressures than shown in Fig 1.2. It has been shown by Raman<sup>47,48</sup> and Brillouin<sup>43</sup> scattering, for example, that ice may transform, at about 500 kbar, to what is thought to be a cuprite structure (Pn3m) where the oxygen atoms form a cubic bcc lattice. This structure has been referred to as ice X which is predicted to be ionic in nature.<sup>49</sup> It should be noted that the existence of this high pressure phase is still a matter of considerable debate.<sup>50</sup> The high density amorphous (hda) phase of ice occurs when ice Ih is pressurized to 10 kbar at liquid nitrogen temperatures. As the temperature of an hda sample is raised to approximately 120K a transformation takes place to low density amorphous (lda).<sup>51,52</sup> The transformation from hda to lda has been shown by calorimetry experiments to be exothermic.<sup>53</sup> Similar pressure induced phenomena have since been discovered in other materials and are thought to be due to a mechanical softening of the lattice.<sup>54</sup> Amorphous phases of ice are also formed by vapour deposition of water on a cold plate below 77K<sup>55</sup> and by rapid temperature quenching of liquid water.<sup>56,57</sup> Preliminary incoherent inelastic neutron scattering experiments aimed at investigating excess low frequency excitations, conducted at Atomic Energy of Canada Ltd., Chalk River Laboratories, are discussed in Appendix B.

Early experiments to determine the stability fields of the various high pressure phases of

ice were carried out by Tammann<sup>58</sup> who worked at pressures up to about 3.5 kbar and was the first to report ice III and ice II. Between 1912 and 1937 Bridgman<sup>59-62</sup> undertook an extensive investigation of the phase boundaries of the high pressure phases of both H<sub>2</sub>O and D<sub>2</sub>O ice. Excellent reviews of the discovery of the phases may be found in Hobbs.<sup>46</sup> Many of the high pressure phases are metastable at atmospheric pressure when quenched to liquid nitrogen temperature. This property enabled much of the early work, such as structural determination, to be carried out. The crystallographic structures of the high pressure phases of ice are presented in Table 1.1. The physical properties of ice III, V, and VI will be discussed in greater detail in the following section.

### ***1.2.1 Ice III***

The first attempt to determine the structure of ice III was made in 1936 by R.L. McFarlan<sup>63</sup> using x-ray diffraction. However, the crystallographic structure proposed by McFarlan was in violation of the Bernal-Fowler *ice rules* and hence lead to the incorrect conclusion that water molecules were disassociated and their tetrahedral character lost. Later W. B. Kamb and S. K. Datta<sup>64</sup> conducted x-ray diffraction experiments in which polycrystalline samples of ice III were quenched to liquid nitrogen temperatures and data were collected from samples recovered at atmospheric pressure. It was shown that the crystal structure of the quenched phase is symmetrically tetragonal and the space group represented by P4<sub>1</sub>2<sub>1</sub>2 with 12 molecules per unit cell (see Table 1.1). No hydrogen bond deviates by more than 17° from a tetrahedral direction while one of the O-O-O angles has the extraordinarily large value of about 143°, the largest deviation from perfect tetrahedral

Table 1.1  
Structural Data on the Polymorphs of Ice<sup>46</sup>

Polymorph	Crystal System	Cell Dimensions (Å)	O-O Distance (Å)	O-O-O Angles (deg.)
Ice Ih	Hexagonal (P6 <sub>3</sub> /mmc)	a <sub>0</sub> =4.50, c <sub>0</sub> =7.32	2.74	109±0.2
Ice Ic	Cubic (Fd3m)	a <sub>0</sub> =6.35	2.75	109.5
Ice II	Rhombohedral (R3̄)	a <sub>0</sub> =7.79, α=111.3°	2.75-2.84	80-128
Ice III	Tetragonal (P4 <sub>1</sub> 2 <sub>1</sub> 2)	a <sub>0</sub> =6.73, c <sub>0</sub> =6.83	2.76-2.80	87-141
Ice V	Monoclinic (A2/a)	a <sub>0</sub> =9.22, b <sub>0</sub> =7.54 c <sub>0</sub> =10.35, β=109.2°	2.76-2.87	84-128
Ice VI	Tetragonal (P4 <sub>2</sub> /nmc)	a <sub>0</sub> =6.27, c <sub>0</sub> =5.79	2.80-2.82	76-128
Ice VII	Cubic (Pn3m)	a <sub>0</sub> =3.43	2.95	109.5
Ice VIII	Tetragonal (I4 <sub>1</sub> /amd)	a <sub>0</sub> =4.80, c <sub>0</sub> =6.99	2.96	≈109.5
Ice IX	Tetragonal (P4 <sub>1</sub> 2 <sub>1</sub> 2)	a <sub>0</sub> =6.73, c <sub>0</sub> =6.83	2.76-2.80	87-140

coordination. Ice III was shown to be fully hydrogen bonded<sup>65,66</sup> but disordered with respect to the positions of the hydrogen atoms.<sup>67</sup> It is quite likely that the samples quenched to liquid nitrogen temperature by Kamb were in fact ice IX, which is an antiferroelectrically ordered phase<sup>68,69</sup> with the same crystal structure as ice III.

The elastic properties of polycrystalline samples of ice III have been studied previously by G.H. Shaw<sup>70</sup> who investigated the compressional and shear wave velocities at -25°C and various pressures in the ice III stability field. Polycrystalline aggregates were prepared from pulverized ice made from distilled water. The technique involved collecting time-of-flight data from 5 MHz sine wave pulses produced by either shear or compressional wave transducers. Shaw reported that the longitudinal and transverse acoustic velocities of ice III are 3610 m s<sup>-1</sup> and 2040 m s<sup>-1</sup> respectively at a pressure of 2.1 kbar. The bulk modulus decreases from 106 kbar to 85 kbar and the shear modulus increases from 33 kbar to 48 kbar in going from ice Ih to ice III at 2.1 kbar and -25°C. Both increase, however, with pressure within each phase. R.E. Gagnon, *et al.*<sup>31</sup> have investigated the elastic properties of polycrystalline samples of ice III at -27.2°C by Brillouin spectroscopy. The longitudinal and transverse acoustic velocities at 2.1 kbar were found to be 3640 m s<sup>-1</sup> and 1865 m s<sup>-1</sup>, respectively, and are shown to increase with pressure more rapidly than the acoustic velocity of ice Ih, ice II, ice V, and ice VI. The bulk modulus  $B_1$  at the same pressure was calculated to be 99.6 kbar at -27.2°C and 2.1 kbar. These results will be further discussed with regard to the present results in chapter III.

### **1.2.2 Ice V**

The preliminary crystallographic determination of the structure of ice V was done by x-ray powder diffraction<sup>71,72</sup> and determined to be monoclinic, which is the lowest structural symmetry of all the known polymorphs of ice. The space group is A2/a with 28 molecules per unit cell (see Table 1.1). The system, like ice III, is fully hydrogen bonded, disordered with respect to the positions of the hydrogen atoms (complete proton ordering is not possible for the A2/a space group), and four coordinated.<sup>65-67</sup> The distortion from the ideal tetragonal coordinations leads to O-O-O angles between 84° and 128°.

The elastic properties of ice V have also been studied by Shaw<sup>70</sup> and Gagnon *et al.*<sup>31</sup>. Shaw gave values of 4140 m s<sup>-1</sup> and 2210 m s<sup>-1</sup> as the longitudinal and transverse acoustic velocities respectively; the adiabatic bulk modulus  $B_s$  was determined to be 132 kbar at P=3.4 kbar and T=-25°C. Gagnon *et al.*<sup>31</sup>, gave 4177 m s<sup>-1</sup>, 2200 m s<sup>-1</sup> as the longitudinal and transverse acoustic velocities at the same pressure and -35°C. From this velocity data the bulk modulus  $B_s$  is calculated to be 137.5 kbar. Both authors report a large jump in the compressional wave velocity in passing from ice III to ice V. The agreement between values obtained by ultrasonic acoustic wave propagation and Brillouin scattering is quite good. This data will be compared to values calculated from the elastic constants found in the present study in chapter IV.

### **1.2.3 Ice VI**

The structure of ice VI is quite different from the structure of any of the phases yet

discussed. Kamb<sup>64</sup> reported that the high density of ice VI is achieved, while maintaining the tetrahedral bonding structure, by two interpenetrating lattices in which the molecules of one lattice fill the voids of the other. The molecules of each lattice form a hydrogen bonded network but no such bonding exists between the two interpenetrating structures. This has been called a self-clathrate by Kamb. The space group symmetry of ice VI is  $P4_2/nmc$  with a tetragonal unit cell containing ten water molecules (see Table 1.1). Dielectric measurements made by G.J. Wilson, *et al.*<sup>67</sup> and infrared measurements<sup>73</sup> indicate that ice VI, like ice III and ice V, is orientationally disordered with respect to the hydrogen positions at high temperature. The tetrahedral arrangement of atoms is, however, highly distorted with O-O-O angles between  $76^\circ$  and  $128^\circ$ . A phase transition to an ordered antiferroelectric structure may occur as ice VI is slowly cooled through 123 K; this ordering requires a degradation of the space group symmetry.<sup>74,75</sup>

The elastic properties of ice VI have been studied by several authors including Shaw<sup>70</sup> and Gagnon.<sup>31</sup> Shaw gives the compressional and shear acoustic velocity and bulk modulus in ice VI at  $-25^\circ\text{C}$  and 8.0 kbar as  $4530 \text{ m s}^{-1}$ ,  $2530 \text{ m s}^{-1}$ , and 160 kbar, respectively. Gagnon *et al.* gives values, at the same temperature and pressure conditions, of  $4558 \text{ m s}^{-1}$ ,  $2357 \text{ m s}^{-1}$ , and 182 kbar, respectively. Brillouin work has also been done by Polian and Grimsditch<sup>76</sup> to determine the elastic properties of polycrystalline ice VI grown in a diamond anvil cell. Brillouin spectra were collected at room temperature between 0 and 5 kbar. Polian and Grimsditch conclude that ice VI is elastically isotropic and therefore estimate the elastic constant  $C_{11} \approx 28 \times 10^4 \text{ bar}$  at  $P = 10 \text{ kbar}$ . Very recently the elastic

constants of ice VI have been determined by Brillouin spectroscopy at pressures above 10 kbar (the present study examines data collected from samples below 10 kbar). Crystals were grown in a diamond anvil cell by H. Shimizu, *et al.*<sup>77</sup>, and the elastic constants determined at 12.3 kbar were  $C_{11}=32.8$ ,  $C_{12}=11.8$ ,  $C_{13}=14.7$ ,  $C_{33}=27.8$ ,  $C_{44}=6.3$ , and  $C_{66}=5.9$  ( $\times 10^4$  bar). The results of the present study may be extrapolated to 12.3 kbar and, in general, compare well with the results of Shimizu *et al.*, with the exception of  $C_{12}$  and  $C_{66}$ . It should be noted that samples produced in a diamond anvil cell are necessarily very small and it is likely that surface effects due to the small sample size may affect experimental data. In addition, Shimizu *et al.* have only collected spectra from one sample, whereas it was noted in the present study that at least two independent samples were required to uniquely determine all elastic constant values. This will be discussed further in chapter V. Before discussing the results from ice III, ice V, and ice VI, the technique of Brillouin spectroscopy, experimental apparatus and elastic theory will be introduced in the next chapter.

# **CHAPTER II**

## **Elastic Theory, Brillouin Spectroscopy and Experimental Apparatus**

### ***2.1 ELASTIC THEORY***

The manner in which solids behave when subject to forces may be described in terms of two theories. A solid is said to behave plastically when it remains deformed after an applied force is relieved. In contrast, a solid is said to behave elastically when it returns to its original shape upon the release of the applied force. Since it is the goal of the thesis to first find the acoustic velocity in various phases of ice, only elastic theory will be treated in detail.

#### ***2.1.1 Stress and Strain***

In relating the elastic properties of solids to their acoustic properties as determined by Brillouin spectroscopy it is worth noting that acoustic wave lengths are long compared with the crystallographic unit cell size, hence a continuum model may be used. Elastic theory will be implemented in the linear, or Hooke's Law, approximation. In order to develop a theory of elasticity it is necessary to first define the applied force, or stress, and

the resulting deformation, or strain. There have been several excellent reviews of the elastic properties of solids.<sup>78-80</sup> Consider an arbitrary length segment  $ds$  in the unstrained solid. In Cartesian coordinates  $ds_u^2 = dx_i dx_j \delta_{ij}$ . In a strained solid the length of the segment will change by  $U_i(x_j)$ . The first derivatives of  $U_i(x_j)$  are continuous and the length segment may now be written as

$$ds_s^2 = (dx_i + \frac{\partial U_i}{\partial x_j} dx_j) (dx_i + \frac{\partial U_i}{\partial x_k} dx_k)$$

and

$$ds_s^2 = dx_i dx_j [\delta_{ij} + \frac{\partial U_i}{\partial x_j} + \frac{\partial U_j}{\partial x_i} + \frac{\partial U_k}{\partial x_i} \frac{\partial U_k}{\partial x_j}] . \quad 2.1$$

Each element of the strain tensor can be found by considering the net length change of the segment  $ds$  given by

$$\begin{aligned} ds_s^2 - ds_u^2 &= dx_i dx_j \delta_{ij} - dx_i dx_j [\delta_{ij} + (\frac{\partial U_i}{\partial x_j} + \frac{\partial U_j}{\partial x_i} + \frac{\partial U_k}{\partial x_i} \frac{\partial U_k}{\partial x_j})] \\ &= -2 e_{ij} dx_i dx_j . \end{aligned} \quad 2.2$$

The  $e_{ij}$  make up the strain tensor defined as

$$e_{ij} = \frac{1}{2} [\frac{\partial U_i}{\partial x_j} + \frac{\partial U_j}{\partial x_i} + \frac{\partial U_k}{\partial x_i} \frac{\partial U_k}{\partial x_j}] \quad 2.3$$

where  $i, j = 1, 2, 3$  and the  $e_{ij}$  are the 9 elements of the rank 2 strain tensor. When an elastic solid is strained due to an acoustic wave, the displacement of atoms or molecules from their equilibrium positions is very small. The first derivatives of  $U_i$  are therefore small

and the product of derivatives in the above equation may be ignored so that

$$e_{ij} = \frac{1}{2} \left( \frac{\partial U_i}{\partial x_j} + \frac{\partial U_j}{\partial x_i} \right) . \quad 2.4$$

The forces acting on an elemental surface area within the solid are known as stresses and are denoted by the elements of the second rank tensor  $\xi$ . The stress may be a force which either compresses ( $\xi_{ii}$ ) or shears ( $\xi_{ij}$ ) the surface. In general, there are stresses associated with each surface of an arbitrary elemental cube within a solid (see Section 2.1.3, Figure 2.1). The principal axes of the stress tensor are given by its eigenvectors and the associated eigenvalues are the called the principal stresses of which there are no shear components.

It is necessary to develop a relation between the applied stress and the resulting strain. Let  $\Phi(0)$  be the internal energy function of a unit mass of unstrained solid.<sup>81</sup> Consider a small deformation of the solid resulting from an external or internal stress.  $\Phi$  may then be expanded in a Taylor series about equilibrium as follows

$$\Phi = \Phi(0) + \left[ \frac{\partial \Phi}{\partial e_{ij}} \right]_0 e_{ij} + \frac{1}{2} \left[ \frac{\partial^2 \Phi}{\partial e_{ij} \partial e_{kl}} \right]_0 e_{ij} e_{kl} + \dots . \quad 2.5$$

Since there are no forces present at zero displacement  $\Phi(0)$  is a stable minimum in the potential function and the second term is equal to zero. The work done in deforming the solid must be positive and the change in energy may be truncated at the first order and written as

$$\Delta \Phi = \frac{1}{2} \left[ \frac{\partial^2 \Phi}{\partial e_y \partial e_H} \right]_0 e_y e_H . \quad 2.6$$

This truncated equation is known as the harmonic approximation. Alternatively the total work done by the applied stress is equally expressed as,

$$\Delta W = \frac{1}{2} \xi_y e_y . \quad 2.7$$

The factor of 1/2 is introduced to insure that the work done along each direction in the above summation is considered only once. Equating 2.6 and 2.7 gives,

$$\xi_y = \left[ \frac{\partial^2 \Phi}{\partial e_y \partial e_H} \right]_0 e_H . \quad 2.8$$

This is Hooke's law generalized to 3 dimensions. The constants which relate the stress to the resulting strain form a fourth rank tensor with 81 elements and are known as the elastic constants, *i.e.*

$$C_{yH} \equiv \left[ \frac{\partial^2 \Phi}{\partial e_y \partial e_H} \right]_0 . \quad 2.9$$

From the symmetry of the second derivative, the number of independent elastic constants may be reduced (*i.e.*  $C_{ijkl} = C_{klij}$ ). In addition, the number of elastic constants is further reduced by noting that all the forces must appear in opposing pairs, *i.e.*  $C_{ijkl} = C_{ijlk} = C_{jilk} = C_{jikl}$ . The number of elastic constants is thus reduced from 81 to 21 independent elements for a completely elastically anisotropic solid, such as the triclinic system, and further reductions are possible when considering crystals with higher symmetry. At this point it is convenient to introduce a notation such that the remaining independent elastic

constants form a 6x6 matrix, and likewise the stress and strain tensors are reduced to 6 element vectors. The subscripts of each element are contracted according to the following scheme:<sup>78</sup>

11	→	1		23, 32	→	4
22	→	2		31, 13	→	5
33	→	3		12, 21	→	6,

hence the generalized Hooke's law  $\xi_{ij} = C_{ijkl} e_{kl}$  may be rewritten as  $\xi_p = C_{pq} e_q$ .

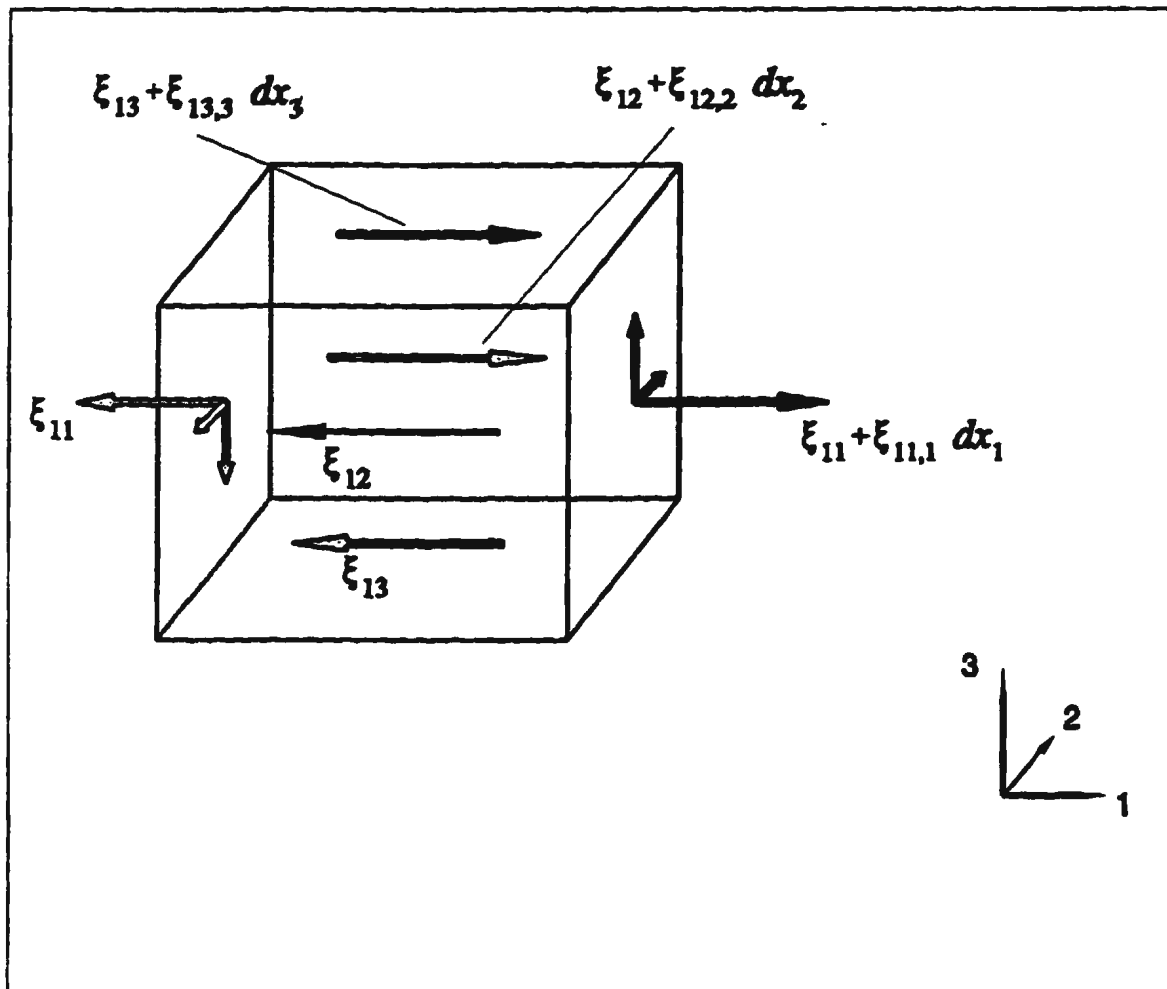
### 2.1.2 Equations of motion

The velocity of a propagating acoustic wave may be found by solving the equations of motion of an elemental volume of solid undergoing harmonic oscillations. In order to derive and solve the equations of motion consider all the forces acting on an arbitrary volume element, including both compressional and shear stresses. Fig. 2.1 illustrates only stresses in the x-direction and shearing forces acting on the two surfaces perpendicular to the x-axis.<sup>81</sup> The stresses in the y and z directions are written in a similar manner. Adding all the forces in the x-direction gives

$$\begin{aligned}
 & -[\xi_{11} dx_2 dx_3 + \xi_{12} dx_1 dx_3 + \xi_{13} dx_2 dx_1] \\
 & + [(\xi_{11} + \xi_{11,1} dx_1) dx_2 dx_3 + (\xi_{12} + \xi_{12,2} dx_2) dx_1 dx_3
 \end{aligned}$$

**Figure 2.1 Elemental Volume Illustrating Stress Components**

Volume element within a solid showing the stresses in the x direction and the shearing forces acting on the face perpendicular to the x-axis. The stress, strain and elastic constant tensors are now defined with respect to the coordinate system indicated. The relative orientation of this coordinate system with respect to the crystallographic system follows the *Standards on piezoelectric crystals* (see for example reference 78).



$$\begin{aligned}
& + (\xi_{13} + \xi_{13,3} dx_3) dx_1 dx_2] + \rho X_i dx_1 dx_2 dx_3 \\
& = \rho \frac{\partial^2 U_1}{\partial t^2} dx_1 dx_2 dx_3
\end{aligned} \tag{2.10}$$

where  $\rho$  is the density and the partial derivatives  $\partial \xi_{ij} / \partial x_j$  are denoted as  $\xi_{sij}$ . The last term on the left hand side gives external forces, or body forces, applied to the system. Unbalanced external forces result in translation or rotation of the crystal as a whole and do not result in strain being introduced into the system. A complete development of elastic theory only requires analysis of internal forces, therefore, the term  $\rho X_i dx_1 dx_2 dx_3$  is set equal to zero. The term on the right hand side is the mass times the acceleration of the strained volume and simplifying this gives

$$\xi_{11,1} + \xi_{12,2} + \xi_{13,3} = \rho \frac{\partial^2 U_1}{\partial t^2} . \tag{2.11}$$

By rewriting this equation and introducing summation notation we get

$$\xi_{ij,j} = \rho \ddot{U}_i . \tag{2.12}$$

Using the generalized Hooke's law, Eq. 2.8, and noting that  $e_{kl} = e_{lk}$ , the equation of motion above can be expressed as,

$$\rho \ddot{U}_i = C_{ijkl} U_{k,l} . \tag{2.13}$$

The solution to the equation of motion is assumed to be a plane acoustic wave of the form

$$U_k = A e^{i(kr - \omega t)} . \quad 2.14$$

The subscript of the vector  $U_k$ ,  $k = 1,2,3$  indicates three polarizations of the displacement vector, two predominantly orthogonal to the direction of wave propagation, forming quasi-transverse acoustic waves, and the other predominantly parallel to the direction of wave propagation, forming quasi-longitudinal acoustic waves.<sup>82</sup> Differentiating these equations and substituting them into the equation of motion leads to a set of secular equations given by,

$$[C_{ijkl} k_i k_j - \rho \omega^2 \delta_{ik}] U_k = 0 . \quad 2.15$$

Near the Brillouin zone centre the acoustic dispersion relation is linear such that  $\omega = V k$ , where  $V$  is the velocity of the acoustic wave. Substituting this into the secular equations and setting the determinant equal to zero gives the eigenvectors  $\rho V^2$  of the expression,

$$|C_{ijkl} k_i k_j - \rho V^2 \delta_{ik}| = 0 . \quad 2.16$$

This is the well known Christoffel determinant which relates the acoustic velocity, direction of wave propagation, and the elastic constants to each of the three eigenvalues  $\rho V^2$ . The complexity of the resulting cubic equation for  $\rho V^2$  is greatly reduced when acoustic waves travel in high symmetry crystal directions. In the present study, however, there was no direct control over the orientation of the crystal during growth and thus it was not possible to choose scattering wavevectors in high symmetry directions. However, the determinant has been solved by Every<sup>83</sup> (for waves travelling in an arbitrary direction in most crystal structures) resulting in closed form expressions for the sound velocity of each acoustic polarization. It should be noted however that the closed form expressions

are not valid in regions where the acoustic velocity becomes degenerate or nearly degenerate. More reliable acoustic wave velocities in arbitrary directions when the transverse polarizations are degenerate may be found by performing numerical diagonalization of the Christoffel determinant. Numerical methods are the only way to calculate acoustic velocities for crystals with symmetries lower than orthorhombic. Once the acoustic velocity is found it may be used with the Brillouin equation, discussed in Section 2.2, to calculate the Brillouin frequency shifts and hence provide a function whose elastic constant parameters can be fitted to experimental data.

### ***2.1.3 Polycrystalline Elastic Properties***

It is evident from the above equations that the elastic properties and hence the acoustic velocities of most single crystals are not isotropic. In contrast, the elastic properties of a material made up of small randomly oriented crystallites may exhibit bulk elastic isotropy. The bulk mechanical properties of polycrystalline aggregates can be determined once the elastic properties of its individual crystallites are known. The theory for isotropic elastic behavior has been worked out by Voigt<sup>24</sup> assuming uniform strain, and by Reuss<sup>25</sup> using uniform stress. A good estimate of the polycrystalline behavior may be found by averaging single crystal elastic properties over all directions. In doing so, two assumptions must be made; (1) crystallites were assumed to be small and randomly oriented and, (2) grain boundaries were assumed to have no effect on the average elastic properties. The longitudinal acoustic velocity of the aggregate was first calculated from the elastic constants by performing a weighted average over all crystallographic directions. The

integral has the form

$$\bar{V}_L = \frac{1}{4\pi} \int V_L(C_{ij}k_i k_j) d\Omega . \quad 2.17$$

$V_L$  is calculated by numerically diagonalizing the dynamical matrix given by Eq. 2.15.

The compliance constants  $S_{ij}$  (or their reciprocals, the elastic constants  $C_{ij}$ ) and the volume change,  $\Delta$ , due to a hydrostatic stress,  $P$ , were used to calculate the volume compressibility (or its reciprocal, the bulk modulus) of a polycrystalline aggregate. The general equation relating the bulk modulus to the compliance constants for any crystal system was found to be<sup>81</sup>

$$B_s = -\left[\frac{\Delta}{P}\right]^{-1} = [S_{11} + S_{22} + S_{33} + 2(S_{12} + S_{23} + S_{31})]^{-1} . \quad 2.18$$

Symmetry conditions imposed by crystal structures considerably simplify this equation. The average longitudinal acoustic velocity  $\bar{V}_L$  was used along with the adiabatic bulk modulus  $B_s$  to calculate the remaining polycrystalline elastic properties.

Once the average longitudinal acoustic velocity and the bulk modulus were determined, many other elastic properties of polycrystalline materials were calculated. For a review of the theory see Gould.<sup>86</sup> Included were the compressional and shearing constants,  $\lambda$  and  $\mu$ , relating the applied stress to a resulting strain in an isotropic solid through the equation

$$\xi_y = \lambda U_y \delta_y + 2\mu U_y . \quad 2.19$$

This is the generalized Hooke's law simplified such that the elastic constant parameters

are no longer dependent on direction. The constant  $\lambda$  relates a linear strain with the corresponding linear stress, and  $\mu$  is the constant which relates a stress to a shearing strain in an isotropic solid. Solving the equations of motion of an elemental volume of isotropic solid gave the following expression for the average longitudinal acoustic velocity

$$\rho \bar{V}_L^2 = \lambda + 2\mu . \quad 2.20$$

The adiabatic bulk modulus  $B_s$  was found to be

$$B_s = \lambda + \frac{2}{3}\mu . \quad 2.21$$

Equations 2.20 and 2.21 when combined with the bulk modulus and average longitudinal acoustic velocity were solved for the Lamé constants  $\lambda$  and  $\mu$ . The average transverse acoustic velocity  $\bar{V}_T$  was found to be related to the Lamé constant  $\mu$  through

$$\rho \bar{V}_T^2 = \mu . \quad 2.22$$

The quotient of stress in one direction divided by the strain in the same direction, is known as Young's modulus  $E$ , and was found to be of the form

$$E = \frac{\mu(3\lambda + 2\mu)}{\lambda + \mu} . \quad 2.23$$

Finally, the quotient of a strain resulting from an applied stress in one direction with strain in a perpendicular direction, is known as Poisson's Ratio  $\sigma$ , and was found to be

$$\sigma = \frac{\lambda}{2(\lambda + \mu)} . \quad 2.24$$

The above elastic properties completely define the elastic behaviour of an isotropic solid

and were calculated in subsequent chapters for ice III, V, and VI.

## **2.2 BRILLOUIN SPECTROSCOPY**

Modern inelastic light scattering probes the properties of materials by scattering incident monochromatic laser light from bulk or surface excitations. As incident monochromatic light interacts with a material the scattered light is found to contain several spectral components other than those present in the incident beam.<sup>87</sup> In the case of Brillouin scattering the additional components are due to interactions with acoustic excitations, and the spectral shifts of the "additional" components give direct measure of the acoustic frequency, as proposed early in this century by Brillouin<sup>88</sup> and independently by Mandelshtam.<sup>89</sup>

### **2.2.1 Introduction**

The theory of Brillouin scattering has been discussed by many authors.<sup>90,91</sup> In particular, Brillouin scattering from cubic crystals has been discussed by Benedek and Fritsch<sup>92</sup> and in crystals of lower symmetry by Nelson *et al.*<sup>93</sup> The first Brillouin spectra were observed by Gross in a study of several liquids and solids.<sup>94</sup> The importance of Brillouin spectroscopy in determining the elastic constants of materials was first demonstrated by Krishnan in 1955.<sup>95</sup> For an excellent review of modern Brillouin spectroscopy see

Sandercock.<sup>96</sup> The Brillouin spectroscopic method of investigating materials requires no physical contact with the sample which can be less than 1 mm<sup>3</sup> in size. In fact, this spectroscopic technique has been applied to materials under ultra high pressures created in diamond anvil cells.<sup>97,98</sup> Brillouin spectroscopy therefore does not suffer the particular disadvantages found in other methods of determining elastic properties such as, time-of-flight ultrasonic experiments or inelastic neutron scattering. Time-of-flight measurement of ultrasonic acoustic waves require that piezo-electric transducers be physically attached to the sample.<sup>99</sup> Inelastic neutron scattering require large samples, ~ 1 cm<sup>3</sup>, and the measured dispersion curves in the long wavelength region may differ from adiabatic and isothermal (found using Brillouin spectroscopy) values. Brillouin spectroscopy does however suffer several limitations which include, restriction to acoustic frequencies in the GHz range, and studies are usually limited to optically transparent material, although, recently there have been Brillouin studies of opaque materials.<sup>96</sup>

Vibrational normal modes may be used to describe the constant thermal motion of molecules in materials. Brillouin spectroscopy specifically involves long wavelength acoustic modes in which all atoms in a particular unit cell oscillate in phase. In long wavelength acoustic modes the atomic displacements vary only slightly over several hundred unit cells so that the elastic continuum model discussed in the last section may be used. Such thermal modes cause local strain which in turn lead to spatial and temporal fluctuations in the dielectric constant. This causes the scattering of incident light through the elasto-optic effect. Strictly spatial fluctuations in the dielectric properties are called

non-propagating modes and are created by processes such as heat diffusion. These non-propagating modes give rise to elastically scattered components, known as Rayleigh lines, centred on the incident laser frequency  $\omega_i$ .<sup>100</sup> In contrast, acoustic modes propagate through the crystal lattice giving rise to a Doppler shift of the incident frequency and hence inelastically scattered light. These Doppler shifted components appear as "Brillouin doublets" about the central unshifted line in a typical Brillouin spectrum. Such inelastic processes require that energy and momentum are conserved as follows,

$$\hbar \omega_s = \hbar \omega_o \pm \hbar \omega_q$$

$$\hbar k_s = \hbar k_o \pm \hbar q \quad 2.25$$

where  $k_i$ ,  $k_s$  and  $q$  are the wavevectors of the incident and scattered light and acoustic mode, respectively. In the case of anisotropic crystals there are generally three Brillouin components about the central Rayleigh peak corresponding to two quasi-transverse polarizations and one quasi-longitudinal polarization of the acoustic wave. Furthermore, the half widths of these components indicate the damping, or attenuation, of acoustic waves. In most cases, however, the line widths are determined by instrumental broadening and true line widths are difficult to obtain.

### ***2.2.2 The Brillouin Equation***

The acoustic mode is selected by satisfying the Bragg scattering condition shown in Fig.

2.2. The optical path travelled by light reflected from successive planes must be an integral multiple of the wavelength of the incident beam. The path difference travelled by two consecutively reflected rays may be written

$$NR + N'R = 2NR = 2nd \sin\left(\frac{\pi}{2} - \phi\right) = \Lambda_i$$

$$\Lambda_i = 2 n d \cos(\phi) , \quad 2.26$$

where  $n$  is the index of refraction within the medium and  $\Lambda_i$  is the wavelength of the incident laser beam (note that the acoustic wavefront separation  $d = \lambda_q$  is the wavelength of sound in the medium), and

$$2 n \lambda_q \cos\left(\frac{\pi - \phi}{2}\right) = \Lambda_i . \quad 2.27$$

In the case of acoustic modes near the Brillouin zone centre the acoustic velocity is related to the wavelength by,  $\omega_q = V_q / \lambda_q$ , and the above equation may be written as

$$2 n \frac{V_q}{\omega_q} \sin\left(\frac{\alpha}{2}\right) = \Lambda_i . \quad 2.28$$

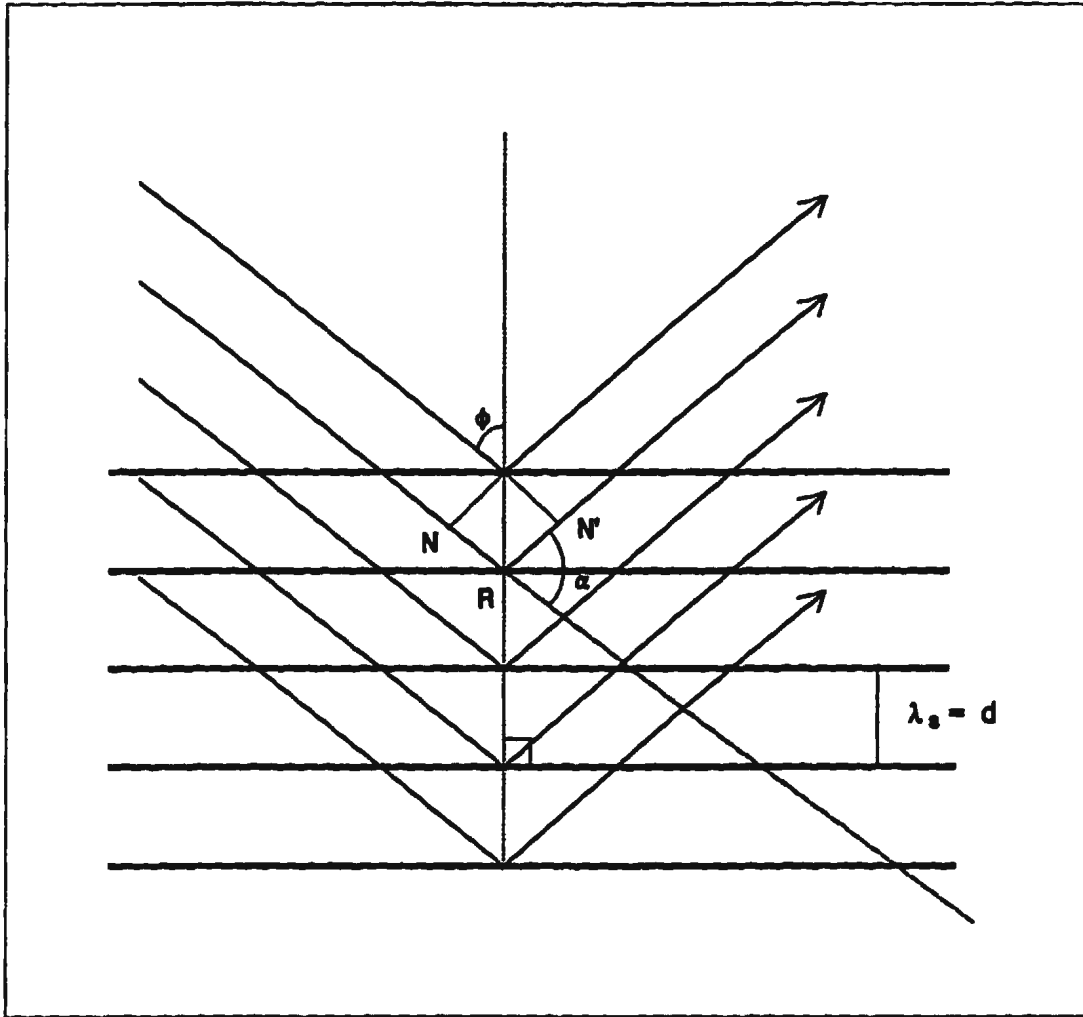
The scattering angle is given by  $\alpha$ . The frequency of the sound wave and the frequency shift  $\Delta\omega$  of the incident light due to the Doppler effect are given by

$$\Delta\omega_i = \omega_q = \frac{2 n V_q}{\Lambda_i} \sin\left(\frac{\alpha}{2}\right) . \quad 2.29$$

This is the well known Brillouin equation. In most Brillouin experiments the refractive index, incident wavelength and scattering angle are well defined, so that the velocity of

## **Figure 2.2 Bragg's Law**

**Illustration of the Bragg scattering condition. The heavy horizontal lines indicate acoustic wave fronts within the crystal, the diagonal lines indicate incoming and scattered light, and the dashed line indicates one transmitted ray. The spacing between wave fronts is the wavelength of the acoustic mode selected by the Bragg condition.**



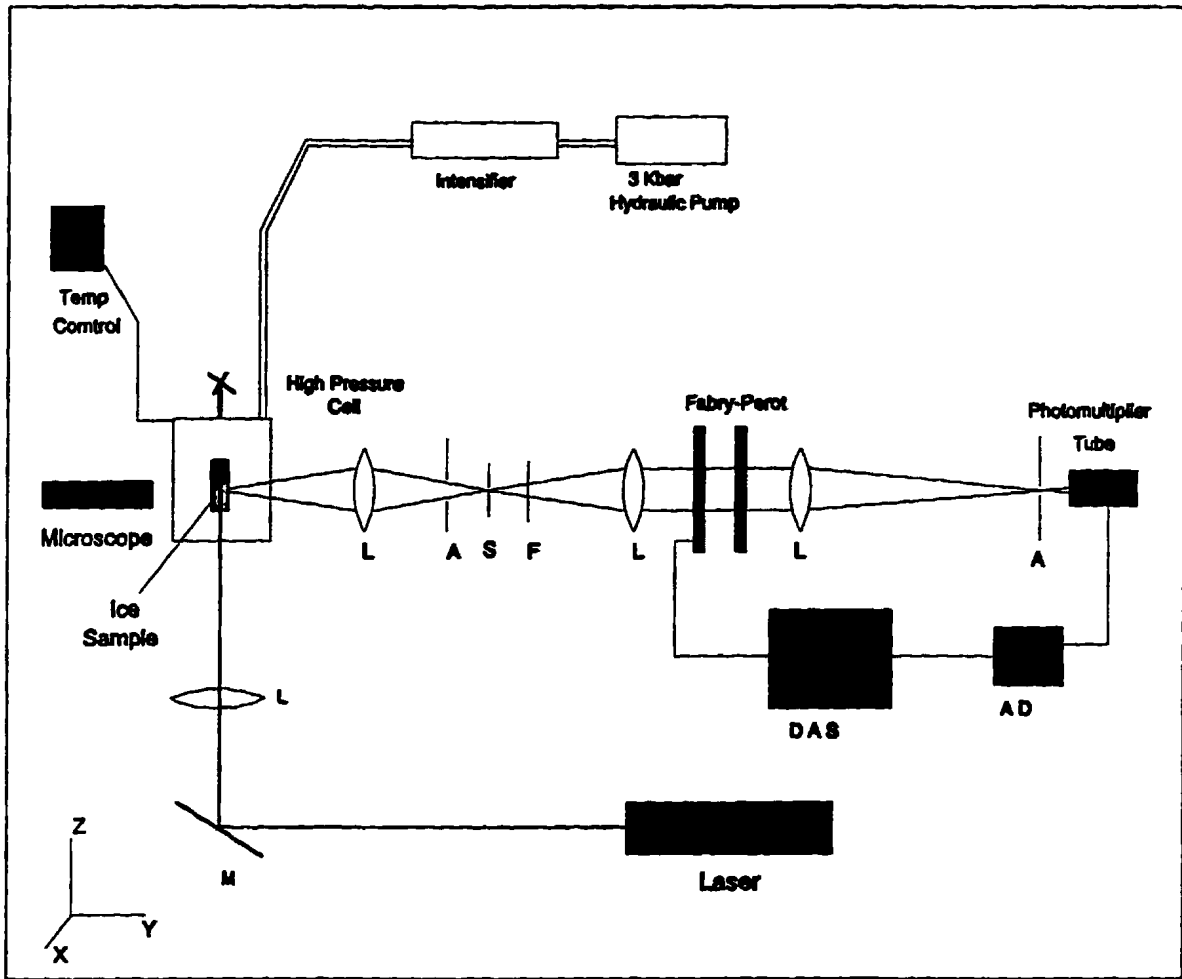
sound may be calculated using the measured frequency shift and the Brillouin equation. The Brillouin equation shows that, (1)  $\Delta\omega_{\max}$  occurs in the backscattering geometry when the scattering angle  $\theta = \pi$ , and, (2)  $\Delta\omega \rightarrow 0$  as  $\theta \rightarrow 0$ . It should be noted that the magnitude of  $k_i$  is only  $\sim 10^5 \text{ cm}^{-1}$  so that the longest phonon wave vector as determined by the Bragg condition is  $q \sim 2 \times 10^5 \text{ cm}^{-1}$ . Hence only excitations of very long wavelength, *i.e.*  $q$  vectors close to the Brillouin zone centre, are observed, and to a very good approximation,  $k_s \sim k_i$ . In the limit of  $q \rightarrow 0$  no Brillouin doublets are observed, since the frequency of acoustic waves near the zone centre behave as  $\omega = Vq$ . Therefore at  $q=0$  the acoustic wavelength is infinite and represents a translation of the crystal as a whole. In addition, the frequency of the acoustic modes approach 0 as  $q \rightarrow 0$  resulting in the Brillouin doublet being very close to the large central peak, this requires that spectrometers have very high resolution typically greater than 0.5 GHz.

### ***2.3 EXPERIMENTAL APPARATUS***

A schematic representation of the experimental apparatus is shown in Fig. 2.3. The components of the optical set-up have been discussed in detail by several authors.<sup>101-104</sup> The laboratory frame of reference is given by the arrows indicated. The laboratory y-axis is defined by the beam from a helium-neon laser directed along the axis of the Fabry-Perot interferometer.

### **Figure 2.3 Experimental Set-Up**

**Schematic of experimental set-up and geometry. The ice sample is contained within the high pressure cell and cryostat; lenses, apertures and filters are indicated by, L, A and, F, respectively; the spatial filter is indicated by S; the mirror is indicated by M. The coordinate system is shown in the lower left.**



The pressure apparatus mainly consisted of a hydraulic system used to pressurize the chamber containing the ice samples. The pressure transmitting fluid was Monoplex™ (dioctyl-sebacate) which is an optically transparent synthetic oil. In addition to being optically transparent, the large molecular size of Monoplex reduced the probability of forming high pressure clathrate hydrates. The freezing point of Monoplex is  $\sim -65^{\circ}\text{C}$  at atmospheric pressure. However, the oil often froze at  $-35^{\circ}\text{C}$  at pressures higher than  $\sim 4.5$  kbar. Therefore, when working at higher pressures, the freezing temperature was reduced by mixing the oil with varying concentrations of isopentane, which has a freezing temperature of  $\sim -153^{\circ}\text{C}$  at atmospheric pressure. Despite an isopentane concentration of nearly 75% the hydraulic fluid still froze at pressures above of 8.0 kbar at  $T \sim -5^{\circ}\text{C}$ .

A 3 kbar hand pump supplied hydraulic oil to the low pressure side of a 20 kbar intensifier. The pressure was measured using a Heise pressure gauge on the low pressure side and it was determined that the intensifier then increased the pressure by a factor of 16 by calibrating using a calibrated manganin wire pressure gauge on the high pressure side. The intensifier fed hydraulic oil into the high pressure cell as described in Section 2.3.1. The high pressure cell was placed inside a plexiglass cryostat which was evacuated and cooled thermoelectrically. In the course of the experiment two different Brillouin setups were used. In each, light was provided by one of two single mode argon ion lasers, (1) a Coherent Innova 90 and (2) a Spectra Physics Series 2000. Both beams were of better than 10 MHz bandwidth centred on 514.5 nm and the laser power was set at between 30 mW and 50 mW throughout the experiment. As illustrated in Fig. 2.3, the

laser beam was focused by a lens L ( $f = 30$  cm), reflected by mirror M through the bottom windows of the cryostat and high pressure cell then into the single crystal sample. Light scattered at  $90^{\circ} \pm 0.2^{\circ}$  was collected through a side window of the high pressure cell and cryostat by lens L ( $f = 45$  cm). The scattering cone was defined by aperture A ( $d = 0.2$  cm), placed behind the collecting lens. The light was then spatially filtered at S by lenses  $L_3$  and  $L_4$ , and the parallel light was then filtered through a narrow band-pass filter of 10 nm bandwidth centred on the laser line. This prevented other spectral components from entering a piezo-electrically scanned triple pass Fabry-Perot interferometer discussed in greater detail in section 2.3.2. The spectral components were then focused by a lens L,  $f = 80$  cm, onto an aperture A,  $d = 600$   $\mu\text{m}$ . The signal was then detected by a cooled ITT FW 120 photomultiplier tube PM set in photon counting mode. The signal from the photomultiplier was fed into an amplifier-discriminator AD (Princeton Applied Research, Model SSR 1120). The threshold of the discriminator was such that only peaks produced by the photomultiplier tube above a predetermined value were passed. The signal was amplified and sent to the Burleigh data acquisition system, (DAS -1), which counted the photons as a function of channel number. The DAS also controlled the ramping voltage to the piezo-electric transducers scanning the Fabry-Perot.

During crystal growth light from an incandescent bulb placed on the Fabry-Perot side of the cryostat was used to illuminate the sample. A microscope was focused inside the cryostat on the sample. A video camera and monitor were set up such that the sample in the high pressure chamber could easily be viewed through the microscope. This

enabled the sample to be viewed during the crystal growth.

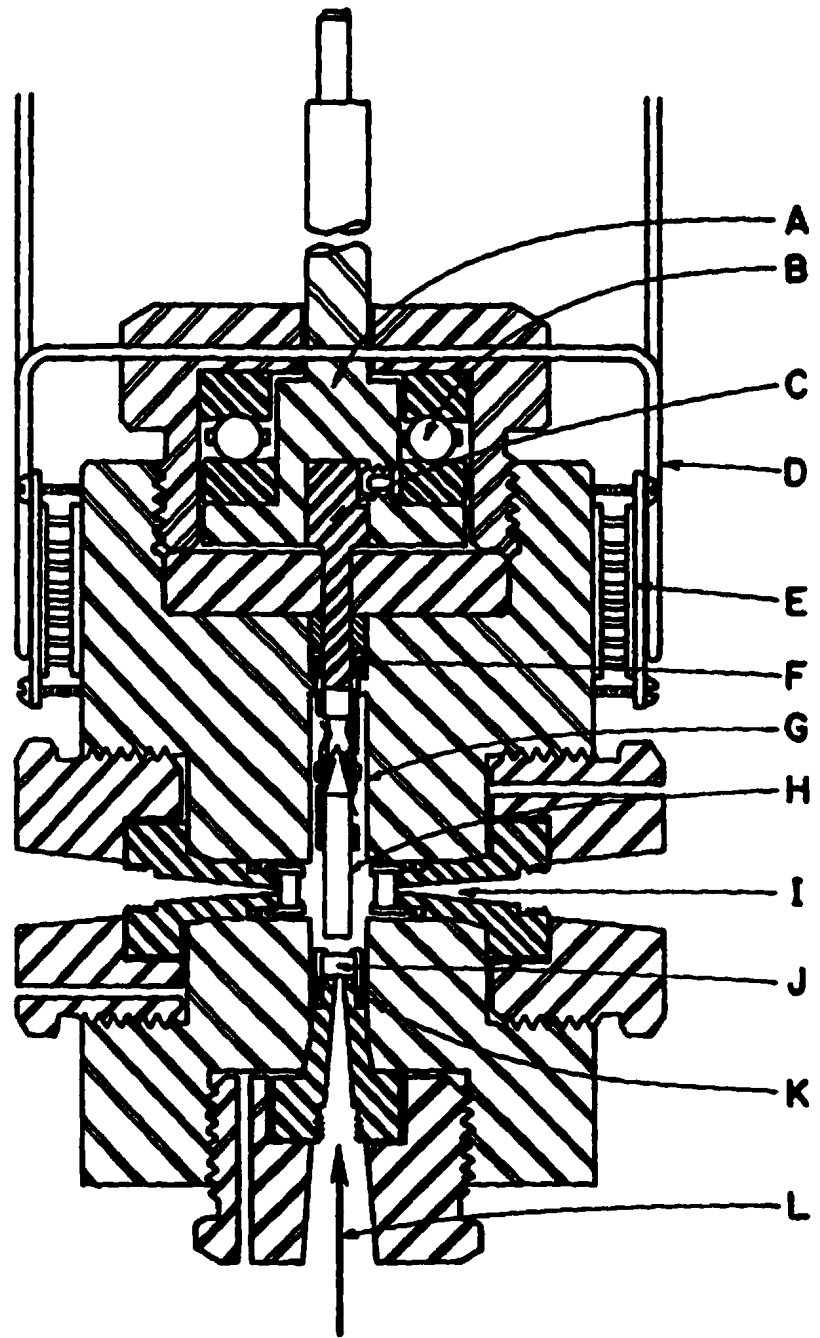
### ***2.3.1 High Pressure Cell***

The high pressure cell has been discussed in other reports<sup>105</sup> and is illustrated schematically in Fig. 2.4. The cell was designed and constructed at the National Research Council of Canada in Ottawa and shipped to Memorial for completion. It essentially consists of a 5x5x7 cm block of hardened 300 maraging steel in which two orthogonal intersecting bores have been drilled. The bore parallel to the long axis formed the high pressure chamber, G, and the bore parallel to one of the short axes formed the viewing ports, I. The bottom of the long bore and the two ends of the short bore have been fitted with windows, J. All three windows were made of glass and sat on optically flat mounts. A conically shaped hole in the centre of the mount minimized the load supported by the glass while under pressure and formed a viewing window 1.8 mm in diameter. Upon pressurization, windows were forced against the optically flat mounts preventing oil leaks. The windows were held in place by threaded, hardened beryllium copper caps which fit over the window and fastened to the mount. An O-ring, K, formed a seal between the mount and the inside of the bore. Backing rings were used to prevent the O-rings from being forced out upon pressurization. The mounts were held in place by large hardened 300 maraging steel gland nuts. The bottom window allows the laser beam to enter the high pressure chamber and was used for inserting and removing samples.

A specially designed rotation stem, A, allowed samples to be rotated through 360° about

## **Figure 2.4 High Pressure Cell**

Schematic of the high pressure cell; A, rotation stem; B, bearing assembly; C inner rotation stem; D, brass rods connecting the cell to the plexiglass thermal insulator; E, Peltier cells; F, O-ring; G, high pressure chamber; H, glass cell containing ice sample; I, port for collecting spectra and viewing samples; J, quartz windows; K, O-ring; L, laser beam. The scale is approximately 1:1.3.

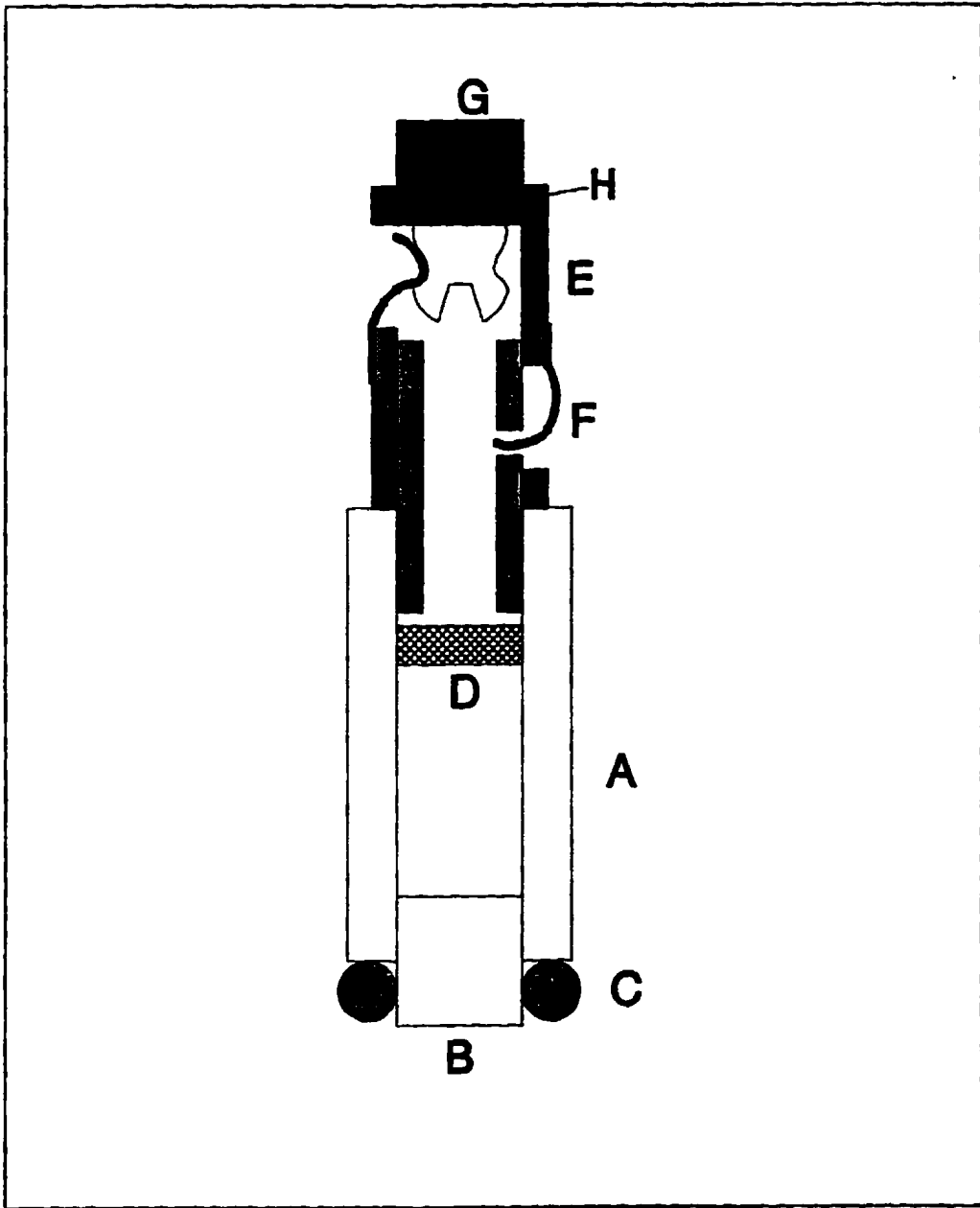


the laboratory z-axis while under pressures up to 10 kbar. The inner stem, C, contained a head at one end which protruded into the high pressure chamber and was designed so that the brass coupling and glass sample containment cell could be removed through the bottom window. The bottom of the stem head contained a small dimple which was painted black so that the laser beam, after passing through the sample would not be reflected. An O-ring and backing rings, F, were used to seal the stem against the inside of the bore. Sitting on the outer stem assembly was an annular ring with a concentric track machined in its upper surface in which sat a set of stainless steel bearings, B. Above the bearings was another annular ring with a similar bearing track machined on its lower side. This entire assembly was held in place by another large heat treated gland nut. Upon pressurization the inner stem would force the outer stem against the bearings and the gland nut. The bearing assembly would permit the rotation of the stem under pressure. Without the bearings the frictional force between the two metals would be so great that rotation of the sample would be impossible even under modest pressures.

Figure 2.5 illustrates the sample containment cell and coupling. A small sample cell, A, made of a thick walled glass tube attached to the rotation stem, G, by a small machined brass coupling, E. The cell was 1.3 cm long with an inner diameter of 4 mm. It was friction fitted to the brass coupling by two prongs which partially extended into the glass tubing. The friction between the glass and prongs was sufficient to prevent slippage during rotation of the stem even at the highest pressures. This was confirmed for each crystal by comparing Brillouin spectra collected before and after a complete 360° sample

### **Figure 2.5 Sample Containment Cell**

**Glass sample containment cell; A, glass tube; B, fire polished glass plug; C, copper ring for gripping glass cell; D, silicone disk; E, brass coupling; F, retaining pin; G, inner rotation stem; H, set pin.**



rotation. The bottom of the glass tube was fitted with a fire polished glass plug, B, held in place with silicone sealant. The optically clear plug permitted the laser beam to be readily transmitted into the sample. The position of the glass plug relative to the viewing windows was critical. In order that the seed crystal be seen during sample growth, the bottom of the cell had to be visible through the side windows with the aid of a microscope and video camera. In addition, the plug could not cover so much of the window that the laser beam could not be seen passing through the bulk ice sample. This means that the plug could cover no more than the bottom 1/3 of the 1.8 mm diameter window. This strict constraint meant that great care was necessary when inserting and removing the glass plug.

The orientation of the brass coupling relative to the rotation stem was fixed by a small set pin on the inner rotation stem assembly (see H, Figure 2.5). Once while trying to rotate the samples under high pressure the load supported by the pin was sufficient to cause failure. This required that the entire cryostat and high pressure cell be dismantled and the pin replaced with harder stainless steel.

The high pressure cell was placed inside a cryostat formed by a plexiglass pipe of inner diameter –16 cm. The bottom of the cryostat was formed by a brass plate sealed against the inside of the plexiglass tubing with an O-ring. A large quartz window in the centre of the brass plate allowed entrance of the laser beam. One of the side windows consisted of a 2.5 cm hole in the plexiglass pipe covered with a quartz disk held in place with

silicone sealant. The scattered light was collected through this window. The opposite window was a similar hole through which the microscope was inserted and focussed into the high pressure chamber. This permitted viewing the sample during crystal growth.

The high pressure cell was fixed to a plexiglass plate by means of four brass rods. The plexiglass plate was, in turn, bolted to the top brass plate of the cryostat. The plexiglass plate served as a thermal barrier between the high pressure cell and the top brass plate. The top brass plate was machined and fitted with the appropriate feed-through apparatus for the rotation stem, high pressure tubing, and electrical connections. The inside of the cryostat was evacuated to thermally insulate the high pressure cell from the room.

The cell was cooled using four Peltier thermoelectric modules with the cold side directly fixed to the side of the pressure cell. The warm sides of the Peltier cells were placed in thermal contact with copper plates which were cooled by a mixture of methanol and water at  $-15^{\circ}\text{C}$  circulating through attached coils. The temperature was measured to within  $0.05^{\circ}\text{C}$  by a calibrated Lakeshore cryogenics platinum resistance thermometer fixed directly to the outside of the high pressure cell. The temperature was controlled, to within  $0.05^{\circ}\text{C}$ , by adjustment of the input current supplied to the Peltier cells. It was necessary at times to adjust the temperature of the cell by adjusting both the coolant temperature and the current through the Peltier modules. However, the adjustment of the current through the Peltier modules provided more sensitive control over the high pressure cell temperature and this was the only adjustment made during the growth of single

crystals.

### 2.3.2 Fabry-Perot Interferometer

The spectral separation between the elastically scattered Rayleigh peak and the inelastically scattered acoustic peaks for the ice phases studied is of the order 10 GHz. In general, the unshifted peaks were much more intense than the acoustic peaks; for example, in the present study the typical unshifted peak was 2000 times more intense than the longitudinal acoustic peak. In order to investigate the components of such a spectrum requires an instrument of very high resolution, contrast and finesse. The modern Fabry-Perot interferometer is well suited to make such measurements, therefore a brief summary of the general features of the Fabry-Perot is given.<sup>106</sup>

The Fabry-Perot consists of two parallel mirrors with reflectivity of typically more than 90% and flat to within  $\lambda/200$ , and separated by a distance  $d$ . A beam of coherent monochromatic laser light incident on the mirrors undergoes internal reflection and hence interference. The intensity profile of emerging beam when projected onto a screen is described by the well known Airy function<sup>107</sup> given as,

$$I(\delta) = \left(\frac{T}{1-R}\right)^2 \frac{1}{1 + 4\frac{R}{(1-R)^2} \sin^2\left(\frac{\delta}{2}\right)} \quad . \quad 2.30$$

The phase difference between two transmitted beams in terms of  $n$  (refractive index of medium separating the mirrors),  $d$  (distance between the mirrors),  $\alpha$  (angle of the incident ray from the optic axis), and  $\Lambda$  (wavelength of the incident light) is written as,  $\delta = (2\pi/\Lambda)$

$2nd \cos \alpha$ . The maximum intensity then occurs when the phase difference of the transmitted beam is an integral multiple of  $\Lambda$ . For an extended source, the pattern produced by an image projected on a screen forms a set of concentric rings described by the equation,

$$2nd \cos(\alpha) = m\Lambda \quad . \quad 2.31$$

Considering the case in which air is the medium between the plates ( $n = 1$ ) and the incident light is collimated such that  $\alpha = 0$ , this equation reduces to  $2d = m\lambda$ , where  $m$  is called the order of interference. Since there is no angular dependence only the central spot is visible during constructive interference. In the spectrometer used in the present study the plate separation is varied by applying a ramping voltage to piezo-electric transducers. The Fabry-Perot thus acts as a frequency-varying narrow-bandpass filter, *i.e.* only light with a wavelength satisfying the above equation constructively interferes in the cavity and therefore emerges from the spectrometer.

If the distance between the two plates is held constant, the wavelength change required to move the order of interference from  $m$  to  $m+1$  can be easily calculated. This wavelength change is known as the free spectral range (FSR). The FSR may equally be stated as the spectral separation between corresponding features in consecutive orders of the Fabry-Perot. To illustrate this, suppose  $\Delta\Lambda$  is the FSR in units of wavelength, this means that the  $m - 1$  order fringe for some wavelength  $\Lambda$  will be the order  $m$  for  $\Lambda + \Delta\Lambda$ . This may be written as  $(m-1)\Lambda = m(\Lambda + \Delta\Lambda)$ . Solving for  $\Delta\Lambda$ , using equation 2.31 and expressing the result in terms of frequency the FSR is given by  $\Delta\nu = c/(2d)$ . In the

present experiment the FSR was chosen so that there was no overlap of spectral components.

The ratio of the full width at half maximum of the unshifted peak and the FSR is called the finesse. The finesse may be calculated by noting that the phase half-width of the unshifted peak at half its maximum ( $I/2$ ) may be found by setting  $4R/(1-R)^2 \sin^2(\delta/2) = 1$  in Eq. 2.30 and solving for  $\delta$ . The phase separation between two consecutive unshifted peaks is  $2\pi$ . The finesse is, therefore,  $F = \pi(R)^{0.5}/(1-R)$  where  $R$  is the reflectivity of the plates. Note that the finesse is dependent on the reflectivity and increases rapidly as  $R$  approaches unity. This is known as the reflectivity finesse and the precise value of the finesse is always less than this value due to surface roughness of the mirrors and misalignment. In fact as  $R$  approaches 1 the finesse approaches a limit dependent on the surface roughness of the mirrors.

The ability of a spectrometer to distinguish between two very close peaks is called the resolving power and can be expressed as  $\Lambda/\Delta\Lambda$ , where the spectrometer can just resolve lines of wavelengths  $\Lambda$  and  $\Delta\Lambda$ . One commonly used definition of "just resolved" states that, "two symmetrical profiles are just resolved when their maxima are separated by their full width at half maximum".<sup>107</sup> This can be written in terms of the finesse as,  $\Lambda/\Delta\Lambda = m F$ . Note that Eq. 2.31 states that "m" is directly proportional to the plate separation  $d$ , this implies that the resolution may be increased by increasing the distance  $d$ . Increasing the plate separation, however, decreases the FSR.

The ability of the instrument to detect very weak signals in the presence of strong signals is called the contrast,  $C$ . It may be defined from the Airy function as the ratio of the maximum intensity to the minimum intensity, thus  $C = I_{\max}/I_{\min} = 1 + 4 F^2 / \pi^2$ . It is important that the Fabry-Perot have a contrast as high as possible in order that the very weak transverse acoustic peak be distinguished from the very strong unshifted peak. The contrast of a Fabry-Perot may be significantly increased by passing the light through the interferometer several times. In the present study the scattered light was reflected back through the Fabry-Perot three times by displacing the successive passes laterally using retro-reflectors. The Airy function for a multipass Fabry-Perot may be found by raising the single pass Airy function to the power  $m$ , where  $m$  is the number of passes. The contrast of a multipass Fabry-Perot is therefore  $C_m = (C_1)^m$  and the multipass finesse may be expressed as  $F_m = F_1 (2^{1/m} - 1)^{-1/2}$ .

In the following chapters the details of the present Brillouin spectroscopic experiments on the phases III, V and VI will be given. Chapter III and V presents the elastic properties of ice III at -17 °C and ice VI at -2 °C, respectively, at various pressures. Chapter IV presents the elastic properties of ice V at 3.0 kbar and -35 °C.

# **CHAPTER III**

## **Single Crystal Growth and The Elastic Constants of Ice III**

### ***3.1 DETERMINATION OF THE ELASTIC CONSTANTS***

In all, three crystals of ice III were studied in the present experiment. The first two were studied at constant temperature and pressure,  $-20^{\circ}\text{C}$  and 2.2 kbar respectively. The first crystal was used to initially determine the 6 independent elastic constants,  $C_{11}$ ,  $C_{33}$ ,  $C_{44}$ ,  $C_{66}$ ,  $C_{12}$  and  $C_{13}$ . The second crystal was used to independently verify the elastic constants found using crystal # 1. The third crystal was used to study the variation of the elastic constants between 2.2 kbar and 3.0 kbar at  $-20^{\circ}\text{C}$ . From the single crystal elastic constant data, bulk polycrystalline elastic properties, such as Young's modulus,  $E$ , the Lamé constants,  $\lambda$  and  $\mu$ , and Poisson's ratio,  $\sigma$ , were calculated in a manner described in Section 2.1.3. The calculated polycrystalline elastic properties are compared with previously obtained values measured directly from polycrystalline samples. Agreement was found to be exceptionally good.

The Brillouin equation, described earlier, is an expression which gives the frequency shift associated with the interaction of light with sound waves propagating within the sample. The refractive index,  $n$ , the wavelength of the incident light,  $\lambda$ , the scattering geometry, and the acoustic velocity are required as parameters of the Brillouin equation. The

wavelength  $\lambda$  is accurately fixed by setting the laser to single mode operation (in the present study  $\lambda=514.5$  nm),  $n$  is calculated in the following section, spectra were collected in  $90^\circ \pm 0.2^\circ$  scattering geometry and the acoustic velocity may be calculated by finding the eigenvalues,  $\rho V^2$ , of the Christoffel determinant derived in section 2.1.2. The calculated frequency shifts,  $v^{\text{calc}}$ , corresponding to the observed experimental frequency shifts,  $v^{\text{obs}}$ , may be compared and used to measure the accuracy of the elastic constant parameters. Through the appropriate adjustment of the elastic constant parameters the difference between  $v^{\text{calc}}$  and  $v^{\text{obs}}$  may be minimized. This is the essence of the  $\chi^2$  non-linear least squares<sup>108</sup> fitting procedure described in section 3.1.4.

### ***3.1.1 Density and Refractive Index of Ice III***

The pressure dependence of the density of ice Ih, II, III, V and VI were extensively studied by Gagnon, *et al.*<sup>31</sup> in a separate experiment on the apparatus used in the present study. In that experiment the density was measured directly from changes in volume as the pressure was varied from 0 to 10 kbar, the uncertainty was estimated to be 0.1%. The density data, measured as a function of pressure within each phase, were fitted to either linear or quadratic polynomials. The resulting linear equation for ice III is quoted below

$$\rho_{\text{iceIII}}(P)_{\text{g cm}^{-3}} = 1.1321 + 1.2057 \times 10^{-2} P_{\text{kbar}} . \quad 3.1$$

The units of Eq. 3.1 are given by the subscripts. It should be noted that the density data used to obtain the above equation were collected at  $T = -35^\circ\text{C}$ . The densities calculated by this expression are considered accurate at  $T = -20^\circ\text{C}$ . The density difference estimated

thermal expansion of ice Ih over the same temperature range is about 1 % and does not change the best fit elastic constant values. The same is true for ice V and ice VI. At P = 2.2 kbar the density is calculated to be 1.1586 gm cm<sup>-3</sup>.

The refractive index of ice VI has been calculated by Polian *et al.*<sup>76</sup> It was assumed that the refractive index  $n(\rho)$  is related to the Eulerian strain  $\epsilon$  through the equation<sup>109</sup>

$$n(\rho_0) - n(\rho) = A\epsilon , \quad 3.2$$

where  $\rho$ ,  $\rho_0$ ,  $n(\rho)$  and  $n(\rho_0)$  are the density under pressure, the density at ambient pressure, the refractive index under pressure and at ambient pressure, respectively. The Eulerian strain  $\epsilon$  is given by

$$\epsilon = 0.5 \left[ 1 - \left( \frac{\rho}{\rho_0} \right)^{\frac{2}{3}} \right] \quad 3.3$$

and

$$n = 1.334 + 0.51(\rho^{\frac{2}{3}} - 1) . \quad 3.4$$

A was determined by fitting Eq. 3.2 to well known values of the refractive index and Eulerian strains of liquid water. These equations were then used to find the refractive index of ice VI. The resulting experimental and calculated values of the refractive index differed by less than 1% and are assumed accurate for the other phases and used in the

present analysis. The refractive index of ice III at  $\rho = 1.1586 \text{ gm cm}^{-3}$  was thus calculated to be 1.386.

### **3.1.2 Euler Angles**

The eigenvalues,  $\rho V^2$ , of Eq. 2.16 may be found if the direction cosines of the propagating acoustic wave with respect to the crystallographic axes (in the tetragonal system) are known. The ice crystals grown in the present study have arbitrary orientation with respect to the laboratory coordinates and hence there is no *a priori* knowledge of the direction cosines. The scattering acoustic wavevector is, however, well defined by the  $90^\circ$  scattering geometry as (0,1,1) in the laboratory frame. It is thus required that the scattering acoustic wavevector be transformed from the laboratory reference frame into the crystallographic reference frame. This may be done through a series of rotational transformations, given by the Euler angles<sup>10,11</sup>  $\theta$ ,  $\phi$  and  $\chi$ . Fig. 3.1 illustrates the Euler angle relationship between the two coordinate systems. The transformation is given by,

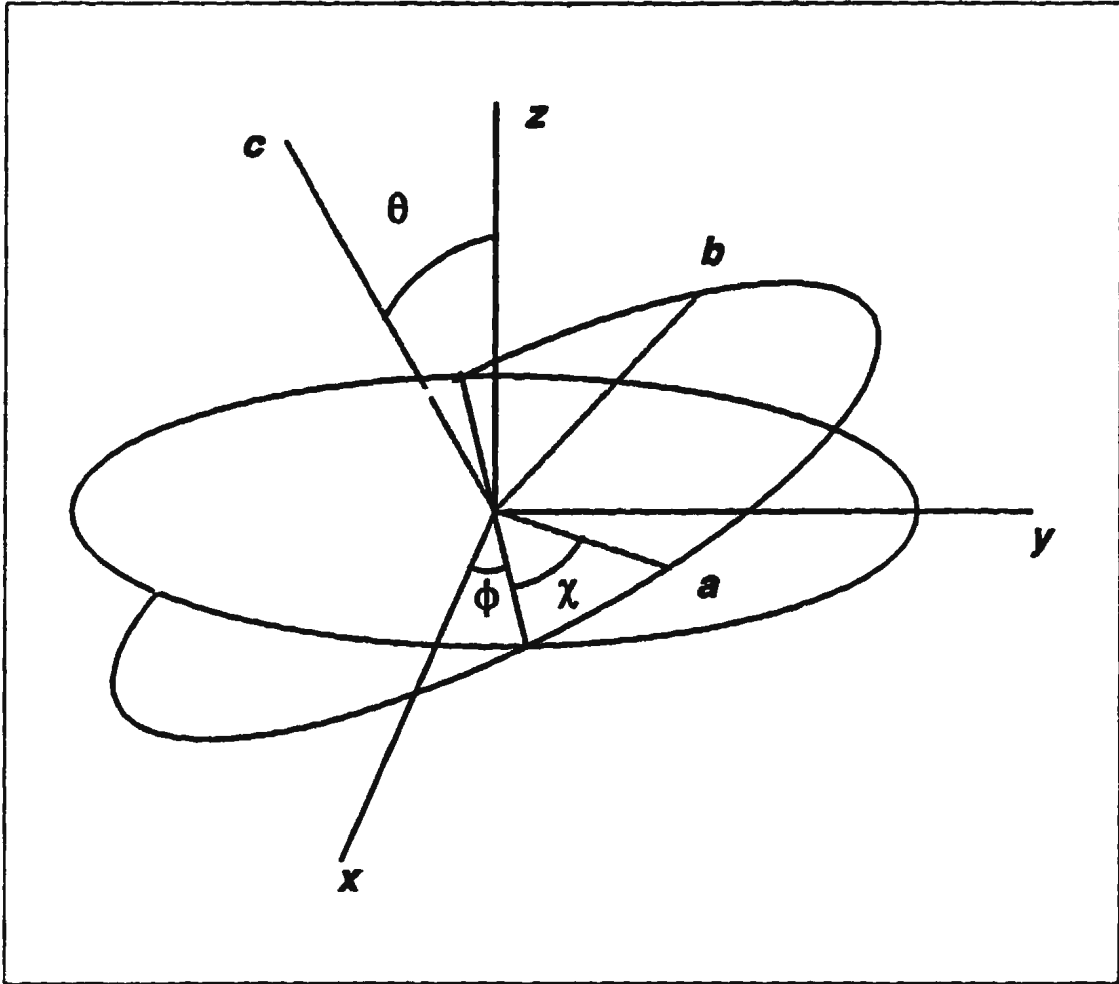
$$\mathbf{x}' = \mathbf{A} \mathbf{x} , \quad 3.5$$

where in the present case,  $\mathbf{x}$  and  $\mathbf{x}'$  are scattering wavevectors in the laboratory and crystallographic coordinate system respectively.  $\mathbf{A}$  is an orthogonal matrix formed by the combination of the three matrices representing the rotations illustrated in Fig. 3.1.

In the present experiment Brillouin spectra were collected at various orientations as the crystal was rotated about the laboratory z-axis. A spectrum was usually collected in

### **Figure 3.1 Euler Angles**

The Euler angles  $\theta$ ,  $\phi$  and  $\chi$  illustrate the relationship between the laboratory axes,  $x$ ,  $y$ , and  $z$  and the crystallographic axes  $a$ ,  $b$ , and  $c$ .



increments of  $\Delta\phi = 10^\circ$ . Note that rotations about the laboratory z-axis change the Euler angle  $\phi$  to  $\phi + \Delta\phi$  while keeping the other Euler angles constant. The problem of calculating the scattering acoustic wavevector is now reduced to finding the Euler angles relating the crystal frame to the laboratory frame. This is complicated by the fact that it is not possible to use the standard technique of Laue x-ray diffraction due to the small size and thickness of the necessary quartz windows. The crystals were however partially oriented optically by observing the polarization behaviour of light as it passes through the crystal.

### ***3.1.3 Determination of Sample Orientation***

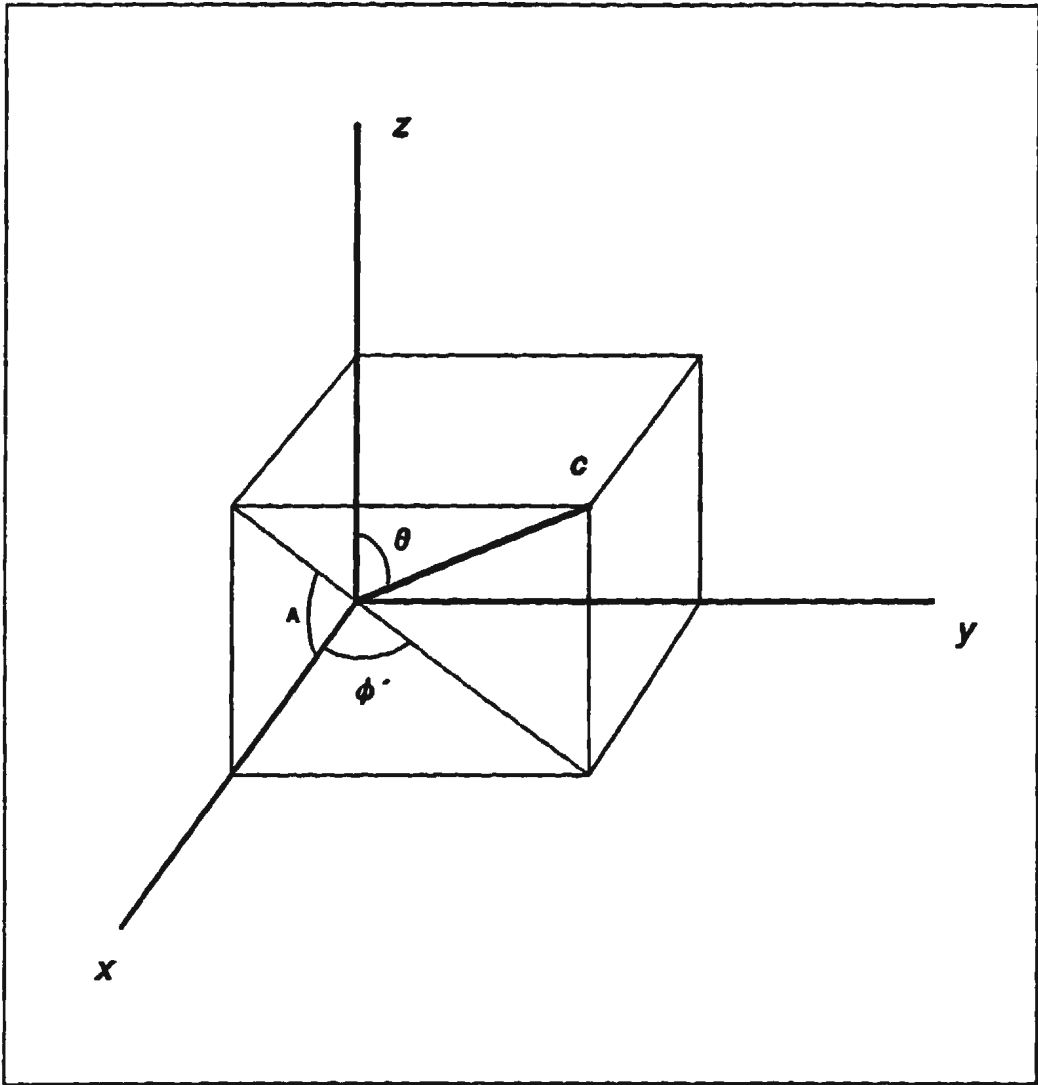
Crystalline substances which are optically anisotropic and exhibit two distinct indices of refraction are said to be birefringent.<sup>112-114</sup> Crystals are uniaxial and birefringent if the optical indicatrix is a biaxial ellipse of revolution, therefore the dielectric constant, or refractive index, has two distinct values forming the major and minor axes of an ellipsoid. Thus a light wave travelling in an arbitrary direction will encounter differing indices of refraction for different polarization directions. The optic axis is defined as the direction about which the atoms are arranged symmetrically, so that all polarizations of light experience the same index of refraction. When propagating along the optic axis light waves will experience the same index of refraction regardless of the polarization. In the tetragonal system this corresponds to the crystallographic c-axis.<sup>115</sup> In general, upon entering the crystal an unpolarized incident light beam is split into two orthogonal polarizations travelling with different speeds. One of the components is normal to the c-

axis and the other is mutually perpendicular or along the projection of the c-axis in the plane perpendicular to the direction of propagation. Therefore, light which travels along the y-axis and enters an arbitrarily oriented crystal will become polarized and have a component parallel to the projection of the c-axis in the xz-plane (see Fig. 3.2). For a complete discussion of birefringent behaviour in crystals see Jenkins and White.<sup>116</sup>

In the present experiment the entire cryostat containing a single crystal sample was placed between mutually orthogonal polaroid filters such that light entering the sample was polarized. The filter system was designed so that both filters may be rotated about the y-axis with their relative orientation fixed. Light from an unpolarised HeNe laser, which defined the laboratory y-axis, was passed through the polarizer and high pressure cell containing the single crystal sample. Upon entering the arbitrarily oriented crystal the polarized light was usually split into two mutually orthogonal components as discussed above. Hence, light emerging from the crystal had a component which was able to pass through the analyser and be projected onto a screen. As the crossed polaroid filters were rotated about the y-axis the plane of polarization of the incident beam also rotates. At some angle the plane of polarization becomes coincident with the projection of c-axis, and as the beam emerged from the crystal there was no component of vibration along the easy axis of the analyser and therefore little light was transmitted. This would be evidenced by a near complete extinction of light projected on the screen. The angle between the plane of polarization and the x-axis was then measured and called the "angle of extinction" A.

### **Figure 3.2 Birefringent Extinction**

**Illustration of the relationship between the crystallographic c-axis, the angles  $\theta$  and  $\phi'$ , and the extinction angle  $A$ , with respect to the laboratory axes (the Euler angle  $\phi = \phi' + 90^\circ$ ).**



From the Fig. 3.2 it is easily seen that the relationship giving  $A$ , measured clockwise from the positive  $x$ -axis, as a function of the angles  $\phi'$  and  $\theta$  is (note that the Euler angle  $\phi = \phi' - 90^\circ$ )

$$\cos(A) = \frac{\sin(\theta) \cos(\phi' + \Delta\phi)}{[\cos^2(\theta) + \sin^2(\theta) \cos^2(\phi' + \Delta\phi)]^{\frac{1}{2}}}, \quad 3.6$$

where  $\Delta\phi$  is the angle of rotation clockwise from the  $x$ -axis. Several extinction angle measurements were averaged at each  $\Delta\phi$  through a complete  $360^\circ$  rotation about the laboratory  $z$ -axis. These data are presented in Table 3.1 for each of the three crystals. Using this method it was possible to partially orient the crystal by fitting the Euler angles  $\theta$  and  $\phi$  to the measured extinction angles using a least squares minimization routine. The remaining Euler angle,  $\chi$ , was uniquely determined when the elastic constant parameters were fitted to the measured acoustic frequency shifts, see Section 3.1.4. The crystal orientation data are plotted in Fig. 3.3 (a), (b) and (c) along with the best fit curves for each of the three crystals studied. The quoted Euler angles refer to the orientation of the crystal at  $\Delta\phi = 0.0^\circ$ .

### ***3.1.4 Fitting the Elastic Constants***

Once the crystals were oriented it was possible to calculate the acoustic velocity, and frequency shifts, in crystallographic directions corresponding to each scattering vector of the experimental data. Unique elastic constants are then found by adjusting the parameters of the Christoffel determinant until the square of the difference between the observed and

**Table 3.1**  
**Extinction Angle versus Crystal Orientation Data**  
**Ice III**

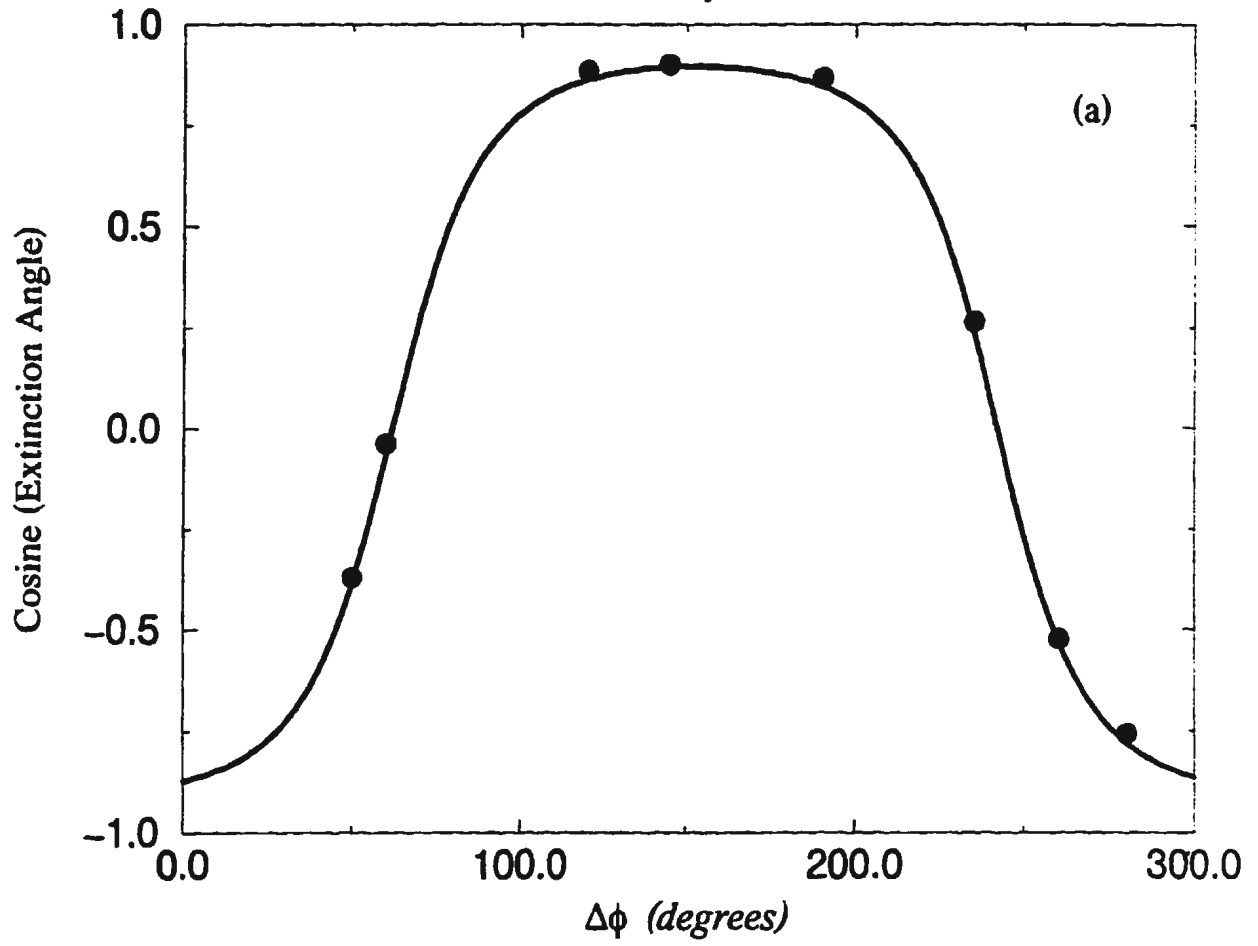
	$\Delta \phi$ (degrees)	cos(extinction angle)
<b>Crystal #1</b>		
1	50.0	-0.3697
2	60.0	-0.0384
3	120.0	0.8854
4	145.0	0.9018
5	190.0	0.8686
6	235.0	0.2639
7	260.0	-0.5210
8	280.0	-0.7570
<b>Crystal #2</b>		
1	30.0	0.3404
2	50.0	0.5563
3	90.0	0.7147
4	110.0	0.7346
5	150.0	0.5030
6	180.0	0.1616
7	210.0	-0.3264
8	240.0	-0.6148
9	270.0	-0.6730
10	290.0	-0.6441
<b>Crystal #3</b>		
1	10.0	-0.2113
2	40.0	0.0680
3	70.0	0.2840
4	100.0	0.3859
5	130.0	0.4242
6	160.0	0.3469
7	190.0	0.1977
8	220.0	-0.0732
9	250.0	-0.3007
10	280.0	-0.4051
11	310.0	-0.4399
12	340.0	-0.3173

### **Figure 3.3 Extinction angle vs. $\Delta\phi$**

Plots of the cosine of the extinction angle vs. rotation  $\Delta\phi$  about the laboratory z-axis, the solid circles represent the experimental data points and the smooth lines are the best fit curves. (a) Ice III crystal #1; (b) Ice III crystal #2; (c) Ice III crystal #3.

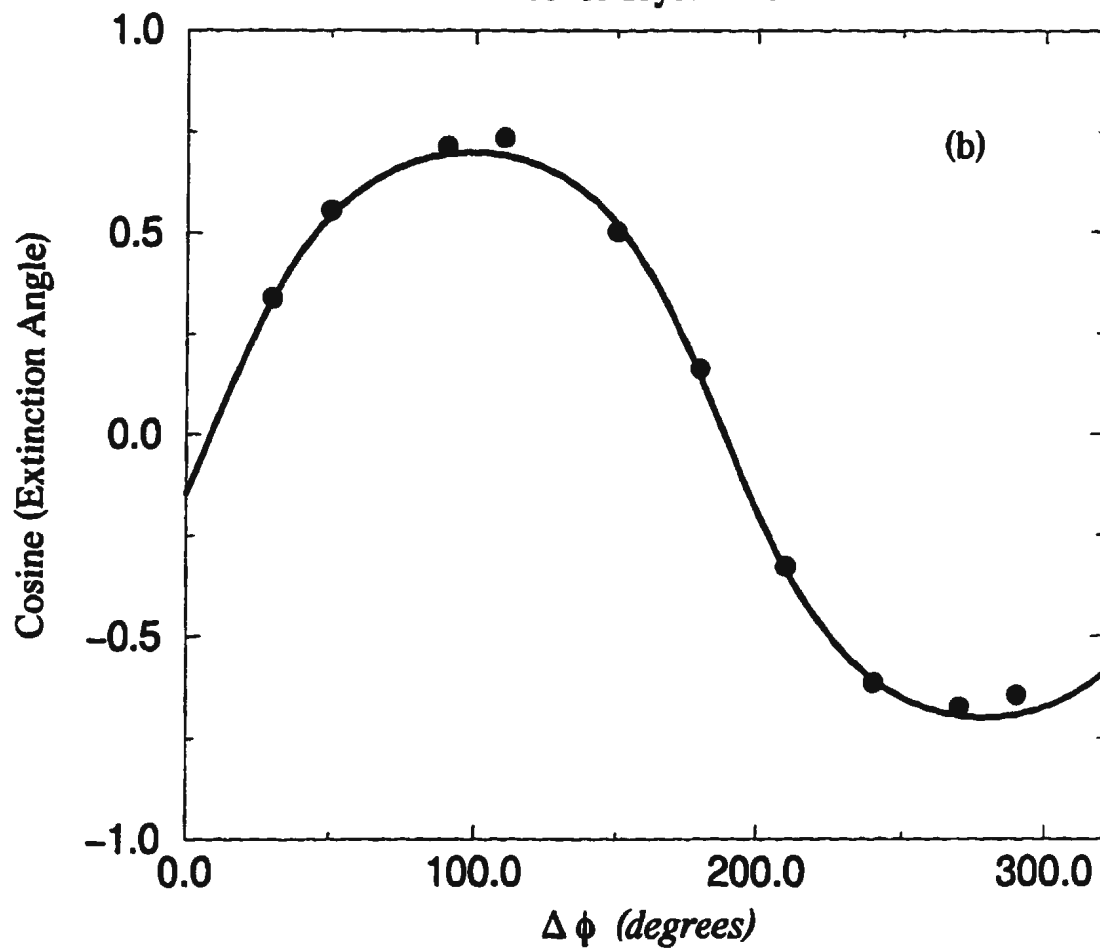
# Orientation Data

Ice III Crystal #1



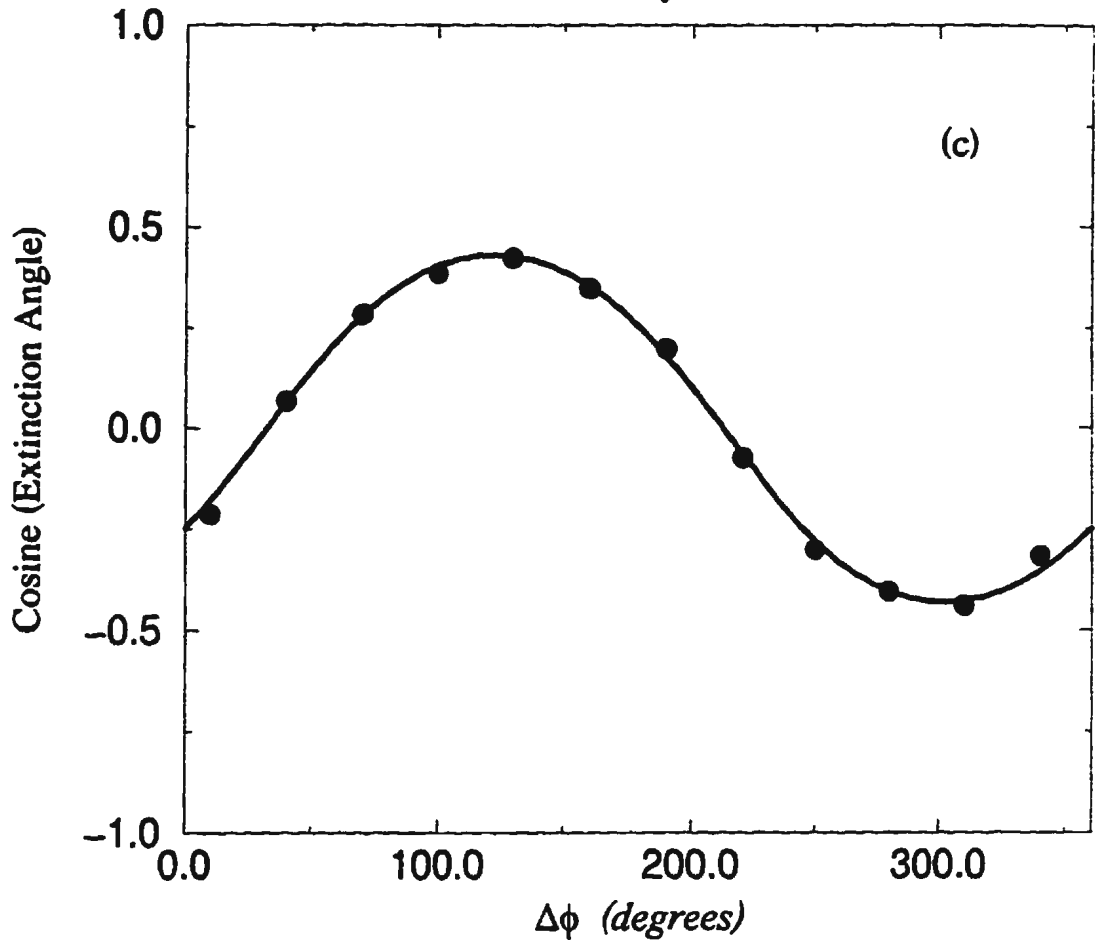
# Orientation Data

Ice III Crystal # 2



# Orientation Data

Ice III Crystal #3



the calculated frequency shift is minimized. In the non-linear least squares procedure the quantity which is minimized is given as

$$\chi^2(a_j) = \frac{1}{M-N} \sum \left[ \frac{v_i^{calc}(a_j, f_i, k_i) - v_i^{obs}}{\eta_i} \right]^2, \quad 3.7$$

where  $a_j$  are the  $j$  independent elastic constants, the sum over  $i$  covers all  $M$  observed frequency shifts,  $N$  is the number of parameters being fit and  $\eta$  is the standard deviation of the observed frequency shifts.

The minimizing computations were done by using the IMSL and NAG math subroutine libraries and the appropriate Fortran code was written. Systematic errors were primarily due to uncertainty in the refractive index, density, and scattering angles. The systematic errors in  $\rho V^2$  may be calculated using the Brillouin equation and are found to be less than 1%. Non-systematic errors were introduced due to uncertainties in the Brillouin frequency shifts and the orientation of the crystals. Calculation of the non-systematic errors requires the standard deviation of the individual frequency shifts,  $\eta_i$ . There was no practical method of determining  $\eta_i$ , therefore,  $\eta_i$  is assumed to be constant for all frequency shift measurements of the present experiments. The standard deviation,  $\eta$ , was estimated by requiring that  $\chi^2$  be equal to unity when  $\eta$  is equal to one standard deviation.

The non-systematic uncertainties in the elastic constants were calculated using the error matrix defined as,

$$(H^{-1})_{mn} = \left[ \sum \frac{\partial v_i^{calc}}{\partial a_n} \frac{\partial v_i^{calc}}{\partial a_n} \frac{1}{\eta_i^2} \right] a_i^*, \quad 3.8$$

where  $a_i^*$  are the best fit elastic constants. The uncertainties are given by the diagonal elements,

$$\Delta C_{ij} = (H_{ij})^{\frac{1}{2}}. \quad 3.9$$

The errors were calculated by a separate computer program written for the purpose of finding the derivatives of the Brillouin frequency shift with respect to the individual elastic constants.

### ***3.2 GROWTH OF SINGLE CRYSTAL SAMPLES***

Sample production for each of the phases, ice III, V, VI, was very similar. All ice samples were produced from triply distilled, degassed and deionized water, produced at National Research Council of Canada, Institute for Marine Dynamics in St. John's, Newfoundland, Canada. In addition, the water was boiled for approximately 20 minutes prior to use to ensure that all gases had been driven out of solution. Each of the ice phases studied shares a common phase boundary with liquid water. This allows single crystals of each of these phases to be grown from the liquid without being forced through

a solid-solid phase transition. Forcing crystals through a solid-solid phase transition by increase of pressure always resulted in single crystal samples shattering and becoming fine grained polycrystalline aggregates. Fig. 1.2, in chapter 1, illustrates the phase diagram of the high pressure phases of ice.

It was noted throughout this experiment that the boundary lines separating the high pressure phases of ice are not well defined. On several occasions samples of ice were super-pressurized, or supercooled, well into the stability field of a neighbouring phase. During the present experiment, early attempts to prepare single crystal samples of ice III involved pressurization of single crystals of ice Ih. Ice Ih samples were pressurized to as much as 3.5 kbar at  $T = -30^{\circ}\text{C}$  before the phase transition occurred. This is well above the stable pressure region of ice Ih. Ice V and VI were also produced by pressurizing single crystals of ice III and V respectively; again the pressure could be increased well into the stability field of the neighbouring phase before the transition occurred.

Such phase transitions from a metastable to a stable crystal structure always proceeded rapidly (*i.e.* complete transformation within 10s of nucleation). This rapid phase transition, in addition to the large volume changes, always resulted in the crystal shattering and producing a fine grained polycrystalline aggregate. It quickly became evident that single crystals could not be retained through solid-solid phase transitions, and that an alternate method of producing large single crystals would have to be developed. In addition, an attempt was made to produce a single crystal of ice II by slowly cooling a single crystal

of ice III to approximately  $-70^{\circ}\text{C}$  at pressures ranging from 2 - 3 kbar. Again ice III is metastable with respect to ice II at this temperature. The samples were left under these conditions for 2 weeks with no sign of an imminent phase transition as determined by the Brillouin frequency shift measurements. This was attempted at least 8 times.

It is quite likely that the lack of a suitable nucleation site in the single crystal lattice played a role in the degree of supercooling required before a phase transition would proceed. It was noted on several occasions that polycrystalline samples exhibited sharp and well defined, repeatable phase transition pressures and temperatures which agree well with those of the established phase diagram. Attempts were made to introduce a nucleation site by placing a sharp piece of glass in the cell. By growing a single crystal of ice III around the shard then slowly cooling the sample into the stability field of ice II it was hoped that the shard would act as an ice II nucleation site. After several days it appeared as though the shard of glass would not produce the required nucleation site. After 3 frustrating attempts it was determined that the cell would need modifications to successfully produce a large single crystal of ice II and the process was temporarily abandoned.

### ***3.2.1 Ice III***

Since it was impossible to retain single crystals through a solid-solid phase transition it was necessary to produce single crystal samples from the liquid state. This required that a seed be grown under very strict control of temperature and pressure into a high quality

single crystal suitable for Brillouin experiments. Such seeds are generally produced in one of two ways; (1) a seed crystal is produced from liquid at the bottom of the cell by setting a temperature gradient, (2) a polycrystalline sample is melted until a single crystal seed remains, and then a slow and controlled regrowth produces the desired single crystal. The second method proved to be most practical and required only minor modifications of the existing apparatus.

As mentioned above, polycrystalline samples of ice III could be easily produced by pressurizing readily available single crystals of ice Ih. This was the first method used to obtain polycrystalline samples of ice III. Samples of ice Ih did not transform uniformly throughout the bulk of the specimen but in a rather inhomogeneous manner allowing excessive amounts of hydraulic oil to penetrate the cracks before the sample fully annealed. Upon melting, large drops of oil adhered to the inside wall of the sample containment cell thus obscuring the view of the crystal. Fine droplets remained in suspension and resulted in a single crystal of very low quality and totally unsuitable for Brillouin scattering.

To reduce the amount of oil intrusion a thin disk of dry silicone sealant was placed in the cell on top of liquid water. The liquid water sample was then pressurized, at room temperature, to approximately 3.3 kbar, directly over the phase boundary of ice III (see Fig. 1.2). The cryostat and sample were then cooled to approximately  $-35^{\circ}\text{C}$  resulting in supercooled water which, after several hours, froze directly into a polycrystalline sample

of ice III. Using this method very little oil penetrated into the sample and the resulting grain size was on the order of 100  $\mu\text{m}$ .

The temperature of polycrystalline sample was then raised at constant pressure to  $-17\text{ }^{\circ}\text{C}$ . The pressure was then carefully reduced until the sample began to slowly melt. Melting continued until only a small ice seed remained, usually containing 3 or 4 crystallites. The sample was monitored with the aid of a video camera and microscope during the entire process until the seed size did not exceed 15  $\mu\text{m}$ . Then the pressure was slightly increased until the seed started to slowly grow. The light used to illuminate the sample produced a thermal gradient across the cell. The seed crystal of all ice phases tended to be at the cooler front of the glass containment cell and always grew toward the back. The light was shielded as much as possible to reduce heating effects. This also reduced the thermal fluctuations that could cause difficulty when trying to precisely control the temperature. The approximately 17% reduction in volume during freezing caused the pressure to be reduced as the sample grew and eventually caused the sample to start melting. The temperature and pressure were therefore constantly monitored and adjusted during the growth process. The entire freezing process typically took 6-8 hours.

Once the sample had completely frozen it was viewed between crossed polaroid filters at several orientations about the laboratory z-axis. Grain boundaries were evidenced by inhomogeneous extinction of light at the appropriate orientation of the polaroid filters. The resulting ice samples, which were rarely single crystals, usually contained 3 or 4

large grains. The growth process would, therefore, have to be repeated several times until a large single crystal of sufficient quality was obtained. Once a single crystal was successfully produced the pressure was increased to 2.2 kbar and the temperature decreased to  $-20^{\circ}\text{C}$ , just inside the ice III stability field. The entire process typically took one full day. The sample was then left for several hours to anneal fully. The process of crystal growth was recorded on video cassette. Fig. 3.4 illustrates the slow growth of a crystal from a single crystal seed, the time between successive frames is  $\sim 1$  min, the bright region in the central portion of each frame is due to a lensing effect produced by the cylindrical sample containment cell, the diameter of this region was approximately 1 mm. The crystal faces are readily seen and give an indication of the crystal quality.

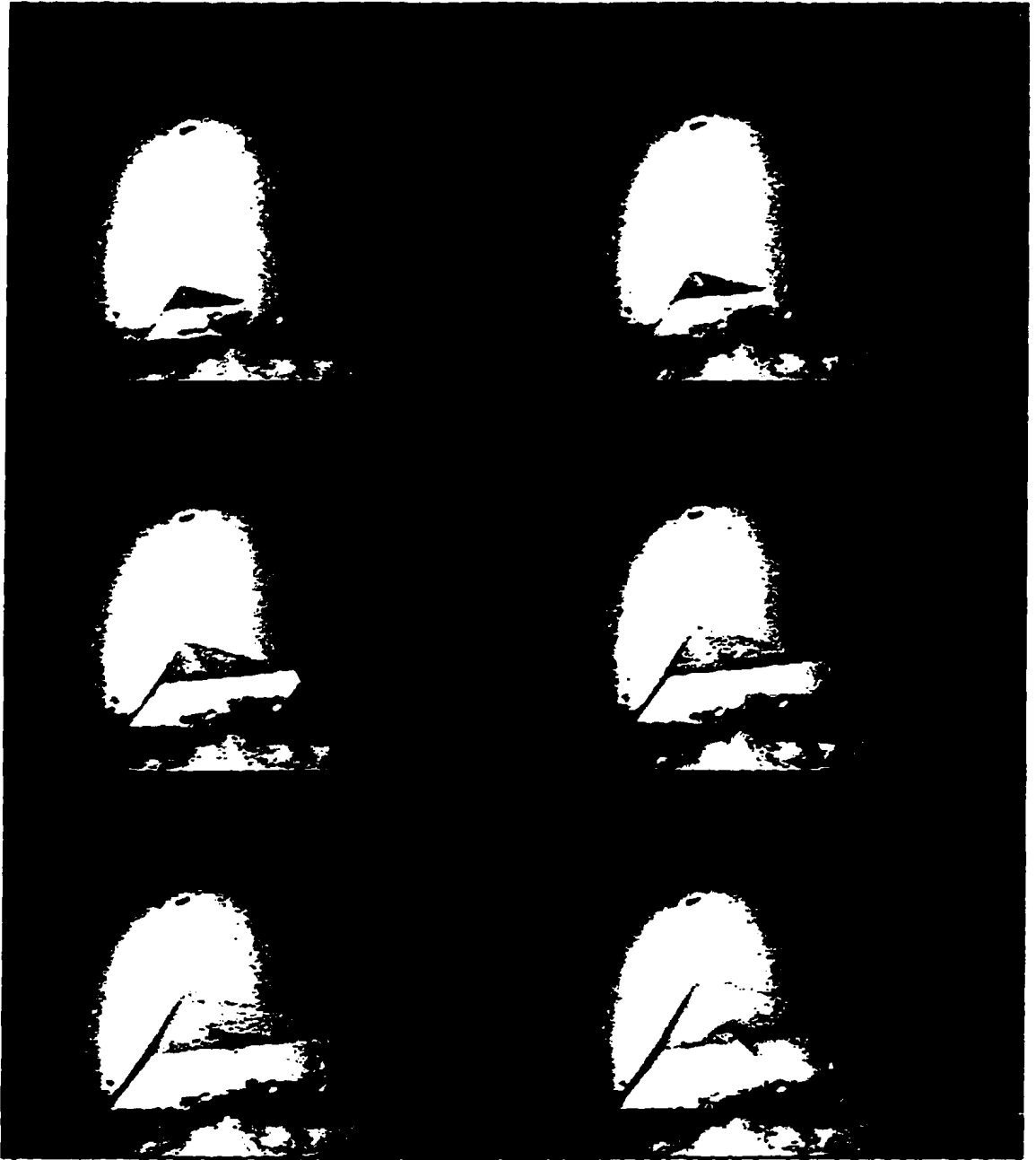
### ***3.3 RESULTS OF ICE III STUDIES***

Three samples of ice III suitable for Brillouin spectroscopy were successfully grown and as much data as possible collected and analyzed. The elastic constants were initially calculated using the first two crystals grown from which suitable spectra could be collected at  $T = -20^{\circ}\text{C}$  and  $P = 2.2$  kbar. The third crystal was used to investigate the pressure dependence of the elastic constants.

#### ***3.3.1 Frequency Shift Data and Elastic Constants of Ice III***

### **Figure 3.4 Growth of a Single Crystal of Ice III**

Time lapse images of a single crystal of ice III growing from liquid water. The images were produced by video taping the samples through a microscope. The seed crystal sits on the glass plug which forms the bottom of the cell and both are visible at the top of each frame. The cylindrical sample containment cell acts as a lens, thus the light entering is focussed to the center axis and appears distorted. The diameter of the bright central portion is ~1 mm. The time between consecutive frames is ~1 min.



For these initial studies a Coherent Innova 90 argon ion laser was used in single mode operation as discussed in the section 2.3. The free spectral range (FSR) was set to 36.36 GHz such that spectra were measured without overlap of components. Fig. 3.5 illustrates a typical Brillouin spectrum of crystal # 2 at  $\Delta\phi = 20^\circ$ . Two complete orders of the Fabry-Perot are shown. The L designates the frequency shift due to the quasi-longitudinal acoustic polarization, and  $T_1$  and  $T_2$  represent the frequency shift due to the two quasi-transverse polarizations. The longitudinal components were very sharp and give qualitative evidence of the very high quality of the samples. The ratio of the longitudinal peak intensity to that of the unshifted central peak was typically 1:100. The transverse acoustic peaks were of very weak intensity relative to the longitudinal peak, typically ratios were of the order 1:50. This resulted in the need to collect a single spectrum over 8-12 hours.

Brillouin spectra were usually collected in  $\Delta\phi$  increments of  $10^\circ$  or  $20^\circ$  through a complete  $360^\circ$  rotation. This resulted in a total of 149 frequency shift measurements from crystal #1 and #2 at  $P=2.2$  kbar and  $T=-20^\circ\text{C}$ . Frequency shift data were collected from crystal #3 at  $T=-20^\circ\text{C}$  between 2.5 and 3.0 kbar. Table 3.2 (a), (b) and (c) give the change in Euler angle  $\phi$  and the corresponding observed frequency shifts for crystal # 1, # 2 and #3. As a check of consistency, the elastic constants were fitted to the frequency shift data of crystal #1 and #2 separately. The agreement between the two independent systems, crystal #1 and #2, is remarkably good. The final elastic constant values were then found by combining all frequency shift data from both crystals and running the least squares routine. As a check of the Fortran code the elastic constants were determined from the

***Figure 3.5 Brillouin Spectrum of Ice III***

Brillouin spectrum of ice III crystal #2, at  $\Delta\phi = 20^\circ$ ,  $T = -20^\circ\text{C}$ ,  $P = 2.2$  Kbar, the FSR is 36.36 GHz. The longitudinal, transverse and central unshifted components are indicated by L,  $T_{1,2}$  and U respectively. Two complete orders of the Fabry-Perot are shown and lines indicated by  $T_1$  and  $T_2$  correspond to the central unshifted peak.

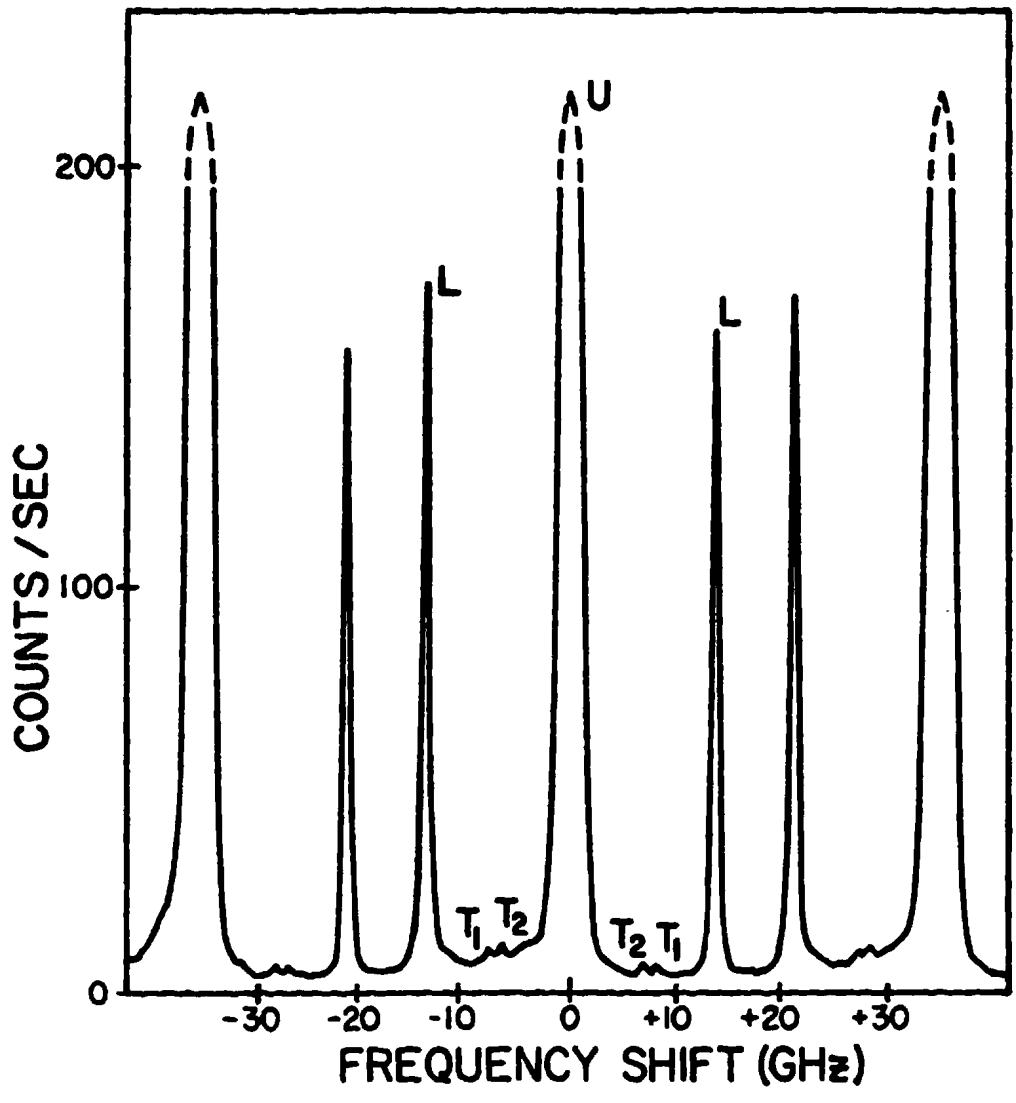


**Table 3.2 (a)**

**Brillouin Frequency Shifts (GHz) Ice III  
Crystal # 1 ( $\theta=64.2^\circ$ ,  $\chi=-19.2^\circ$ ,  $\phi=118.5^\circ$ )**

	$\Delta\phi$ (degrees)	L	$T_1$	$T_2$
1	0	14.94	-	6.28
2	10	14.99	-	-
3	20	15.02	-	6.05
4	30	15.07	-	-
5	40	14.88	7.34	6.21
6	50	14.61	-	-
7	60	14.42	7.59	6.94
8	70	14.10	-	-
9	80	13.87	-	-
10	90	13.90	-	-
11	100	13.96	8.26	-
12	110	14.18	7.91	-
13	120	14.33	7.41	-
14	130	14.61	-	6.98
15	140	14.70	-	6.77
16	150	14.70	7.38	6.60
17	160	14.56	7.39	6.47
18	170	14.24	7.40	6.28
19	180	14.14	-	-
20	190	13.83	7.22	-
21	200	13.49	7.28	6.64
22	210	13.11	7.49	6.77
23	220	12.79	-	6.83
24	230	12.57	-	6.98
25	240	12.47	-	7.07
26	250	12.57	-	7.25
27	260	12.76	-	-
28	270	13.01	-	6.83
29	280	13.43	-	-
30	290	13.56	7.59	6.55
31	300	13.80	7.72	6.60
32	310	14.06	7.77	6.73

	$\Delta\phi$ (degrees)	L	$T_1$	$T_2$
33	320	14.24	7.56	-
34	330	14.62	-	-
35	340	14.06	7.51	6.78
36	350	14.96	-	-

**Table 3.2 (b)**  
**Brillouin Frequency Shifts (GHz) Ice III**  
**Crystal # 2 ( $\theta=136.2^\circ$ ,  $\chi=45.4^\circ$ ,  $\phi=-8.7$ )**

	$\Delta\phi$ (degrees)	L	$T_1$	$T_2$
1	0	15.16	-	5.92
2	10	15.12	-	5.83
3	20	15.12	-	6.08
4	30	14.86	-	6.51
5	40	14.66	-	7.09
6	50	14.27	7.6	-
7	60	14.06	-	-
8	70	13.89	-	7.18
9	80	13.90	-	7.06
10	90	13.84	8.11	6.75
11	100	13.90	7.98	6.82
12	110	13.78	7.84	6.60
13	120	13.72	7.58	6.58
14	130	13.52	7.51	6.57
15	140	13.19	-	6.81
16	150	12.90	-	7.04
17	170	12.24	-	7.41
18	180	12.10	-	7.46
19	190	12.03	-	-
20	200	12.19	-	7.46
21	210	12.39	-	7.31
22	220	12.76	-	7.14
23	230	13.07	-	6.89
24	240	13.40	-	6.74
25	250	13.64	7.53	6.58
26	260	13.86	7.68	6.54

27	270	13.90	7.85	6.64
28	280	13.92	7.96	6.88
29	290	13.94	-	-
30	300	13.86	8.57	7.24
31	310	14.05	8.21	-
32	320	14.22	7.97	-
33	330	14.50	-	7.41
34	340	14.78	-	6.85
35	350	14.96	-	6.36

**Table 3.2 (c)**  
**Brillouin Frequency Shifts (GHz) Ice III**  
**Crystal # 3 ( $\theta=26.45^\circ$ ,  $\chi=-55.93^\circ$ ,  $\phi=157.38^\circ$ )**

	$\Delta\phi$ (degrees)	L	$T_1$	$T_2$
2.5 kbar				
1	0	14.30	7.79	-
2	20	14.82	7.34	6.33
3	40	14.94	7.22	6.12
4	50	14.84	7.32	6.29
5	60	14.72	-	6.69
6	70	14.32	7.51	-
7	80	14.08	7.89	-
8	90	13.92	8.19	6.79
9	100	13.86	-	6.62
10	110	13.83	8.07	6.62
11	120	13.84	7.66	6.62
12	130	13.80	7.45	6.63
13	140	13.55	-	-
14	160	13.19	7.16	-
15	180	12.83	-	7.01
16	200	12.64	7.27	-
17	220	12.76	7.03	-
18	240	13.03	-	6.78
19	260	13.59	7.30	-
20	280	14.07	7.01	-
21	300	14.21	7.43	6.59

22	320	14.08	7.92	-
23	340	13.99	-	-
<b>2.8 kbar</b>				
1	0	14.40	7.76	-
2	20	14.88	7.49	6.41
3	40	14.99	7.36	6.05
4	60	14.64	7.42	6.69
5	80	14.16	7.97	-
6	100	13.90	-	6.80
7	120	13.87	7.80	6.50
8	140	13.72	-	7.07
9	160	13.32	7.24	-
10	180	12.97	-	7.06
11	200	12.78	7.36	-
12	220	12.89	7.10	-
13	240	13.17	-	6.76
14	260	13.66	7.45	-
15	280	14.14	7.06	-
16	300	14.28	7.41	6.66
17	320	14.02	7.98	6.93
18	340	13.99	-	7.03
<b>3.0 kbar</b>				
1	0	14.45	7.85	7.00
2	20	14.95	7.42	6.43
3	40	15.06	7.46	6.18
4	60	14.68	7.48	6.61
5	80	14.29	7.84	-
6	100	14.02	-	6.82
7	120	14.08	7.78	6.62
8	140	13.86	-	7.09
9	160	13.45	7.25	-
10	180	13.09	-	7.11
11	200	12.93	7.34	-
12	220	13.00	7.22	-
13	240	13.28	-	6.84
14	260	13.68	7.43	-
15	280	14.19	7.05	-
16	300	14.35	7.47	6.67
17	320	14.24	8.00	6.90
18	340	14.06	-	6.96

acoustic data using commercially available software called Elcon and the results were found to be entirely consistent with that of the computer routine written for the present study. It should be noted that Elcon requires the direction cosines for the scattering acoustic wave be known *a priori*, this was not possible in the present study since the crystals could only be partially oriented (Euler angles  $\phi$  and  $\theta$ ) using the optical technique discussed in section 3.1.3. The Euler angles quoted in Table 3.2 were therefore supplied to the Elcon program.

The plots shown in Fig. 3.6 (a) and (b) graphically represent the frequency shift data collected from crystals # 1 and # 2 as a function of the Euler angle given by  $\phi + \Delta\phi$ . The solid circles are the experimentally determined points and the smooth lines were calculated from Every's closed form expressions using the best fit elastic constants. The large variation in the frequency shift as a function of crystallographic orientation suggests that ice III is, in fact, quite acoustically anisotropic. This is confirmed by the elastic constants determined in this study. The large number and high quality of experimental data points lead to an exceptionally good fit.

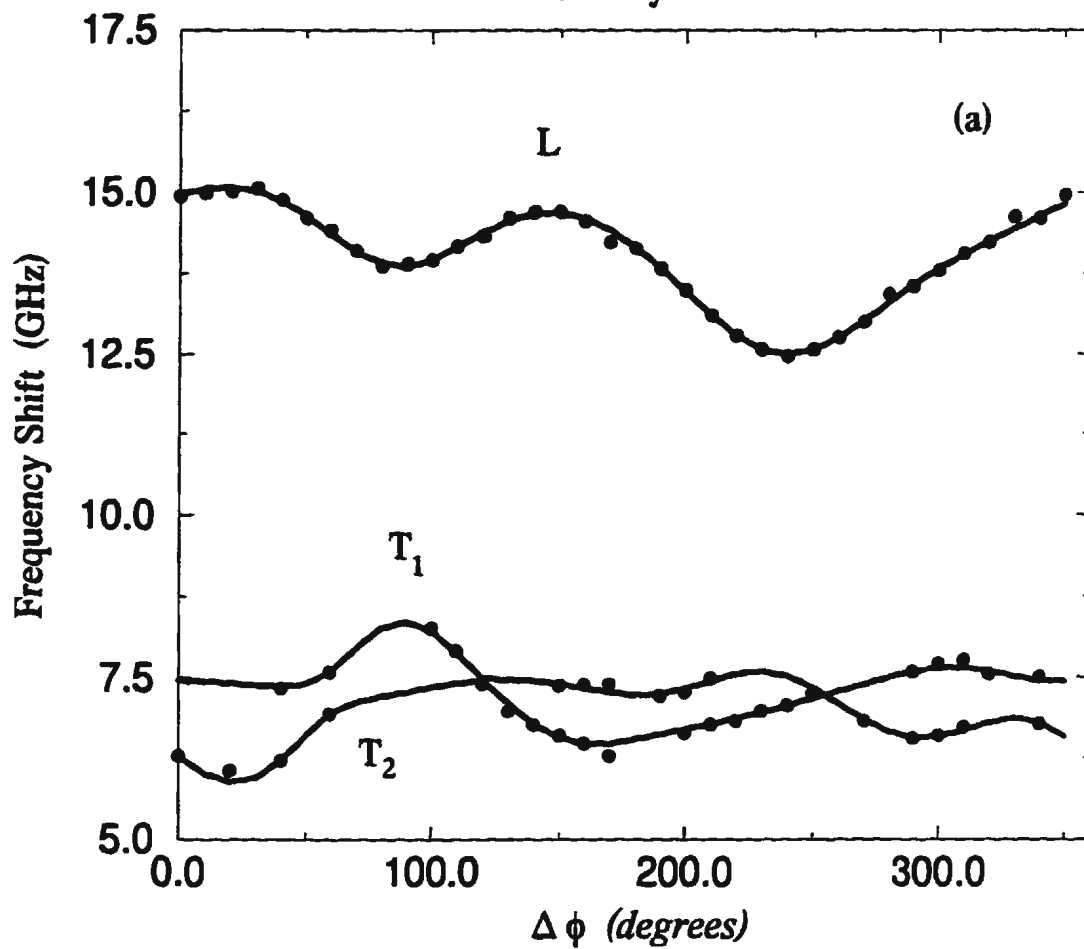
The experiment on crystal # 3 was conducted using a different Brillouin set-up. A Spectra Physics 2000 argon ion laser was used for these studies (see experimental set-up). The FSR of the Fabry-Perot interferometer was set to 39.19 Ghz, this allowed the collection of spectra without overlap of spectral components. Data were collected at various pressures ranging from 2.5 to 3.0 kbar.

### **Figure 3.6 Frequency Shift vs. $\Delta\phi$**

Frequency shift plotted as a function of the angle of rotation  $\Delta\phi$  about the laboratory z-axis. The solid circles represent the experimental data and the smooth curves are the frequency shifts calculated using the best fit elastic constants. (a) Ice III crystal #1, (b) Ice III crystal #2,  $T = -20^\circ\text{C}$  and  $P = 2.2$  kbars.

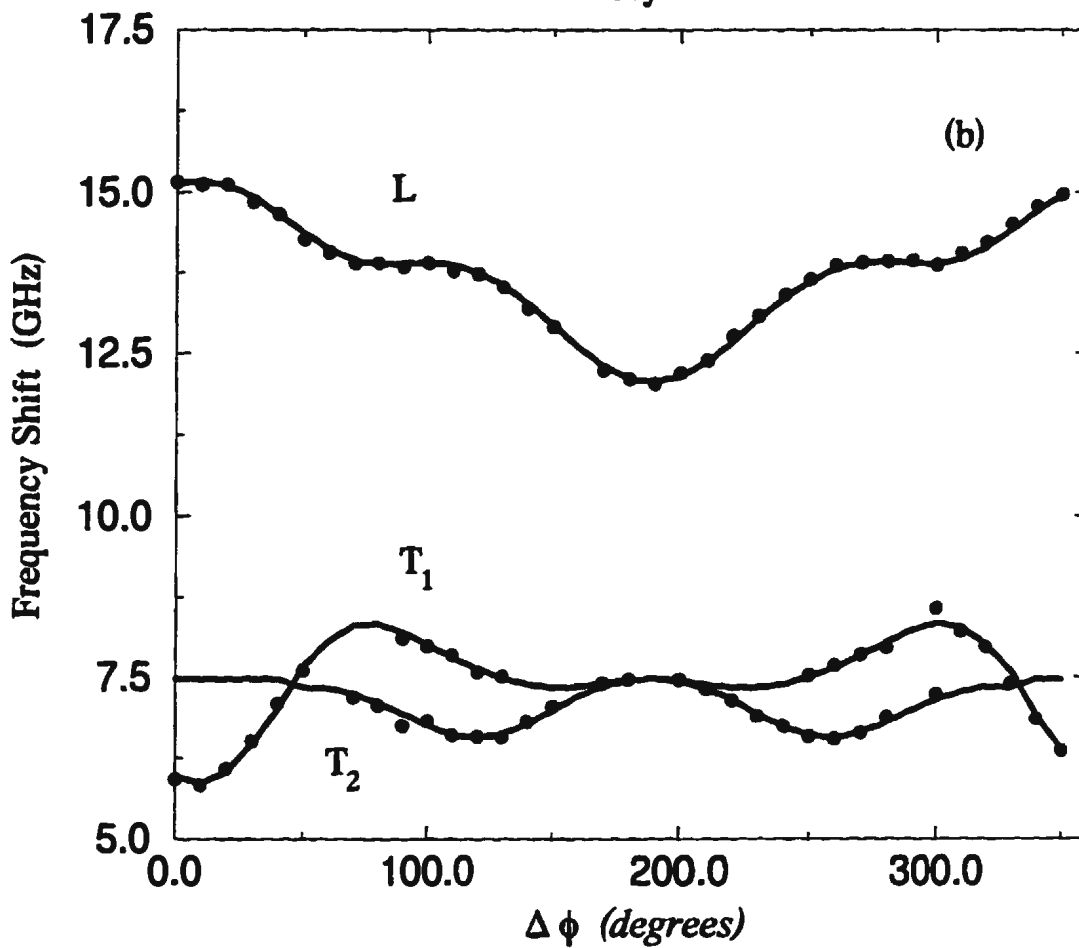
# Frequency Shift vs. $\Delta\phi$

Ice III Crystal # 1



# Frequency Shift vs. $\Delta\phi$

Ice III Crystal # 2



The variations in frequency shift with pressure are best seen by plotting the calculated frequency shift as a function of the sample orientation, see Fig. 3.7. The smooth curves indicate the frequency shift values calculated from the best fit elastic constants and numerical diagonalization of the Christoffel determinant. The fit to the experimental data was again excellent.

The best fit values for the 6 independent elastic constants found for crystal # 1 and #2 at  $P = 2.2$  kbar and  $T = -20^{\circ}\text{C}$  are given in Table 3.3. The agreement between the elastic constants calculated independently for each crystal is excellent. As well, the elastic constants found when all data were combined are presented with the calculated errors. The errors given in Table 3.3 represent a standard deviation in the least squares fit and are caused by uncertainties in the frequency shifts and crystallographic orientation and are calculated using all data combined, as discussed in Section 3.1.4. There are additional systematic errors caused by uncertainties in the refractive index, scattering angle and, to a much lesser extent, the error in the laser frequency. This combination of errors can be easily calculated from the Brillouin equation and is found to be approximately 1%.

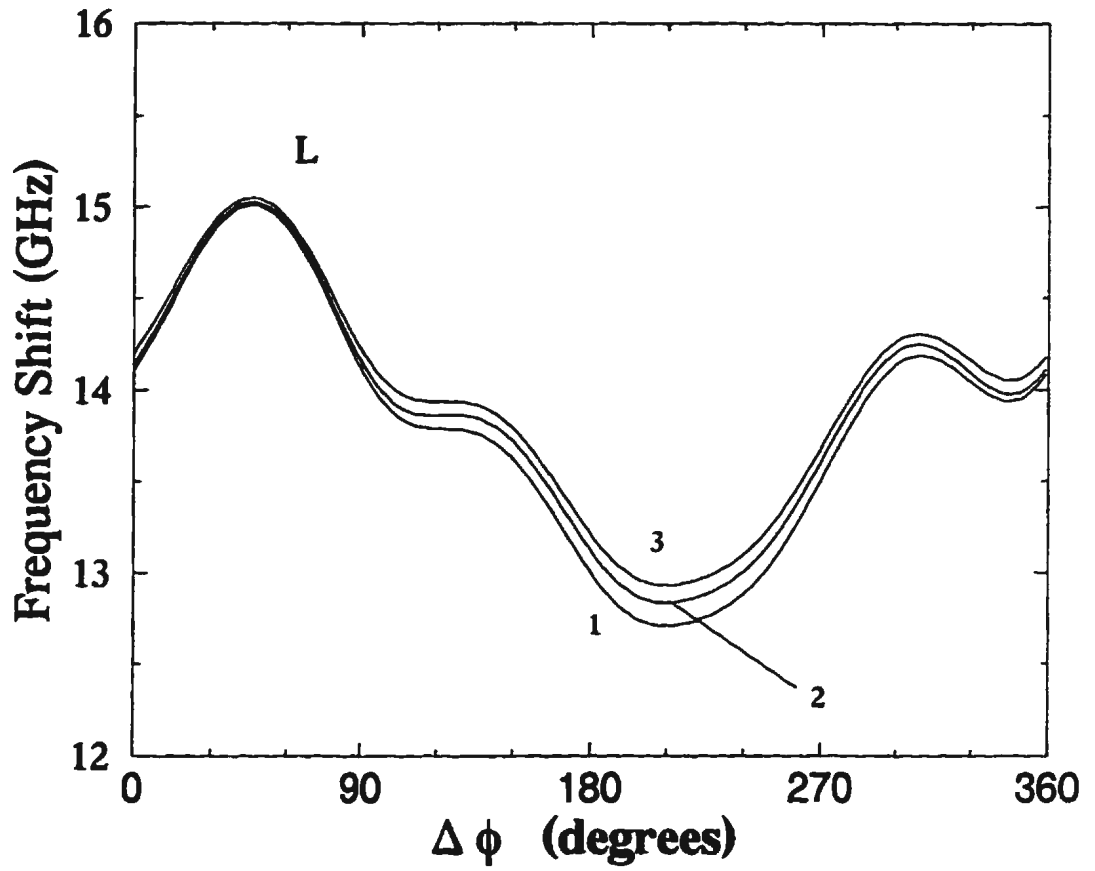
The elastic constants calculated using data from crystal # 3 at 2.5, 2.8, and 3.0 kbar are given in Table 3.4 along with the calculated density and refractive index. The elastic constants were then plotted as a function of pressure, see Fig. 3.8 and fitted to either a linear or a quadratic polynomial depending on the general shape of the plot. All but the

### **Figure 3.7 Frequency Shift Curves**

Frequency shift calculated from the best fit elastic constants at 1) 2.5 kbar, 2) 2.8 kbar, and 3) 3.0 kbar as a function of rotation angle  $\Delta\phi$ . The longitudinal shifts are shown in (a) and the two transverse shifts are shown in (b).

# Frequency Shift vs. $\Delta\phi$

P = 2.5, 2.8, 3.0 kbar



# Frequency Shift vs. $\Delta\phi$

P = 2.5, 2.8, 3.0 kbar

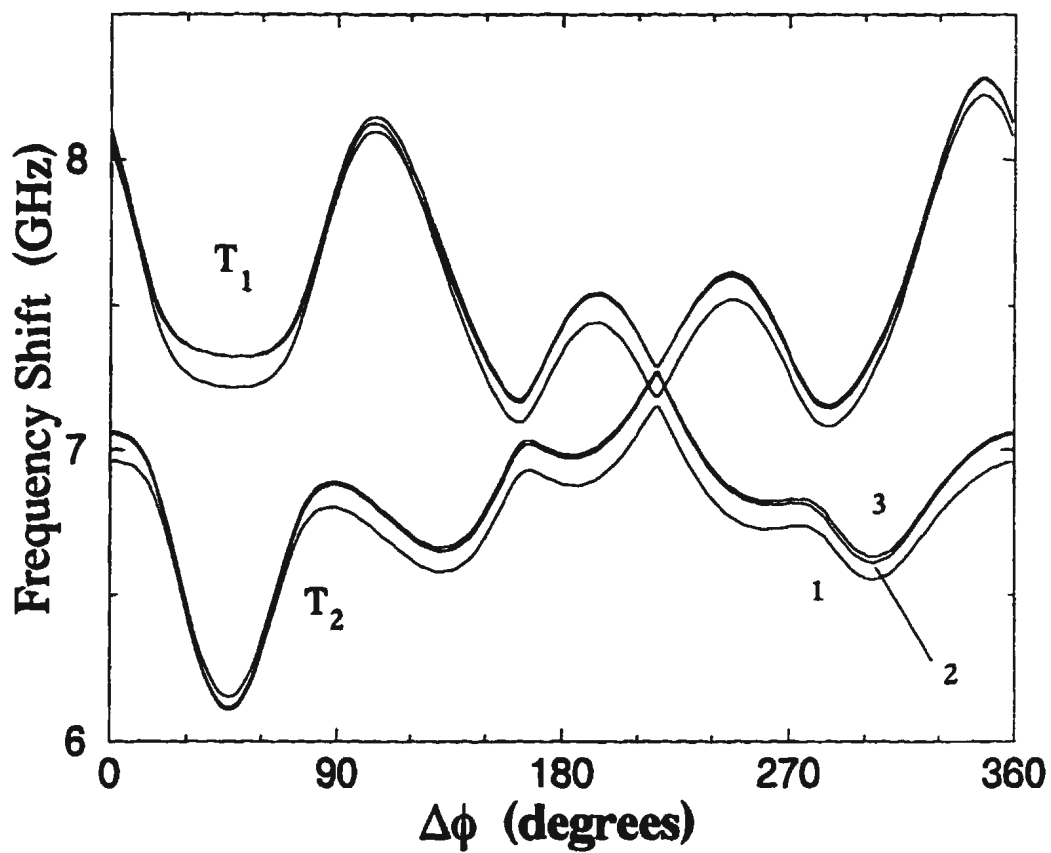


**Table 3.3**  
**Elastic Constants of Ice III**  
 Elastic constants are given in units of  
 $\times 10^4$  bar at  $P = 2.2$  kbar and  $T = -20$  °C.

	$\theta$	$\phi$	$\chi$	$C_{11}$	$C_{12}$	$C_{13}$	$C_{33}$	$C_{44}$	$C_{66}$
Ice III (a)	64.2	118.5	-19.2	15.34	9.97	6.45	11.50	4.46	5.67
Ice III (b)	136.2	-8.7	45.4	15.40	9.95	6.56	11.58	4.47	5.70
Ice III*				15.37 $\pm 0.5$	9.95 $\pm 0.6$	6.51 $\pm 0.6$	11.55 $\pm 0.7$	4.46 $\pm 0.2$	5.68 $\pm 0.4$
				$S_{11}$	$S_{12}$	$S_{13}$	$S_{33}$	$S_{44}$	$S_{66}$
Ice III**				12.00	-6.44	-3.13	12.19	22.42	17.61

\* All data combined and analysed together.

\*\* Elastic compliance constants (error approximately 2.5%).

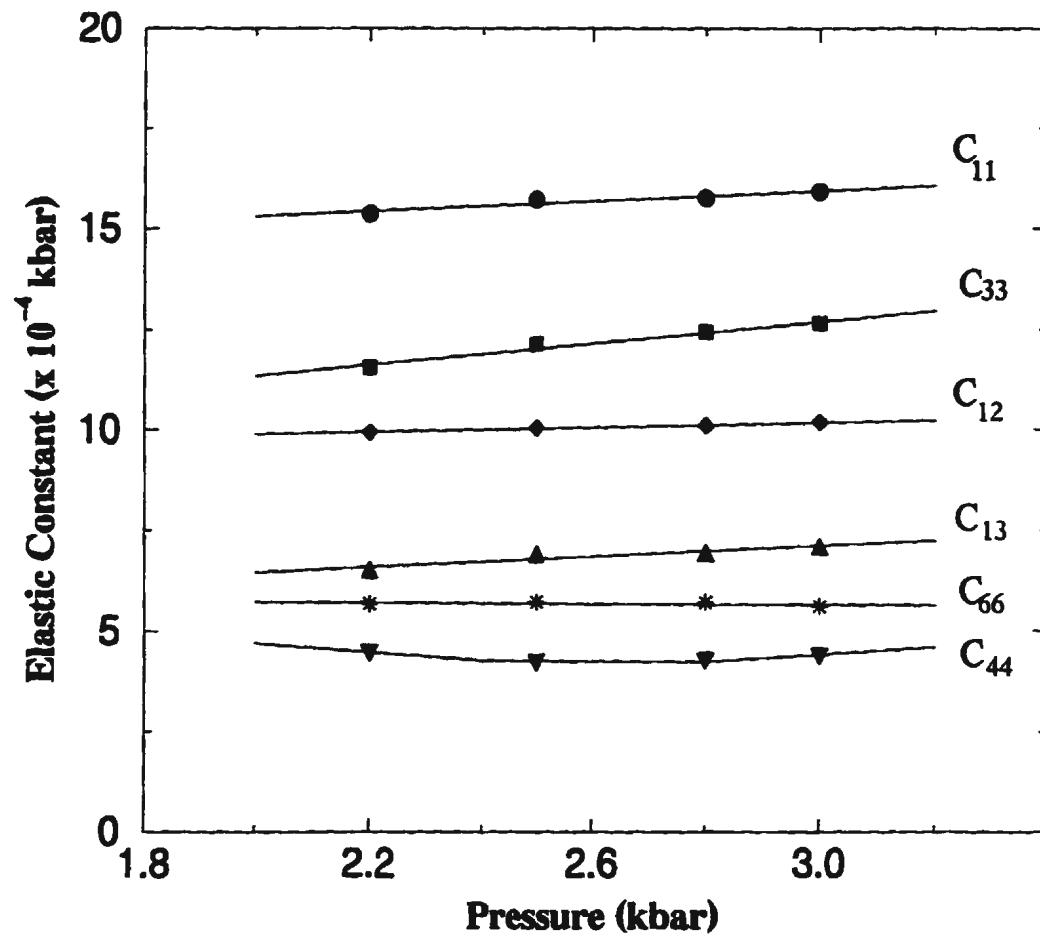
**Table 3.4**  
**The Elastic Constants, Density and**  
**Refractive Index of Ice III at Each Pressure Studied**

Pressure	$\rho$ (g/cm <sup>3</sup> )	n	C <sub>11</sub>	C <sub>12</sub>	C <sub>13</sub>	C <sub>33</sub>	C <sub>44</sub>	C <sub>66</sub>
2.2	1.1586	1.386	15.37	9.95	6.51	11.55	4.46	5.68
2.5	1.1622	1.388	15.73	10.06	6.91	12.15	4.23	5.72
2.8	1.1659	1.389	15.75	10.10	6.92	12.43	4.38	5.71
3.0	1.1683	1.390	15.92	10.19	7.09	12.65	4.39	5.62

**Figure 3.8 Elastic Constants of Ice III as a Function of Pressure**

Elastic constants of ice III as a function of pressure. The solid squares and circles are elastic constants obtained from the experimental frequency shift measurements and the smooth curves illustrate the best fit polynomials.

## Elastic Constants of Ice III



elastic constant  $C_{66}$  was found to have a positive slope. The functional dependence of the elastic constants with pressure is

$$C_{11}(P) = 0.6197 P_{\text{kbar}} + 14.07$$

$$C_{12}(P) = 0.2789 P_{\text{kbar}} + 9.34$$

$$C_{13}(P) = 0.6510 P_{\text{kbar}} + 5.15$$

$$C_{33}(P) = 1.3374 P_{\text{kbar}} + 8.68$$

$$C_{44}(P) = 1.26 P_{\text{kbar}}^2 - 6.63 P_{\text{kbar}} + 12.93$$

$$C_{66}(P) = - 0.0605 P_{\text{kbar}} + 5.84 . \quad 3.10$$

The units of the elastic constants in the above equations are,  $\times 10^4$  bar. The elastic constant  $C_{33}$  has the greatest slope while that for  $C_{66}$  is almost zero.

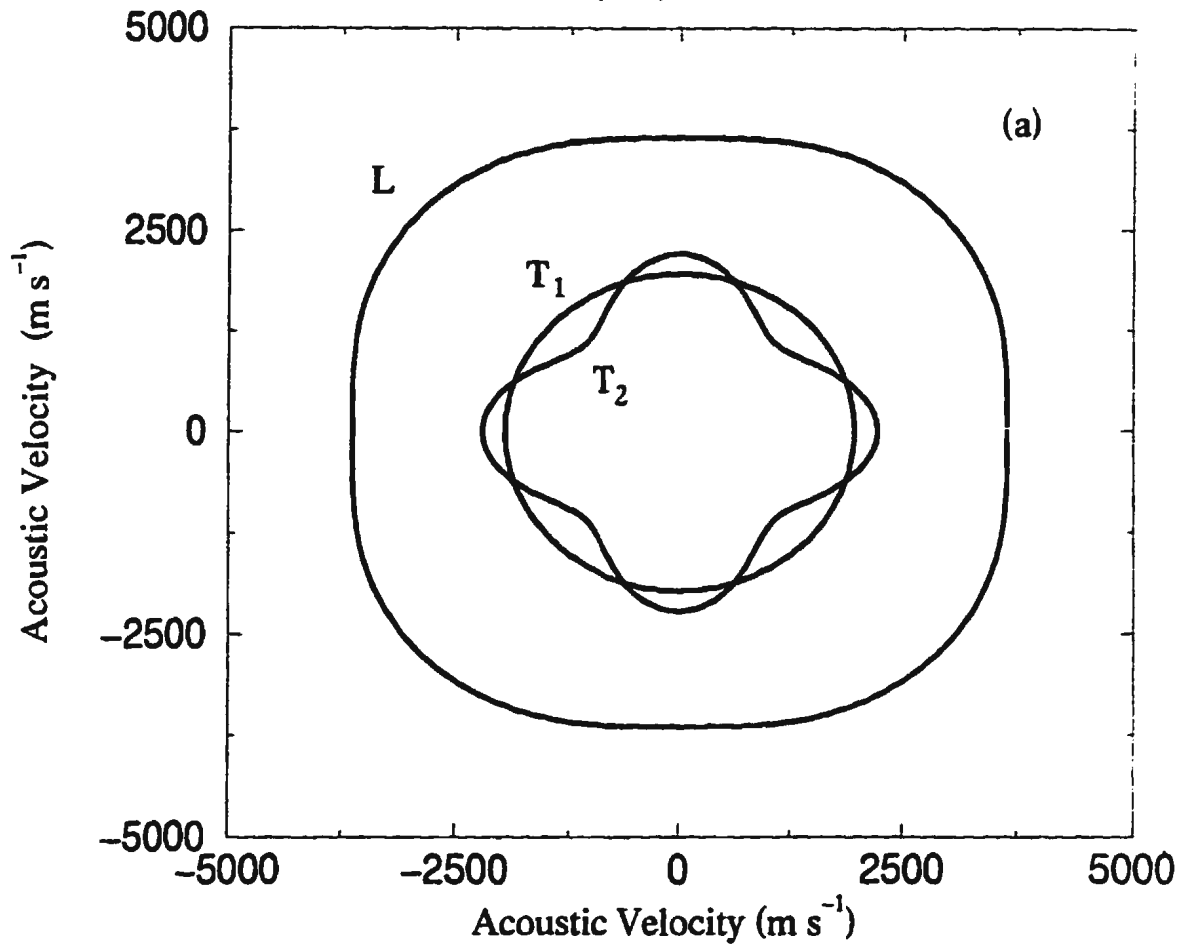
Acoustic velocities can be calculated for an arbitrary propagation direction once the elastic constants are known. Fig. 3.9 shows the acoustic symmetry of ice III by plotting the acoustic velocity, in polar coordinates, in several crystallographic planes. There is variation in the longitudinal acoustic velocity in the (001) and the (010) planes. In the (001) plane the velocity along the crystallographic [100] and [010] directions was found to be  $3574 \text{ m s}^{-1}$  and  $3674 \text{ m s}^{-1}$  respectively while the maximum velocity,  $3973 \text{ m s}^{-1}$ , is in the [110] direction. In the (010) plane the minimum velocity is  $3223 \text{ m s}^{-1}$  in the

**Figure 3.9 Acoustic Velocity in High Symmetry Planes of Ice III**

The calculated acoustic velocity of Ice III in high symmetry crystal planes. L, longitudinal acoustic velocity, and  $T_1$  and  $T_2$ , transverse acoustic velocities. (a) (001) plane, (b) (010) plane.

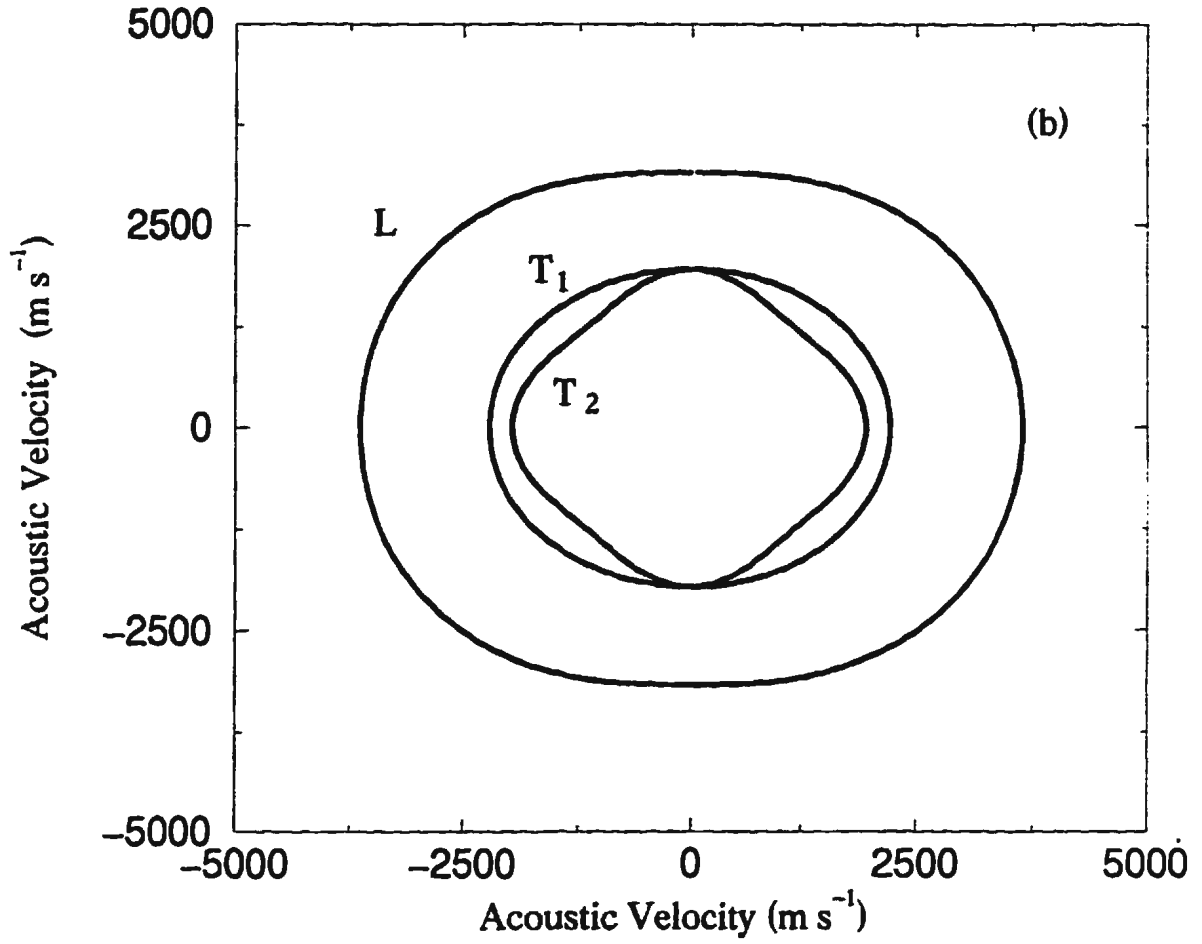
# Acoustic Velocity

(001) Plane



# Acoustic Velocity

(010) Plane



[001] direction and the maximum is  $3607 \text{ m s}^{-1}$  in the [101] direction. Due to anomalous velocity behaviour of two transverse polarizations in regions where they become nearly degenerate these calculations were done by diagonalizing the Christoffel matrix numerically rather than using the closed form expressions of Every.

### 3.3.2 Derived Polycrystalline Elastic Properties

Bulk elastic properties such as, the adiabatic bulk modulus  $B_s$ , Young's modulus  $E$ , the Lamé constants  $\mu$  and  $\lambda$ , Poisson's ratio  $\sigma$ , and the average longitudinal and transverse acoustic velocities  $\bar{V}_L$  and  $\bar{V}_T$  of polycrystalline solids may be derived from the single crystal elastic constants as described in section 3.4.1. These calculations were performed for samples of ice III and are given below. The bulk modulus was found by substituting the six independent, non-zero, elastic constants of ice III in equation 2.18. The resulting general equation becomes

$$B_s = \frac{C_{33}C_{11} - 2C_{13}^2 + C_{33}C_{12}}{C_{11} + 2C_{33} - 4C_{13} + C_{12}}, \quad 3.11$$

where the bulk modulus, as well as, the other polycrystalline elastic properties of ice III at 2.2 kbar and  $-20^\circ\text{C}$  are given in Table 3.5. The average acoustic velocity and bulk modulus measured directly from polycrystalline samples by Gagnon, *et al.*<sup>31</sup> were used to calculate the polycrystalline elastic properties under pressure and temperature conditions similar to those of present experiment. They are presented in Table 3.5 for

**Table 3.5**  
**Elastic Properties of Isotropic**  
**Polycrystalline Ice III**

	Ice III *	Ice III **
	P = 2.2 kbar T = -20° C	P = 2.76 kbar T = -27.2° C
$\bar{V}_L$ (m/s)	3658	3648
$\bar{V}_T$ (m/s)	2008	1882
$B_s$ (kbar)	92.7	99.4
$\mu$ (kbar)	46.7	41.0
$\lambda$ (kbar)	61.5	72.1
E (kbar)	120.0	108.1
$\sigma$	0.284	0.319

\* Present results.

\*\* Calculated from the results of R.E. Gagnon, *et al.*<sup>31</sup>

comparison. The polycrystalline elastic properties calculated from accurate values of the elastic constants found in this work and those measured from previous experiments are in good agreement.

The polycrystalline elastic properties were calculated at 2.2, 2.5, 2.8 and 3.9 kbar and have been fitted to linear equations. The variation of these quantities with pressure is given by the following equations.

bulk modulus:

$$B_s(P)_{\text{kbar}} = 8.127 P_{\text{kbar}} + 75.50 \quad 3.12$$

Young's modulus:

$$E(P)_{\text{kbar}} = -1.0 P_{\text{kbar}} + 121.6 \quad 3.13$$

average acoustic velocity:

$$\bar{V}_L(P)_{\text{m s}^{-1}} = 58.74 P_{\text{kbar}} + 3530.43 \quad 3.14$$

$$\bar{V}_T(P)_{\text{m s}^{-1}} = -34.22 P_{\text{kbar}} + 2075.6 \quad 3.15$$

Poisson's ratio:

$$\sigma(P) = 0.246 P_{\text{Kbar}} + 0.018 \quad 3.16$$

Lamé constants:

$$\mu(P)_{\text{Kbar}} = -1.0578 P_{\text{Kbar}} + 48.67 \quad 3.17$$

$$\lambda(P)_{\text{Kbar}} = 8.80 P_{\text{Kbar}} + 43.04 \quad 3.18$$

The units are given by subscripts in the above equations. The above experimental and derived data fully describe the elastic properties of ice III at  $T = -20^\circ\text{C}$  at pressures ranging from the ice Ih-ice III phase transition to the ice III-ice V phase transition. It is thought that under certain temperature conditions the high pressures created with a shock wave by explosive loading of ice Ih will result in ice III. If this is so, detailed understanding of the elastic properties of ice III as a function of pressure are essential to complete understanding of the mechanical processes involved. In chapter V the elastic properties of ice VI, which has the same tetragonal crystal symmetry but different point group (see Table 1.1) as ice III, will be discussed. The elastic constants of ice V are presented in the next chapter.

# **Chapter IV**

## **Single Crystal Growth and The Elastic Constants of Ice V**

### ***4.1 ICE V***

Samples of ice V were very easily produced. In the initial stages of this experiment tests were conducted to determine the best method by which single crystals of the high pressure phases of ice could be produced. During this process polycrystalline samples were initially frozen at pressures close to the phase boundary between ice III and ice V. The distinction between the two was made evident by the melting pressure at  $-17^{\circ}\text{C}$ . A variety of growth procedures were tested starting with polycrystalline samples of ice III and ice V, whichever happened to form in the high pressure chamber. In the present experiment, ice V was the first successfully grown large single crystal from which Brillouin spectra were observed, of any of the high pressure phases of ice. The crystal, however, was lost before sufficient Brillouin spectra could be collected. Fortunately, the first single crystal from which significant Brillouin data were collected was ice III. After that, three independent single crystals of ice V were produced by a method similar to that of ice III, Brillouin spectra were collected and the results are reported in this chapter. No pressure dependent studies of the elastic constants of ice V were performed.

#### ***4.1.1 Orientation Problems***

As mentioned in chapter I the crystal structure of ice V is monoclinic, which is the lowest symmetry of all known crystalline polymorphs of ice. Low crystallographic symmetry greatly complicates crystal orientation and analysis of Brillouin frequency shift data. Crystals with monoclinic symmetry, for example, are optically biaxial. This leads to an optical indicatrix which is described by a triaxial ellipsoid with two distinct optic axes which are defined by two sets of polar angles  $\theta_{1,2}$  and  $\phi_{1,2}$ . In contrast, tetragonal crystals, such as ice III and VI, have only one optic axis parallel to the crystallographic c-axis. It may be possible to partially orient biaxial crystals by an optical technique similar to that used for ice III and VI. The extinction points, given by the Biot-Fresnel law and the technique discussed in section 3.1.3, of a biaxial crystal are mathematically more difficult to describe and many suitable combinations of the polar angles  $\theta_{1,2}$  and  $\phi_{1,2}$  exist. Even if the optic axes and the axes of the triaxial ellipsoid are found and if one assumes that one of the crystallographic axes is perpendicular to the plane containing the two optic axes (the optic plane), it is not clear which crystallographic axes bisects the acute and obtuse angle formed by the optic axes. Hence there is additional uncertainty in the orientation of the optical indicatrix with respect to the crystallographic axes. The problem is further complicated because the required Euler angles relate the orthogonal laboratory system to the orthogonal coordinates in which the elastic constant tensor is defined, not the monoclinic crystallographic axis which is a set of oblique coordinates (recall  $\beta \sim 109^\circ$ , see Table 1.1).

Since it may be possible to determine one of the crystallographic axes using an optical technique, an attempt was made to partially orient the ice V samples. A set of extinction angle measurements were collected from each of the three crystals studied. After fitting the extinction angle data to the appropriate equation based on the Biot-Fresnel law and using the results to calculate the polar coordinates of the indicatrix it was found that none of these angles coincided with the polar angles of the crystallographic b-axis (given by the Euler angles fitted to the acoustic data). As mentioned above, there are many combinations which give adequate fits to extinction angle data for biaxial crystals and the angles found in the above analysis were not correct. It is thought that a method may be developed to at least partially orient biaxial crystals optically using a technique similar to that used for ice III and ice VI. Experiments would have to be conducted on samples of known orientation in a specially designed containment cell to perfect such a technique.

All these optical orientation problems can be avoided if the Euler angles are found along with the elastic constants when fitting the parameters of the Christoffel determinant, Eq. 2.16, to the experimental Brillouin frequency shifts. It is therefore, unnecessary to have *a priori* knowledge of the Euler angles. In the present study the elastic constant tensor is defined with respect to a coordinate system given by unit vectors  $X_1$ ,  $X_2$ ,  $X_3$  whose  $X_2$  axis is parallel to the crystallographic b-axis.

The monoclinic space group of ice V is denoted as A2/a which has 13 independent elastic constants. Because there exist no closed form solutions of the Christoffel determinant, Eq. 2.16, the eigenvalues  $\rho V^2$  were determined numerically. A separate computer minimization program was written using the NAG math libraries which fitted the elastic constants and Euler angles to the experimental data by minimizing  $\chi^2$  (Eq. 3.7). The computer routine was tested using two methods. (1) Previously determined elastic constants of the monoclinic crystal<sup>117,118</sup>  $C_{14}H_{14}$  were used with arbitrarily chosen Euler angles  $\theta$ ,  $\phi$  and  $\chi$  to calculate frequency shift data in  $\Delta\phi$  increments of  $10^\circ$ . The calculated points served as experimental Brillouin data. The non-linear least squares computer minimization routine was used to fit the elastic constants to the simulated Brillouin data. The elastic constants were very accurately reproduced. (2) The program was modified to fit the elastic constants of the tetragonal structure by redefining the relationships between the elastic constants in the Christoffel determinant. The program was run on the ice VI data and the elastic constant results of chapter V were accurately reproduced. As with the other phases, the elastic properties of polycrystalline ice V have been determined by the manner described in Section 2.1.4.

#### ***4.1.2 Density and Refractive Index***

The density and refractive index of ice V were calculated using previously determined results in a manner similar to that of ice III and ice V. Gagnon *et al.*<sup>31</sup> experimentally

determined a quadratic equation giving the pressure dependence of the density. The equation is given as,

$$\rho_{iceV}(P)_{g\ cm^{-3}} = 1.1974 + 1.9632 \times 10^{-2} P_{kbar} - 1.0982 \times 10^{-3} P_{kbar}^2, \quad 4.1$$

where the units of the above equation are indicated by the subscripts. The data used to obtain the above equation were collected at  $-35^{\circ}\text{C}$ , between 3 kbar and 6 kbar. The density at 3.0 kbar is calculated to be  $1.2572\ g\ cm^{-3}$ .

The refractive index as a function of density was calculated, using the Eulerian strain, following the method of Polian and Grimsditch<sup>76</sup> see Section 3.1.1. The results calculated from these equations are assumed accurate for ice V and the refractive index at 3.0 kbar was calculated to be 1.4181.

## ***4.2 CRYSTAL GROWTH AND RESULTS***

Ice V shares a common phase boundary with liquid water and therefore the method of crystal growth closely followed that described for ice III and ice VI.

### ***4.2.1 Growth of Ice V single Crystals***

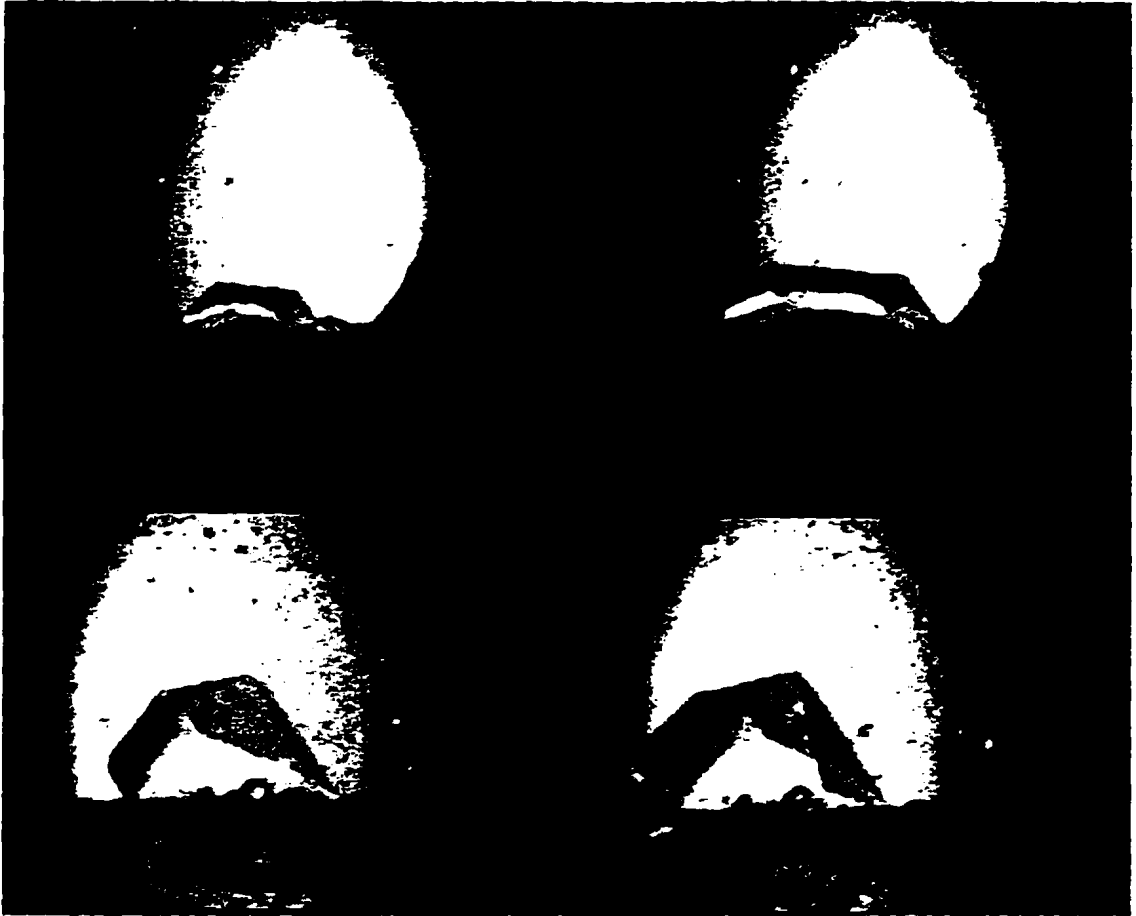
Triply distilled deionized water produced at NRC/IMD was boiled for approximately 20 minutes to drive out any dissolved gasses. The water was placed in the glass cell and

pressure chamber and pressurized to approximately 4.4 kbar. The temperature was then reduced to  $-35^{\circ}\text{C}$  and the liquid sample left in a supercooled state for several hours. Upon nucleation the sample froze directly into ice V. The longitudinal Brillouin frequency shift of ice V is approximately 2.5 GHz greater than the longitudinal Brillouin frequency shift of ice III.<sup>31</sup> This was used as a definitive test to confirm that ice V had been produced. After raising the temperature to approximately  $-17^{\circ}\text{C}$  the sample was slowly melted by slightly decreasing the pressure to  $\sim 2.8$  kbar. Again the sample was constantly monitored during the melting process with the aid of a microscope and video equipment. It was noticed that ice V generally melted much faster than ice III. In fact, the entire sample was melted to a tiny seed ( $\sim 50\ \mu\text{m}$ ) within 45 minutes from the initial depressurization. The pressure was then slightly increased until the sample slowly began to refreeze. As before, the pressure and temperature were constantly monitored and adjusted to maintain optimum crystal growth. Once the sample had fully grown it was viewed between crossed polaroid filters to check for grain boundaries and to determine if a single crystal had been successfully grown. If necessary the procedure was repeated.

Fig. 4.1 illustrates four video frames showing the growth of two single crystal seeds of ice V. The top two video frames show the growth of one crystal, the time between images is approximately 30 sec. The two images on the bottom of Fig. 4.1 show another crystal which nicely illustrates the complex crystal morphology of ice V. The bright region is caused by light refracting through the cylindrical sample cell and is approximately 1 mm in diameter. The entire growth process typically took 5-6 hours. Once a sample had

### **Figure 4.1 Growth of a Single Crystal of Ice V**

Several video images illustrating the growth of a single crystal of ice V. The top two images show the growth of one crystal. Again, the brightest portion of the frame is due to the lensing effect produced by the cylindrical sample containment cell, the width is ~ 1mm. The time between the two consecutive frames is ~ 30 sec. The lower two images were taken from a separate crystal and illustrate the complex morphology of monoclinic ice V crystal symmetry.



completely frozen the temperature was decreased to  $-20^{\circ}\text{C}$ , the pressure set to 3.0 kbar and the sample left overnight to fully anneal. The sample was again viewed between crossed polaroids to check for grain boundaries. Birefringent orientation data were collected from each of the three crystals but, as described earlier, were not used in the final analysis and are therefore reported in Appendix A. However, it is worth noting that the extinction points for ice V were sharp and found to be very well defined, in contrast to ice VI.

Preliminary Brillouin spectra were collected from the first two crystals at  $-20^{\circ}\text{C}$  in several crystallographic orientations. In an attempt to induce an ice V  $\rightarrow$  ice II phase transition the temperature of the sample was reduced to approximately  $-40^{\circ}\text{C}$ . Brillouin spectra were again taken and compared with the previously obtained spectra at the same orientation. A phase transition would be indicated by a change in the Brillouin frequency shift. After several days of observation no such phase transition occurred, perhaps because a single crystal of ice V lacks the necessary nucleation site required to initiate such a phase transition. Similar behaviour regarding ice III has been described in section 3.2. The temperature was then increased to approximately  $-35^{\circ}\text{C}$  and a complete set of Brillouin data collected. In the case of the third crystal, a complete set of Brillouin data was collected at  $-35^{\circ}\text{C}$  before the temperature was lowered to  $-40^{\circ}\text{C}$  and several more Brillouin spectra collected. Again, after comparing the two sets of experimental data no phase transition was observed.

### ***4.2.2 Frequency Shift Data and the Elastic Constants of Ice V***

In these experiments the Spectra Physics Series 2000 argon ion laser provided monochromatic laser light at 514.5 nm at about 40 mW. The FSR of the Fabry-Perot was set to 39.19 GHz, this allowed the collection of data without overlap of spectral components. Fig. 4.2 illustrates a typical Brillouin spectrum of ice V collected at -35 °C and 3.0 kbar. Two transverse components and one longitudinal component are symmetrically spaced about the unshifted central peak and are indicated by T<sub>1</sub>, T<sub>2</sub>, L and U respectively. Brillouin spectra were collected in  $\Delta\phi$  increments of 10° or 20° through a complete 360° rotation about the laboratory z-axis. Collection times typically ranged from 6 to 8 hours. This resulted in a total of 201 frequency shift measurements being collected from the three single crystals at P=3.0 kbar and T=-35°C. The measured frequency shifts and the  $\Delta\phi$  increments are given in Table 4.1.

The monoclinic structure is distinguished from the tetragonal structure by two principal differences, (1)  $a \neq b$  and (2)  $\beta \neq 90^\circ$ , resulting in the number of independent elastic constants increasing from 6, or 7, depending on the point group, to 13. In the case of ice V,  $a = 9.22 \text{ \AA}$ ,  $b = 7.54 \text{ \AA}$  and  $\beta = 109.2^\circ$ . The large number of independent elastic constant and Euler angle parameters greatly increased the difficulty in finding the absolute minimum of  $\chi^2$ , see equation 3.7. It was thought that the elastic constants could be more easily found if data from all three crystals were combined and parameters fitted to all experimental data at once. The first approximation of the elastic constants was found by treating ice V as if it were tetragonal and finding the elastic constants  $C_{11}$ ,  $C_{12}$ ,  $C_{13}$ ,  $C$

### **Figure 4.2 Brillouin Spectrum of Ice V**

**Brillouin spectrum of ice V crystal #3 at  $\Delta\phi = 160^\circ$ ,  $T = -35^\circ\text{C}$ ,  $P = 3.0$  Kbar, the FSR is 39.19 GHz. Longitudinal, transverse, and unshifted Central peaks are indicated by L,  $T_{1,2}$  and U respectively. Two complete orders of the Fabry-Perot are shown and lines indicated by  $T_1$  and  $T_2$  correspond to the central unshifted peak.**

# Brillouin Spectrum

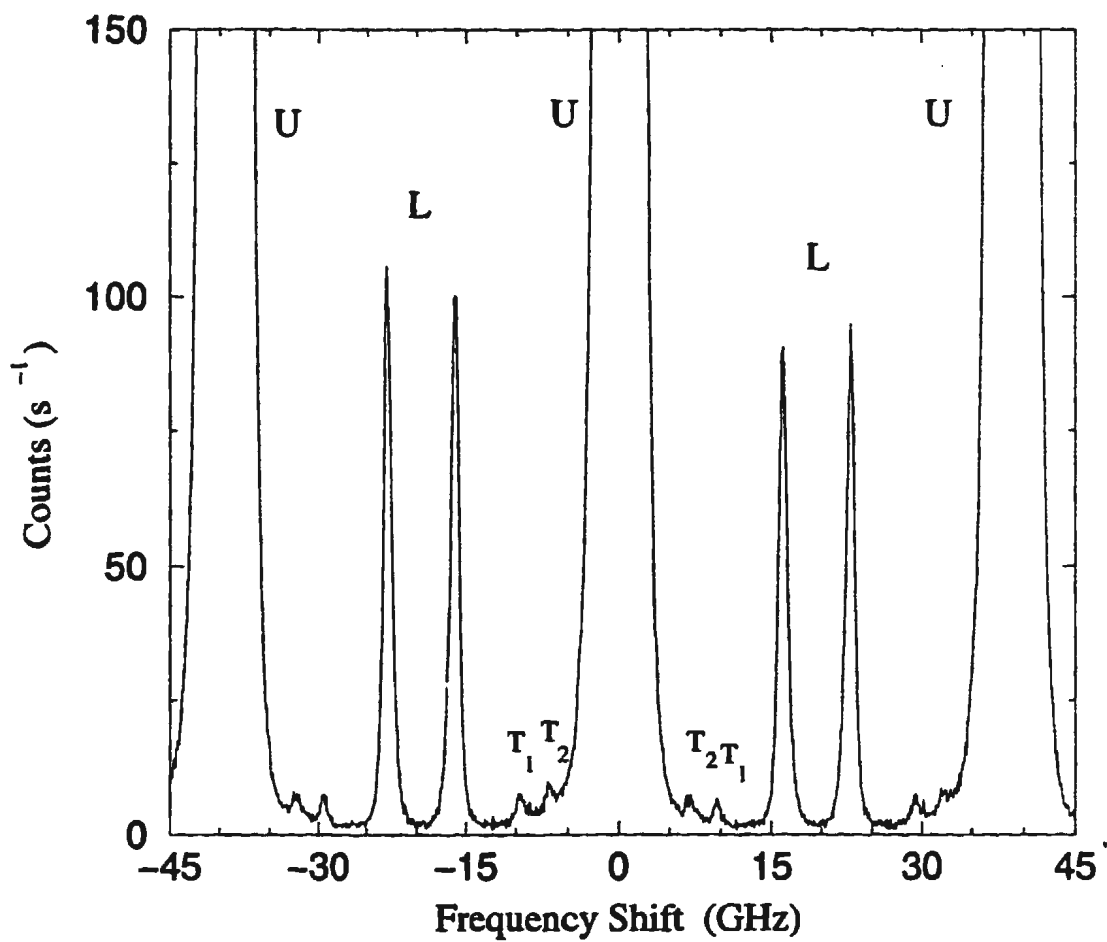


**Table 4.1 (a)**

**Brillouin Frequency Shifts (GHz) Ice V  
Crystal #1 ( $\theta=18.0$ ,  $\chi=21.3$ ,  $\phi=182.1$ )**

	$\Delta\phi$ (degrees)	$L$	$T_1$	$T_2$
1	0	16.17	8.06	7.57
2	10	15.77	-	7.86
3	20	15.41	8.22	-
4	30	15.27	8.18	-
5	40	15.18	8.14	-
6	50	15.13	-	8.14
7	60	15.21	-	7.88
8	70	15.43	-	-
9	80	15.57	-	-
10	90	15.72	9.27	-
11	100	15.82	-	7.83
12	110	15.59	9.80	-
13	130	15.87	-	-
14	140	16.01	10.20	-
15	150	16.26	9.67	7.69
16	160	16.61	8.87	7.84
17	170	16.86	8.64	7.68
18	180	17.33	-	7.04
19	190	17.51	-	6.56
20	200	17.56	-	-
21	210	17.45	-	6.59
22	220	17.27	-	7.38
23	230	16.97	8.11	-
24	240	16.28	9.35	-
25	250	15.80	9.95	-
26	260	15.31	-	-
27	270	15.26	10.81	-
28	280	15.76	10.19	8.33
29	290	16.13	9.77	7.98
30	300	16.50	9.20	7.49
31	310	16.68	9.01	7.39
32	320	16.84	8.57	6.98
33	330	16.85	-	-

34	340	16.70	7.78	-
35	350	16.48	7.61	-

**Table 4.1 (b)**

**Brillouin Frequency Shifts (GHz) Ice V  
Crystal #2 ( $\theta=101.2$ ,  $\chi=245.5$ ,  $\phi=83.2$ )**

	$\Delta\phi$ (degrees)	$L$	$T_1$	$T_2$
1	0	17.20	8.40	6.93
2	10	17.29	8.65	-
3	20	17.22	-	6.69
4	30	17.20	-	-
5	40	16.93	7.61	-
6	50	16.52	7.85	-
7	100	15.38	7.87	-
8	110	15.31	8.01	-
9	120	15.44	8.02	-
10	130	15.55	7.85	-
11	140	15.84	8.43	7.34
12	150	15.98	8.65	7.06
13	160	16.29	8.88	6.82
14	170	16.36	8.77	-
15	180	16.63	8.60	7.01
16	190	16.70	8.65	7.15
17	200	16.98	8.38	7.01
18	240	17.12	8.50	7.23
19	260	16.35	9.39	7.86
20	280	16.03	9.92	7.94
21	300	15.49	-	8.02
22	320	15.99	9.86	-
23	340	16.74	-	8.15

**Table 4.1 (c)**

**Brillouin Frequency Shifts (GHz) Ice V  
Crystal #3 ( $\theta=54.1$ ,  $\chi=42.9$ ,  $\phi=83.4$ )**

	$\Delta\phi$ (degrees)	$L$	$T_1$	$T_2$
1	30	16.04	9.69	-
2	40	16.16	9.88	6.71
3	60	16.35	9.45	7.09
4	70	16.75	8.80	6.81
5	80	16.94	8.27	7.13
6	90	17.12	7.93	7.10
7	100	17.14	8.03	7.20
8	110	16.91	8.44	7.07
9	120	16.67	9.09	7.06
10	140	16.00	9.79	6.80
11	150	16.05	9.98	7.03
12	160	16.25	9.51	6.79
13	190	16.83	7.89	-
14	200	16.77	7.65	-
15	210	16.55	8.30	-
16	220	16.41	8.85	-
17	230	16.10	9.33	-
18	240	16.02	9.62	6.85
19	250	15.90	9.34	6.80
20	260	15.96	9.19	6.84
21	270	16.07	8.55	7.30
22	280	16.07	-	7.87
23	290	16.03	8.18	-
24	300	15.96	8.72	7.28
25	310	15.95	9.08	-
26	320	15.95	-	-
27	330	16.04	8.88	6.90
28	340	16.23	8.48	7.47

$C_{22}$ ,  $C_{33}$  and  $C_{66}$  which best represent the ice V data. The initial values supplied to the curve fitting program were the elastic constants of ice VI. Subsequently each independent elastic constant of the monoclinic symmetry not present in the tetragonal symmetry was introduced and the data fitted again using the previously found elastic constants as initial parameters.

After completing this procedure the calculated curves were plotted and compared with the experimental points. In the case of the first two crystals there was generally good agreement between calculated and experimental points. The agreement between the calculated and experimental frequency shifts for the third crystal was, however, poor with some points differing by more than 1.5 GHz. Brief inspection of the experimental results of the third crystal indicate that the curves defined by the transverse modes are significantly different from that of crystal #1 and crystal #2. Therefore, it was incorrectly concluded that crystal #3 was anomalous and the data temporarily ignored. Emphasis was placed on finding elastic constant values which reproduce the data collected from crystal #1 and #2. In general, good agreement was achieved and none of the elastic constant values were able to accurately reproduce the data obtained from crystal # 3.

The above procedure was run again using the elastic constants of ice III as the initial parameters. This resulted in equally good fits to the data from crystal #1 and crystal #2, however, the procedure resulted in significantly different elastic constant values than those previously obtained. It was quickly realized that several different combinations of elastic

constants accurately reproduce the data collected from crystal #1 and #2. Calculations of the bulk modulus, by the method outlined in chapter II, and comparison with previously determined values proved useful in identifying elastic constants which were incorrect. Some values of the bulk modulus, however, fell within 15% of the previously determined values. Considering other measurements obtained from polycrystalline samples, 15% was considered to be within acceptable error.

Crystal #3 was consequently reexamined, the data were deemed reliable and the crystal was unquestionably ice V. The orientation must have been significantly different from the other two crystals. Therefore the correct elastic constant values must produce good fits to crystal #3 as well as crystal #1 and #2. Crystal #3 was therefore analyzed independently. The elastic constants of ice III were used as initial parameters in the curve fitting procedure. An extremely good fit to experimental data was obtained, see Fig. 4.3 (c). The average percent difference between calculated frequency shift values and the experimentally determined frequency shift values was less than 0.05%.

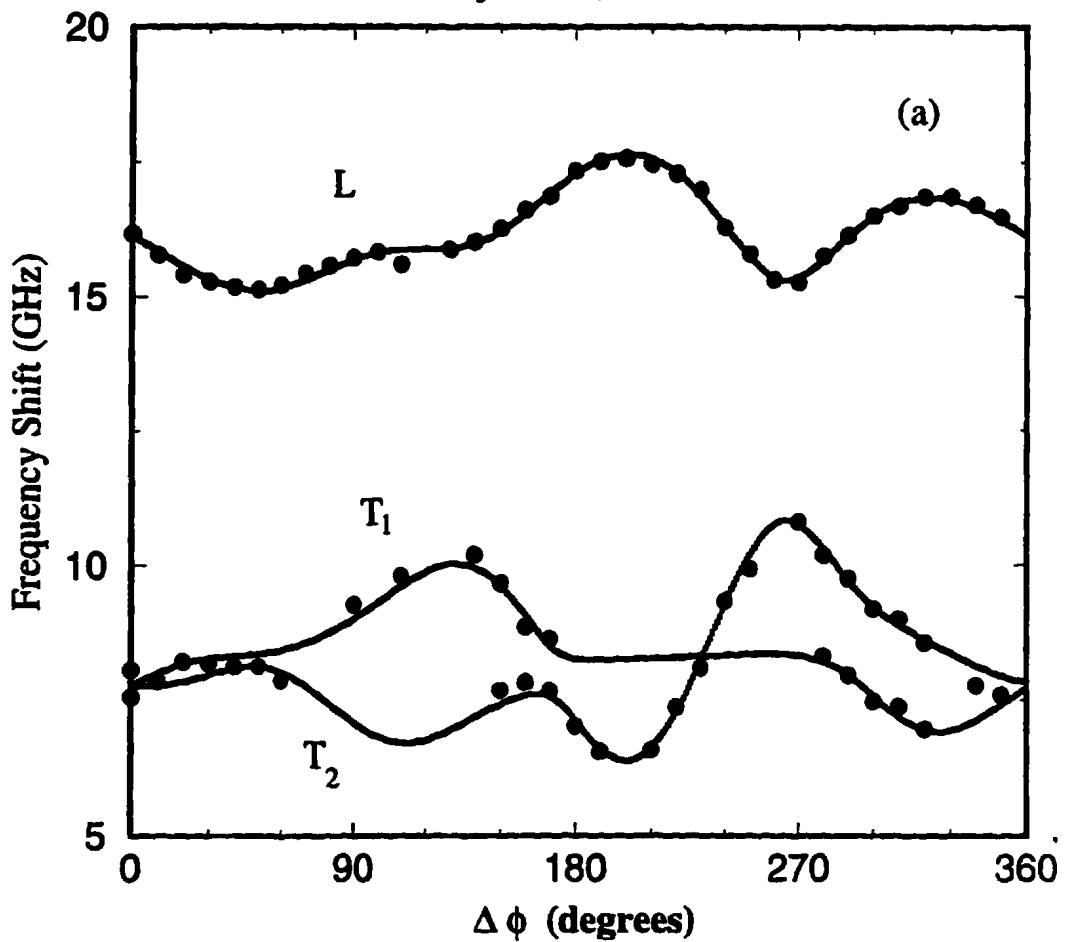
These values of the elastic constants were then fixed in an attempt to reproduce the experimental data of crystal #1 and crystal #2 by fitting only the corresponding Euler angles  $\theta$ ,  $\phi$  and  $\chi$ . The resulting fits were good indicating that the elastic constant parameters found from crystal #3 were very close to the best fit values for crystals #1 and #2. The Euler angles were then fixed and the best fit elastic constants for crystal #1 and crystal #2 determined. These data are plotted on Fig. 4.3 (a), (b) and (c) for crystals #1,

### **Figure 4.3 Frequency Shift versus $\Delta\phi$**

**The Brillouin frequency shift data, solid circles, and calculated best fit curves, smooth lines, (a) crystal #1, (b) crystal #2, (c) crystal #3. All data were collected at  $-35^{\circ}\text{C}$  and 3.0 kbar.**

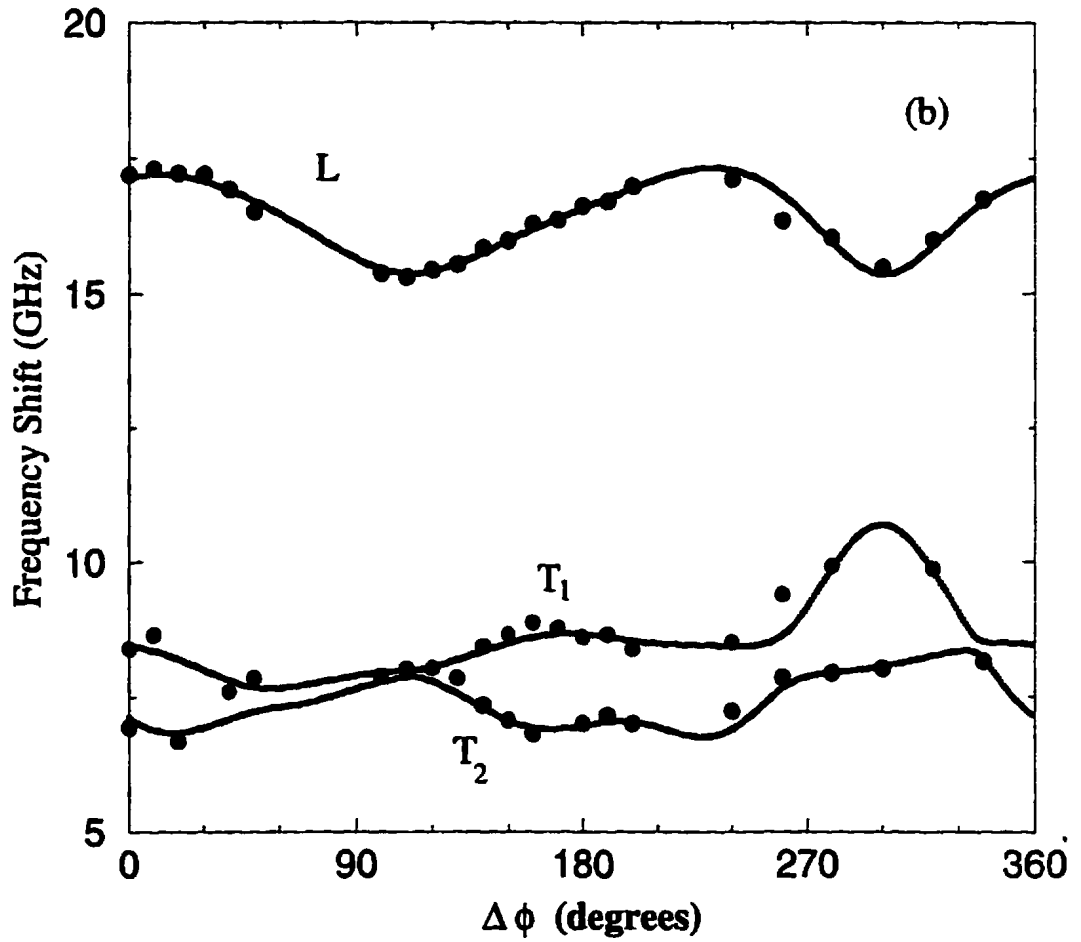
# Frequency Shift vs. $\Delta\phi$

Ice V, crystal #1, P = 3.0 kbar



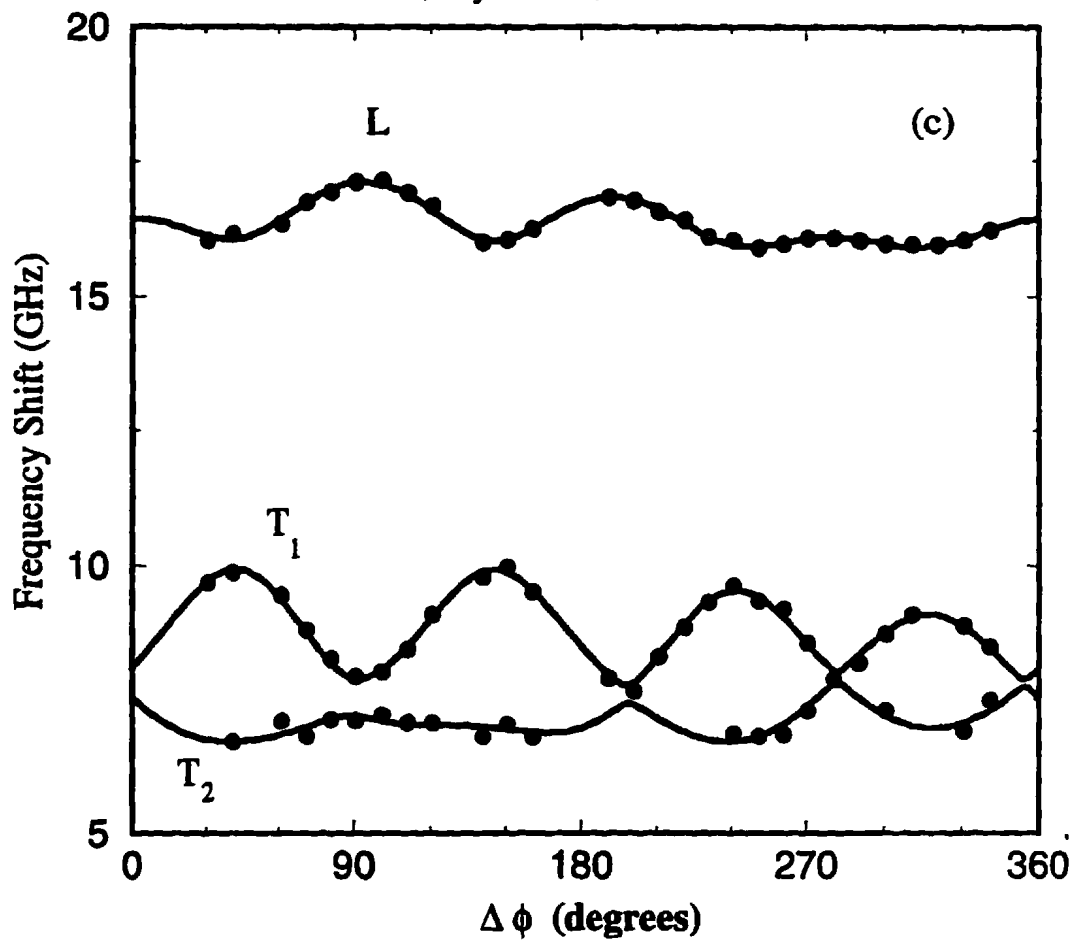
# Frequency Shift vs. $\Delta \phi$

Ice V, crystal #2, P = 3.0 kbar



# Frequency Shift vs. $\Delta \phi$

*Ice V, crystal #3, P = 3.0 kbar*



#2, and #3, respectively. The solid circles and the smooth curves represent the experimental and calculated frequency shifts, respectively. While the fit to the individual crystals is quite good, there is some variation between the independent systems. This is thought to be a result of the number of parameters being fitted and sensitivity of the elastic constant parameters to subtle differences in the experimental data. Finally all the data were recombined into one data file and the fitting program run to obtain the elastic constants of ice V. The values of the best fit elastic constants for each of the crystals, the results obtained when all data were combined and the best fit Euler angles are presented in Table 4.2. The errors quoted in Table 4.2 are non-systematic errors, the additional systematic error is ~ 1%, as discussed in Section 3.1.4. The errors of each individual crystal were, consequently, combined to obtain the errors given for ice V. The bulk modulus calculated using elastic constant data presented in Table 4.2 differ from the value of Gagnon *et al.*<sup>31</sup> by only 4.2 %, therefore the criteria that the bulk modulus fall within 15 % of values obtained by measurements from polycrystalline samples is fulfilled. This will be discussed along with other polycrystalline results in the next section.

The acoustic velocities in several high symmetry crystallographic planes were calculated from the ice V elastic constants. The velocities are plotted in polar coordinates in Fig. 4.4. As expected, ice V shows greater acoustic anisotropy than the other phases investigated in the present set of experiments. The maximum velocity in the (010) plane, Fig. 4.4 (a), is 4144 m s<sup>-1</sup> in the [100] and [001] directions, the minimum velocity is 3894 m s<sup>-1</sup> in

**Table 4.2**

**Elastic Constants ( $\times 10^4$  bar) and Euler Angles (degrees) of Ice V**

	<b>Crystal #1</b>	<b>Crystal #2</b>	<b>Crystal #3</b>	<b>Ice V</b>		<b>Ice V</b>
$C_{11}$	21.1	22.6	21.4	$21.4 \pm 1.2$	$S_{11}$	7.4
$C_{22}$	19.3	19.7	20.4	$19.3 \pm 1.2$	$S_{22}$	10.1
$C_{33}$	21.2	20.4	21.3	$21.1 \pm 1.3$	$S_{33}$	7.4
$C_{44}$	7.3	8.2	7.4	$7.5 \pm 0.7$	$S_{44}$	14.5
$C_{55}$	3.7	3.2	3.7	$3.7 \pm 0.5$	$S_{55}$	27.1
$C_{66}$	7.9	6.4	7.5	$7.5 \pm 0.7$	$S_{66}$	14.7
$C_{12}$	12.2	12.9	12.5	$12.2 \pm 1.2$	$S_{12}$	-4.1
$C_{13}$	9.5	9.5	9.1	$9.5 \pm 1.1$	$S_{13}$	-1.1
$C_{15}$	-0.1	0.1	0.1	$0.17 \pm 0.4$	$S_{15}$	-0.5
$C_{23}$	11.9	10.0	11.8	$11.8 \pm 1.1$	$S_{23}$	-3.8
$C_{25}$	-0.4	-0.2	0.0	$-0.1 \pm 0.8$	$S_{25}$	0.02
$C_{35}$	-0.1	-0.6	-0.4	$-0.3 \pm 0.6$	$S_{35}$	6.2
$C_{46}$	-2.1	-1.9	-2.1	$-2.1 \pm 0.3$	$S_{46}$	40.5
$\theta$	18.0	101.2	54.1			
$\phi$	182.1	83.2	83.4			
$\chi$	21.29	245.5	42.9			

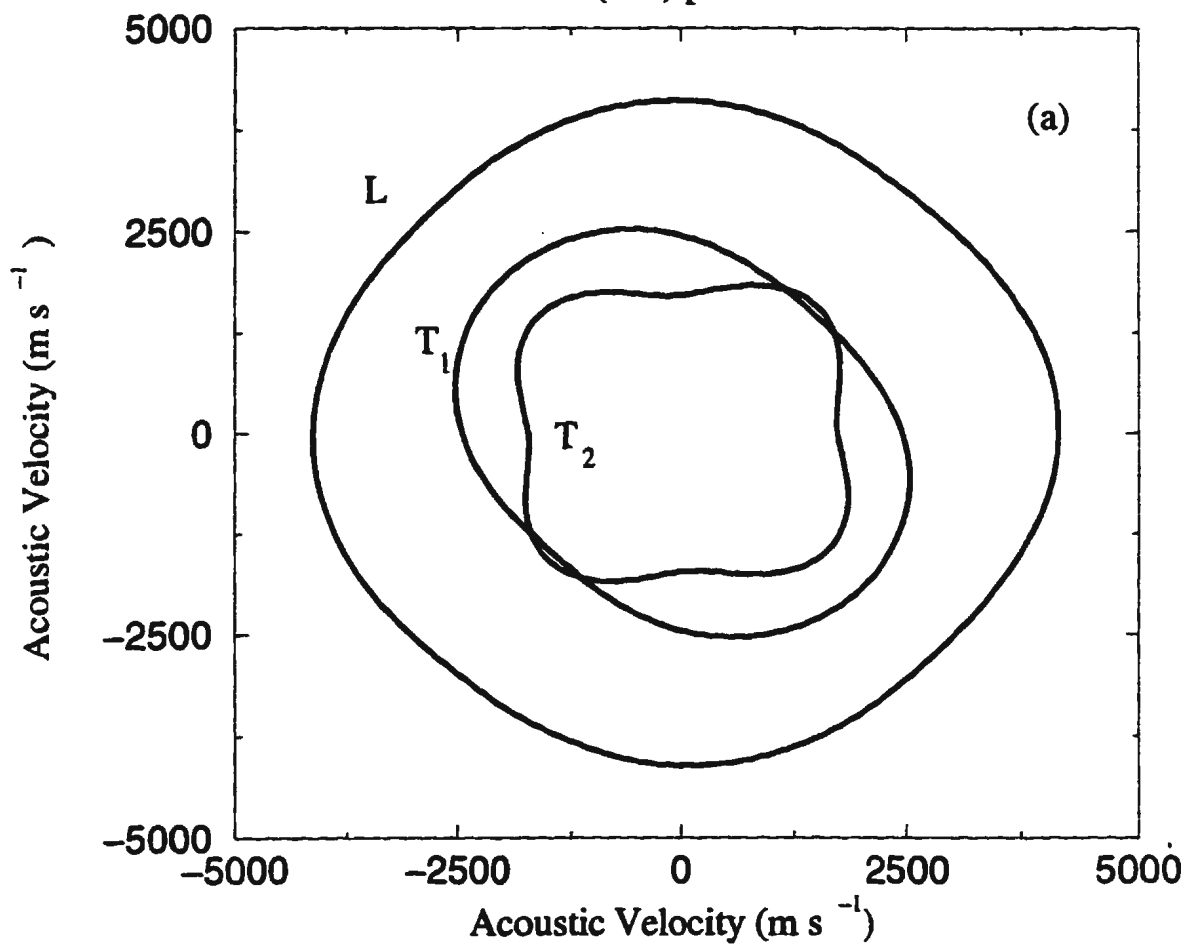
$C_{ij}$  represent the elastic constant values,  $S_{ij}$  represent the elastic compliance constants in units of  $10^3 \text{ kbar}^{-1}$  with an average error of approximately 2.5 %.

**Figure 4.4 Acoustic Velocity in High Symmetry Planes of Ice V**

The acoustic velocity of ice V plotted in polar coordinates for high symmetry crystallographic planes. (a) (010) plane, looking along the b-axis which has 2-fold rotational symmetry, (b) (001) plane, looking along the c-axis.

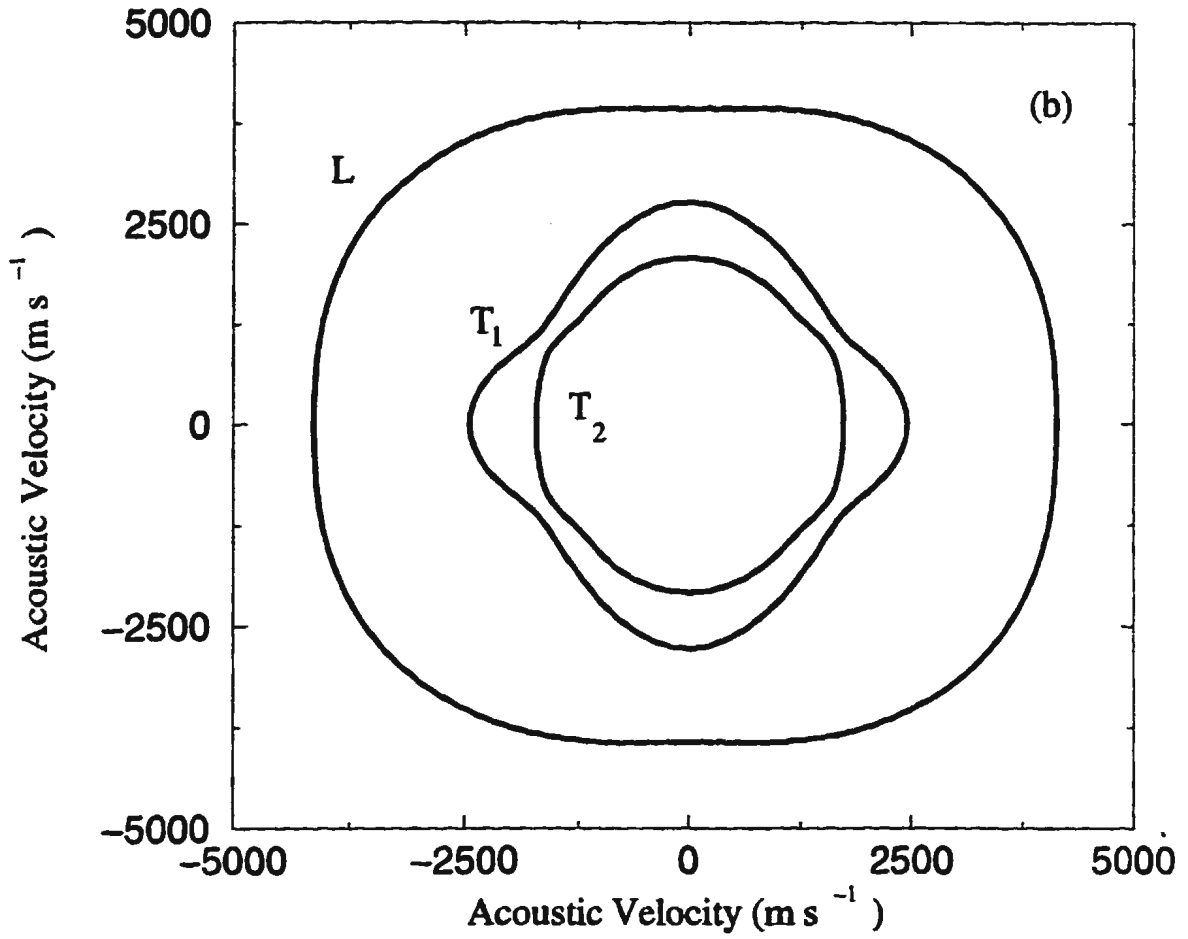
# Acoustic Velocity

(010) plane



# Acoustic Velocity

(001) Plane



the [101] and [101] directions. In the (001) plane, Fig. 4.4 (b), the maximum velocity is  $4383 \text{ m s}^{-1}$  in the [110] and [110] directions and the minimum is  $3935 \text{ m s}^{-1}$  in the [010] and [100] directions.

### ***4.2.3 Derived Polycrystalline Elastic Properties***

The elastic properties of polycrystalline, isotropic ice V samples have been derived following the method outlined in chapter II, section 2.1.3. In Table 4.3 the results are compared with results calculated from acoustic velocity data obtained directly from polycrystalline samples.<sup>31</sup> The excellent agreement amongst the results support the present elastic constant values.

The bulk modulus has been calculated by Eq. 2.18 using the values of the elastic compliance constants found in the previous section. An equation giving the bulk modulus in terms of the elastic constants was not derived due to the complexity of expressions relating the elastic constants and the compliance constants for the monoclinic structure.

The average longitudinal acoustic velocity,  $\bar{V}_L$ , was found by calculating the acoustic velocity in many crystallographic directions through  $4\pi$  steradians and performing the weighted average described by equation 2.17. Other isotropic elastic properties including Young's modulus  $E$ , the Lamé constants  $\mu$  and  $\lambda$ , the average transverse acoustic velocity  $\bar{V}_T$  and Poisson's Ratio  $\sigma$  have been calculated and are presented in Table 4.3. The elastic

**Table 4.3**

**Elastic Properties of isotropic  
Polycrystalline ice V**

	<i>Ice V*</i>	<i>Ice V**</i>
	<i>P = 3.0 kbar T = -35°C</i>	<i>P = 3.0 kbar T = - 35°C</i>
$\bar{V}_L$ (m/s)	4198	4168
$\bar{V}_T$ (m/s)	2164	2186
$B_s$ (kbar)	143	137
$\mu$ (kbar)	58.9	59.6
$\lambda$ (kbar)	103.7	97.3
E (kbar)	155.4	156.2
$\sigma$	0.319	0.310

\* Results from the present study

\*\* Results of R. E. Gagnon, *et al.* <sup>31</sup>.

properties of polycrystalline ice V derived from elastic constant values found in the present study are in excellent agreement with those calculated directly from average acoustic velocity measurements obtained directly from polycrystalline samples.<sup>31</sup> The agreement, in fact, is the best of all phases studied in the present set of experiments.

Finding the elastic constants of ice V proved to be the most difficult of all the phases studied in the present set of experiments. More experiments investigating the pressure dependence of the elastic constants of ice V would greatly complement this work. In particular the elastic properties could be investigated at pressures approaching the phase boundary of ice VI. In the next chapter the elastic constants of ice VI are discussed as the pressure is decreased toward the ice VI-ice V phase boundary.

# CHAPTER V

## Single Crystal Growth and The Elastic Constants of Ice VI

### 5.1 ICE VI

As noted in chapter I, ice VI is structurally very similar to ice III. With regard to the present study two of the most important similarities are: (1) both phases have a tetragonal unit cell, the form of the point group symmetry for ice VI is  $4/mmm$  with 10 molecules per unit cell and dimensions  $a = c = 6.27 \text{ \AA}$  while the point group of ice III is  $422$  and (2) both are optically uniaxial. The optical method of determining the Euler angles  $\theta$  and  $\phi$  of each ice VI crystal is exactly the same as the method used in the case of ice III. In addition, the form of the Christoffel determinant is the same for both ice VI and ice III, and therefore, the computer routine developed to minimize  $\chi^2$ , see equation 3.7, in the case of ice III was quickly adapted to find the elastic constants of ice VI.

#### 5.1.1 Introduction

The bond geometry of ice VI follows the Bernal-Fowler rules and abnormally high density is achieved through the formation of two identical interpenetrating sublattices in which the molecules of one lattice fill the voids of the other. This structure has been described as a "self clathrate". The molecules within each lattice form a hydrogen bonded network but there are no hydrogen bonds connecting the interpenetrating lattices (see chapter I). The interaction between the two lattices in ice VI may be evidenced through

the elastic constants. A comparison of the elastic properties of ice III and ice VI may give some insight into the interaction between the "self clathrate" lattices (in ice VI).

The stability field of ice VI extends to approximately 20 kbar at  $-2^{\circ}\text{C}$ , however, the present study is restricted to pressures below 8.5 kbar for two reasons: (1) hydraulic fluid leaks became more frequent as the pressure was increased, and (2) the hydraulic fluid routinely froze, even with high concentrations of isopentane, at pressures above 7.5 kbar. In total four large single crystals of ice VI were studied at  $-2^{\circ}\text{C}$  and pressures between 6.2 and 8.2 kbar. Crystal #1 was used to determine the elastic constants of ice VI at  $-2^{\circ}\text{C}$  and 7.2 kbar. Crystals #2 and #3 were subsequently used to verify the results found using crystal #1, and to study the elastic behaviour at pressures approaching the phase boundary with ice V. It should be noted that the change of point group symmetry as ice VI transforms to ice V, namely, the point group transformation  $4/mmm \rightarrow 2/m$ , may be proper ferroelastic transition. In proper ferroelastic phase transitions, a distortion of the unit cell occurs at the transition temperature/pressure and is accompanied by major elastic anomalies. Typically strain is the order parameter (or has the same symmetry as the order parameter and couples to it linearly) which softens as the transition is approached. In the case of the ice VI-ice V transition the order parameter is the spontaneous strain  $\epsilon_4$ . A ferroelastic transition between ice VI and ice V would, therefore, be evidenced through softening of the  $C_{44}$  elastic constant as the phase transition was approached at constant temperature. No such evidence was found in the present study. It is, however, likely that the pressure was not sufficiently close to the phase boundary to observe acoustic

softening. The fourth crystal was used to study the pressure dependence of the elastic properties at 7.7 kbar and 8.2 kbar. As with ice III and ice V, the polycrystalline elastic properties were derived and compared with previous experimental results.

## ***5.2 DENSITY, REFRACTIVE INDEX AND EULER ANGLES OF ICE VI***

As with the other phases the density and refractive index of ice were required to determine the elastic constants. They were calculated in a method similar to that used for ice III and ice V.

### ***5.2.1 Density and Refractive Index***

The density of ice VI at -35°C as a function of pressure as determined by Gagnon *et al.*<sup>31</sup> is given by a quadratic equation

$$\rho(P)_{\text{g cm}^{-3}} = 1.1559 + 0.04521 P_{\text{kbar}} - 0.002425 P_{\text{kbar}}^2 . \quad 5.1$$

The units are given by the subscripts in the above equation. The density of ice VI at  $\rho = 7.2$  kbar was determined from the above equation to be  $1.3535 \text{ g cm}^{-3}$ . It is assumed that this value is well within experimental error at -2°C.

As in the previous chapters, the refractive index was found using the function describing the Eulerian strain.<sup>76</sup> (equation 3.2). The index of refraction of ice VI at 7.2 kbar and  $\rho = 1.3535 \text{ g cm}^{-3}$  was found to be 1.4480. The density and index of refraction at the other pressures studied were likewise found. It was estimated that the uncertainty in the density and refractive index is less than 1%.

### **5.2.2 Euler Angles**

The method used to find the orientation of the crystallographic c-axis with respect to the laboratory coordinate system was exactly the same as that used in the case of ice III. For each of the four single crystals studied a set of extinction angle measurements was collected for each orientation  $\Delta\phi$ , through a complete  $360^\circ$  rotation about the laboratory z-axis. These were averaged for each orientation and fit to Eq. 3.6, thus partially orienting the crystal by giving the Euler angles  $\theta$  and  $\phi$ , which correspond to  $\Delta\phi=0.0^\circ$ . The remaining Euler angle  $\chi$  was found during the fit of the elastic constants to the frequency shift data.

The cosine of the measured extinction angle and corresponding angles of rotation  $\Delta\phi$  about the z-axis are given in Table 5.1. This data are plotted and the best fit curves are shown in Fig. 5.1 (a), (b), (c) and (d).

It should be noted that, in the case of ice VI, light transmitted through the crystal was never completely extinguished by rotating the crossed polaroid filters about the laboratory

**Table 5.1**  
**Extinction Angle versus Crystal Orientation Data**  
**Ice VI**

	$\Delta\phi$ (degrees)	cos (extinction angle)
<b>crystal #1</b>		
1	10	-0.4000
2	40	-0.4573
3	70	-0.2990
4	80	-0.2377
5	100	-0.0799
6	120	0.0087
7	150	0.2011
8	180	0.2890
9	210	0.3714
10	240	0.3814
11	280	0.0872
12	310	-0.0958
13	340	-0.3140
<b>crystal #2</b>		
1	0	0.2538
2	30	0.3987
3	60	0.5548
4	90	0.3681
5	120	0.1271
6	150	-0.1513
7	180	-0.3633
8	210	-0.4187
9	240	-0.5262
10	250	-0.5354
11	270	-0.4597
12	300	-0.2317
13	330	0.0680
<b>crystal #3</b>		
1	0	0.3223
2	30	0.1840
3	60	0.0976

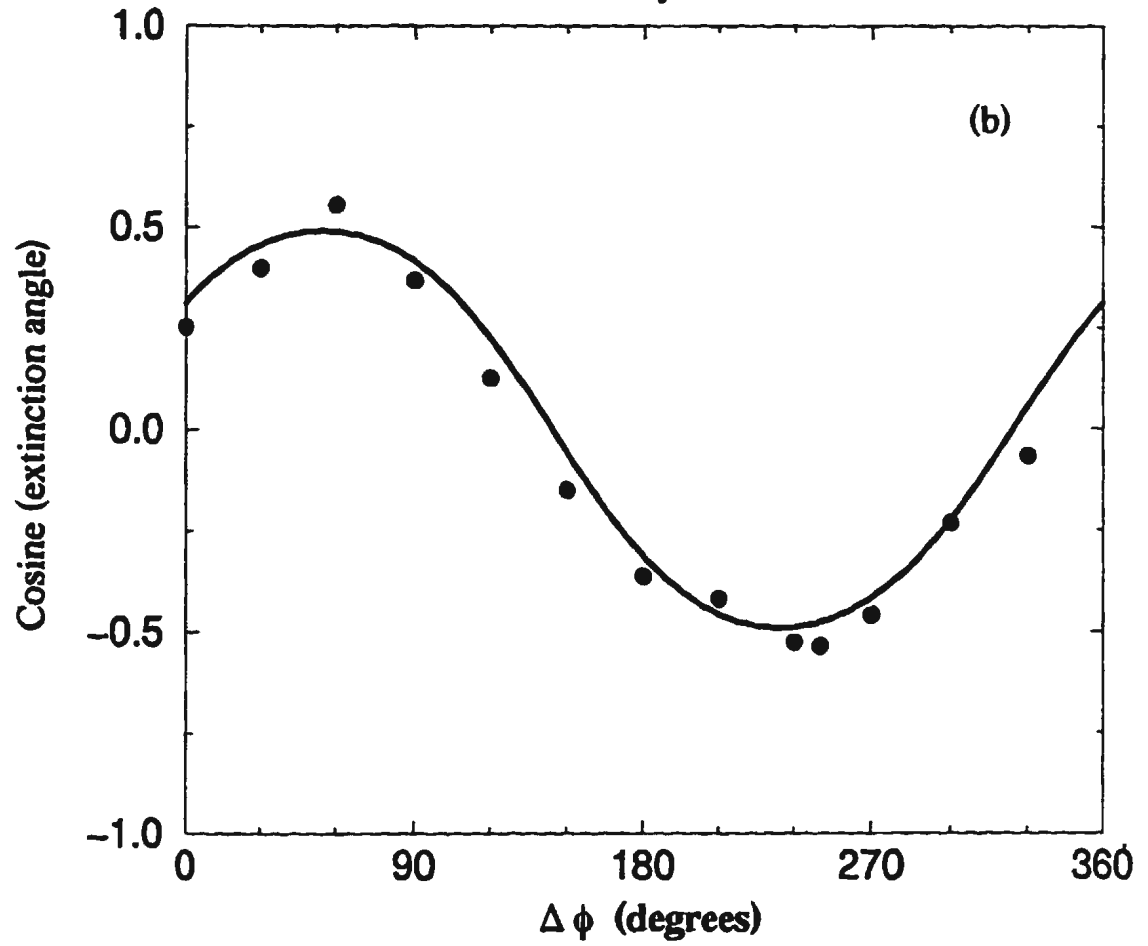
4	90	-0.0105
5	120	-0.1132
6	150	-0.3518
7	180	-0.2840
8	210	-0.1616
9	240	-0.1028
10	270	0.0854
11	300	0.1685
12	330	0.3923
<b>crystal #4</b>		
1	20	0.5861
2	50	0.4462
3	80	0.1729
4	130	-0.3502
5	160	-0.4357
6	190	-0.5050
7	220	-0.4695
8	260	-0.1564
9	290	0.1352
10	320	0.3891
11	350	0.4695

**Fig. 5.1 Extinction Angle versus  $\Delta\phi$**

Plots showing the cosine of the extinction angle as a function of the rotation angle  $\Delta\phi$  about the laboratory z-axis. The solid circles represent the experimental data and the curves were calculated using equation 3.6 and the best fit Euler angles  $\theta$  and  $\phi$ .

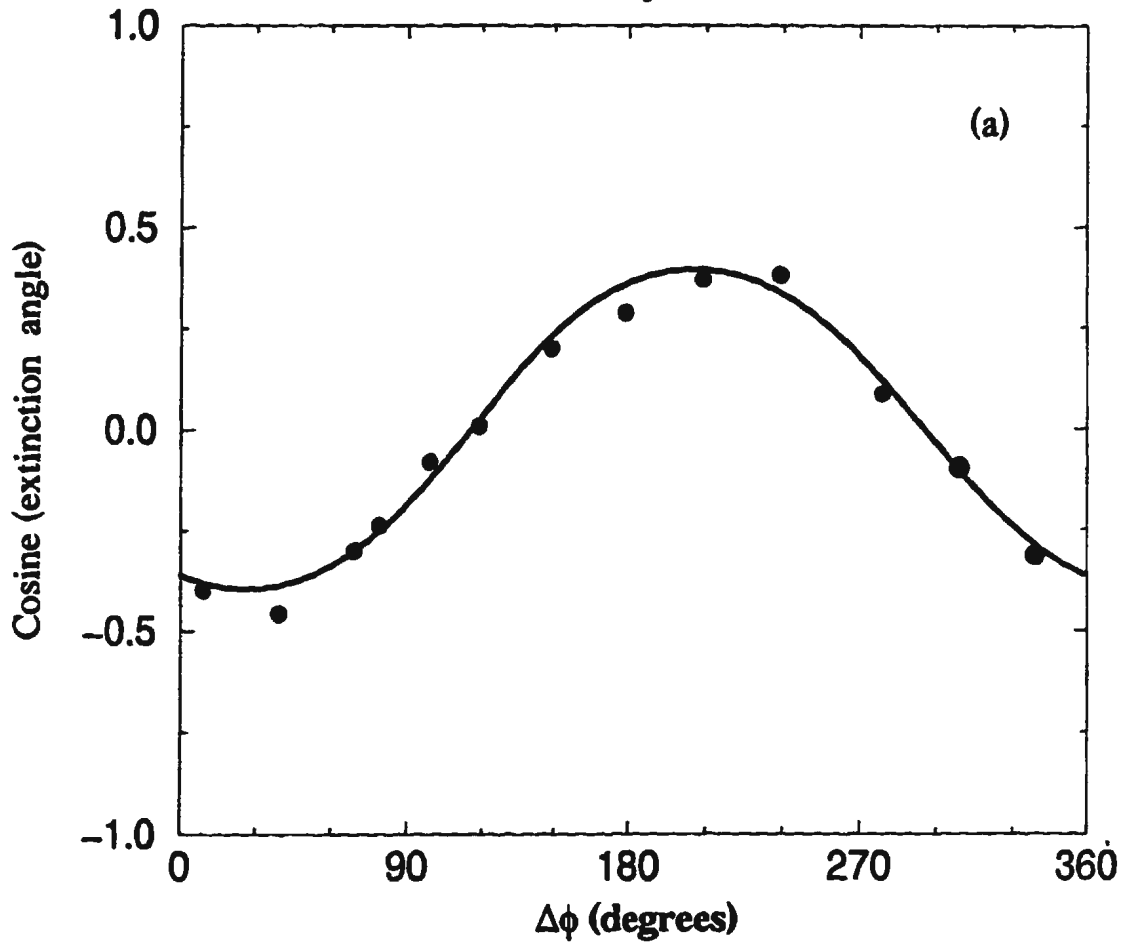
# Orientation Data

Ice VI Crystal #2



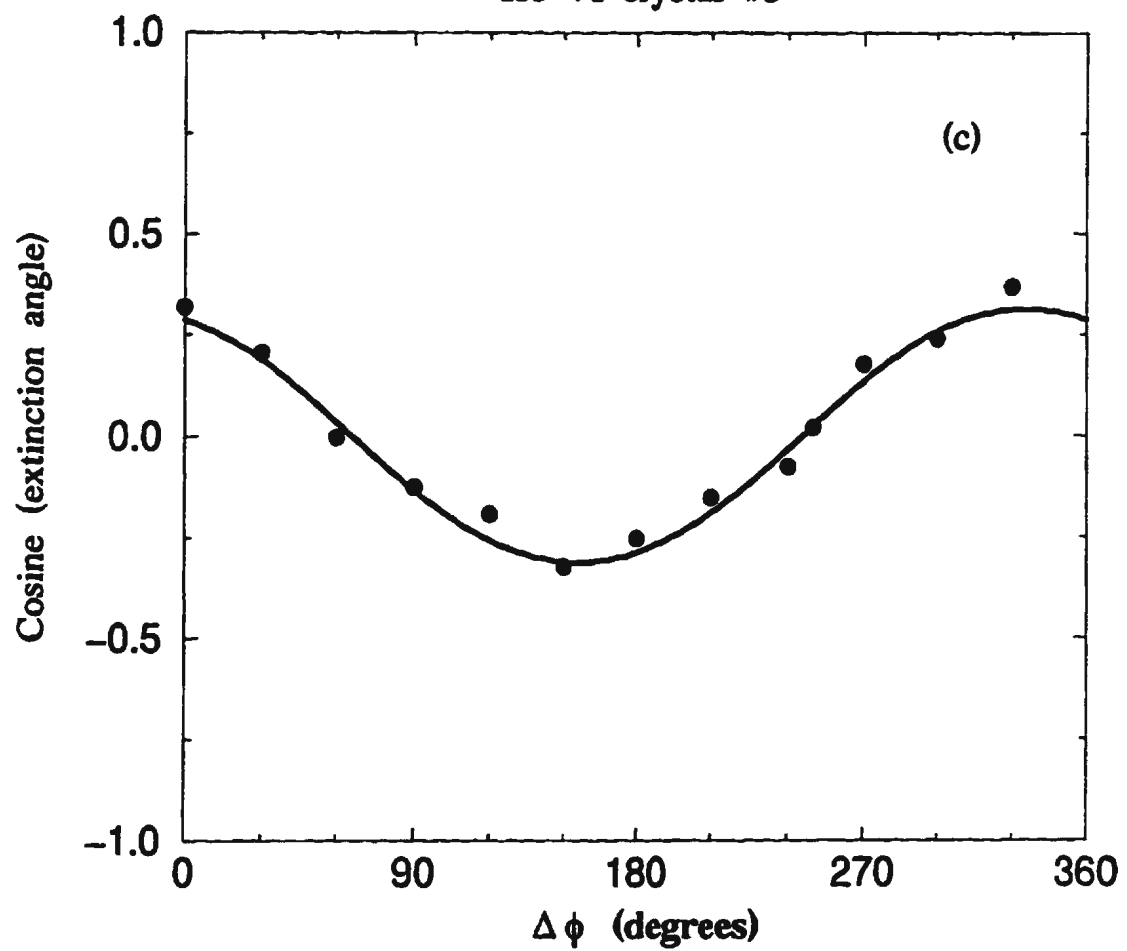
# Orientation Data

Ice VI Crystal #1



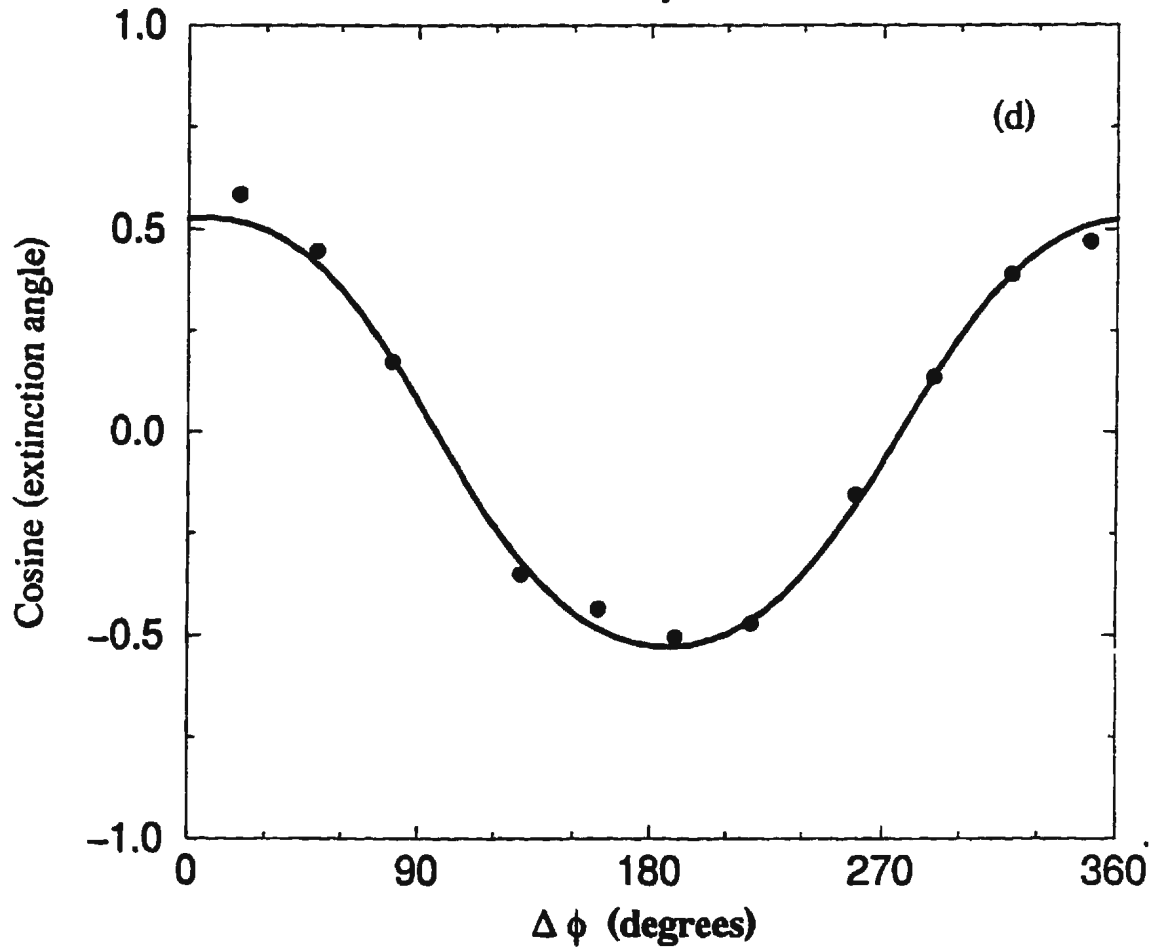
# Orientation Data

Ice VI crystal #3



# Orientation Data

Ice VI crystal #4



y-axis. This is in contrast with ice III, where the extinction of transmitted light was nearly complete at the correct orientation of the polaroid filters. In addition, this gives qualitative evidence that birefringent behaviour of ice VI is very weak, *i.e.* the ordinary and extraordinary refractive index,  $n_i$  and  $n_o$ , differ by a very small amount. Therefore the determination of the exact extinction angle is more difficult to determine and hence increases the scatter in experimental data. Based on a Brillouin spectroscopy experiment, which indicated that the polarization of the incident laser beam had little effect on the frequency shift, it has been suggested by Polian *et al.*<sup>76</sup> that the difference in  $n_i$  and  $n_o$  is less than 1%.

The Euler angles found by birefringence analysis were used as very good initial parameters,  $\theta$  and  $\phi$ , in the non-linear least squares routine which was used to fit the elastic constants to the acoustic data. Therefore 9 parameters, 6 independent elastic constants and 3 Euler angles, were initially fitted to the acoustic data. The agreement with the best fit values of  $\theta$  and  $\phi$  were generally within  $4^\circ$ . These angles were then fixed and the 7 remaining parameters were fitted independently. The best fit value of the Euler angle  $\chi$  was, therefore, fixed and the remaining elastic constant parameters fitted to the acoustic data.

### ***5.3 GROWTH OF SINGLE CRYSTALS OF ICE VI***

As mentioned earlier, small hydraulic fluid leaks developed during almost every attempt to produce ice VI samples. The slow reduction of pressure usually resulted in the sample either melting or changing to ice V. Such small leaks proved very elusive and sometimes led to weeks of down time. On one occasion the entire cryostat and high pressure cell were disassembled to replace a worn O-ring which was thought to be the source of a slow leak around the rotation stem. After reassembling the apparatus an attempt was made to pressurize the cell. It was then discovered that the leak was, in fact, due to a backing ring inside the intensifier. This type of problem persisted throughout the entire experiment and much time was spent trying to find and repair hydraulic fluid leaks (see chapter VI).

### ***5.3.1 Crystal Growth***

In addition to having to overcome problems with leaks in the high pressure system the hydraulic fluid consistently froze within 4 days of growing a single crystal at pressures greater than 6.5 kbar. Though the sample could not be viewed optically and Brillouin spectroscopy was impossible, it was thought that the samples were still in excellent condition. Several unsuccessful attempts were made to increase the temperature in hope that the oil would melt, leaving the ice sample frozen. In an attempt to reduce the freezing point of the hydraulic fluid the Monoplex was mixed with isopentane, initially in a 1:1 ratio and placed inside the high pressure chamber. Unmixed Monoplex pumped into the cell from the intensifier during pressurization was blended with the oil/isopentane mixture by quickly rotating the sample several times. This had a significant effect on the freezing point of the hydraulic fluid and at pressures less than 7.5 kbar proved sufficient

to prevent freezing. At pressures greater than 7.5 kbar the amount of isopentane was increased to 70%, however, this did not prevent solidification of the hydraulic fluid over time. In total, 8 single crystals were grown and oriented, and preliminary Brillouin spectra were collected before the oil froze (thereby causing the sample to be abandoned). The problem was finally resolved by adding isopentane to the oil reservoir inside the intensifier such that hydraulic fluid pumped into the cell during pressurization did not change the oil-isopentane ratio. The lowered viscosity of the mixture nevertheless exacerbated the problems of fluid leaks.

Water samples were prepared in the same manner as for the other crystals, and the general technique used to grow large single crystals of ice VI was similar to that of ice III and ice V. Briefly, samples were produced by pressurizing liquid water at room temperature to approximately 7.5 kbar then cooling the cryostat and sample to approximately -35°C. Liquid water remained supercooled at -35°C for several hours before the onset of solidification. Upon nucleation, water quickly froze directly into a polycrystalline sample of ice VI. In early experiments several polycrystalline samples were slowly depressurized at -8°C resulting in a pronounced phase transformation to ice V at approximately 6.5 kbar. This gave conclusive evidence that ice VI formed from the liquid.

The temperature of the cryostat containing the polycrystalline sample was raised at constant pressure to approximately 0.5°C and the crystal was left to equilibrate for several

hours. The pressure was then reduced to approximately 6.7 kbar, thus initiating a slow and controlled melting process. Melting continued until a small seed crystal remained, the pressure was then slightly increased and the sample began a controlled freezing process. The temperature and pressure were continually adjusted to maintain optimum regrowth conditions. As with the other ice phases this process often resulted in bi-crystalline samples and the melting procedure would have to be repeated. In general it was easier to obtain a suitable single crystal of ice VI than any of the other phases. Figure 5.2 illustrates several video frames showing the growth of an ice VI single crystal seed. Note the well defined crystallographic faces. The time elapsed between consecutive video frames is 1 min. The diameter of the bright region is approximately 1 mm.

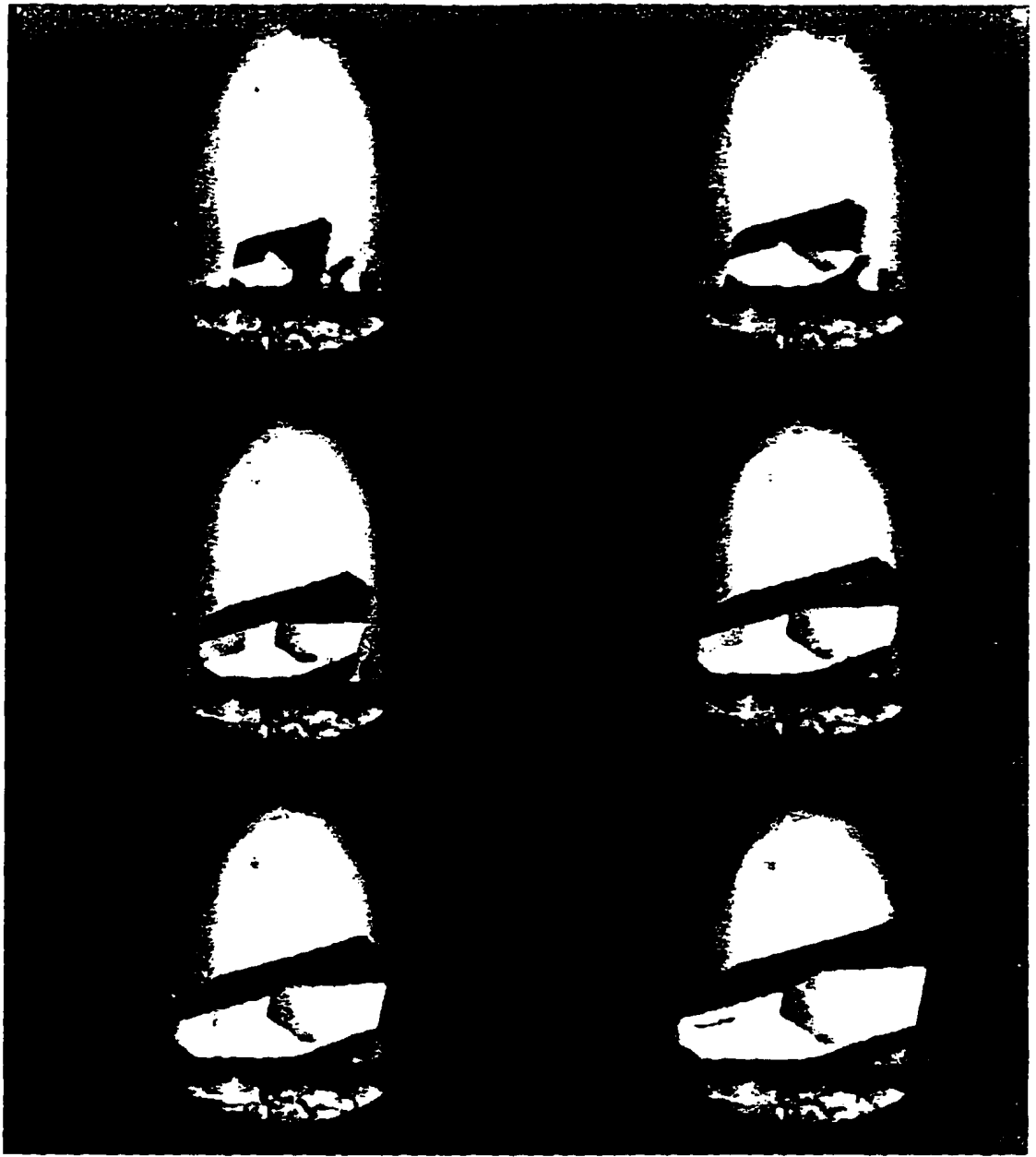
When a single crystal sample of sufficient quality was produced the temperature and pressure were set to  $-2^{\circ}\text{C}$  and 7.2 kbar, respectively. The sample was then allowed to fully anneal for several hours. This entire process typically took two days.

#### ***5.4 RESULTS OF ICE VI STUDIES***

Ice VI spectra were collected in  $\Delta\phi$  intervals of  $10^{\circ}$  or  $20^{\circ}$  through a complete  $360^{\circ}$  rotation about the laboratory z-axis. In these studies a Spectra Physics Series 2000 argon ion laser provided light of approximately 35 mW at 514.5 nm. The free spectral range of the Fabry-Perot was set to 39.19 GHz. This allowed spectra to be collected without overlap of spectral components. A total of 191 frequency shift measurements were

### **Figure 5.2 Growth of a Single Crystal of Ice VI**

**Time lapse images of a single crystal of ice VI growing from liquid water. The images were produced by video taping the samples through a microscope. The seed crystal sits on the glass plug which forms the bottom of the cell and both are visible at the top of each frame. Again, the cylindrical sample containment cell acts as a lens thus the light entering is focussed to the center axis and appears distorted. The diameter of the bright central portion is ~ 1 mm. The time between consecutive frames is ~ 1 min.**



collected from crystals #1, #2, and #3 at 7.2 kbar and  $-2^{\circ}\text{C}$ . A typical Brillouin spectrum, illustrating one longitudinal and two transverse Brillouin doublets is shown in Fig. 5.3. L designates the quasi-longitudinal components and  $T_1$  and  $T_2$  designate the two quasi-transverse components. The transverse components of ice VI were generally very weak with respect to the longitudinal components. The two transverse doublets corresponding to the central Rayleigh peak have been amplified by 10. The very narrow line width of the longitudinal peaks gives qualitative indication that the crystals are of high quality as opposed to the line widths of spectra collected from polycrystalline samples.<sup>31</sup> These spectra were typically collected over 10-12 hours.

#### ***5.4.1 Frequency Shift Data and Elastic Constants of Ice VI***

The frequency shift data for each of the four crystals at all the pressures studied and  $-2^{\circ}\text{C}$  are presented in Table 5.2 along with the corresponding Euler angles. The frequency shift data and curves calculated using the Christoffel determinant, Brillouin equation, and best fit elastic constants are shown graphically in Fig. 5.4. The solid circles represent experimentally determined frequency shifts and the smooth lines represent calculated frequency shifts. Every's closed form expressions were not used to calculate these curves due to problems when the transverse velocity eigenvalues became nearly degenerate. The overall agreement between the experimental and calculated frequency shift is quite good. The quality of the fit is not as good as that of ice III. At higher pressures it was more difficult to maintain precise control over the pressure which fluctuated slightly from day-

**Fig. 5.3 Brillouin Spectrum of Ice VI**

Typical Brillouin spectrum of ice VI, crystal #2,  $\phi = 18.81^\circ$ . L, longitudinal Brillouin components;  $T_1$  and  $T_2$ , transverse Brillouin components. Two complete orders of the Fabry-Perot are shown and  $T_1$  and  $T_2$  are associated with the central unshifted peak has been amplified by 10.

# Brillouin Spectrum

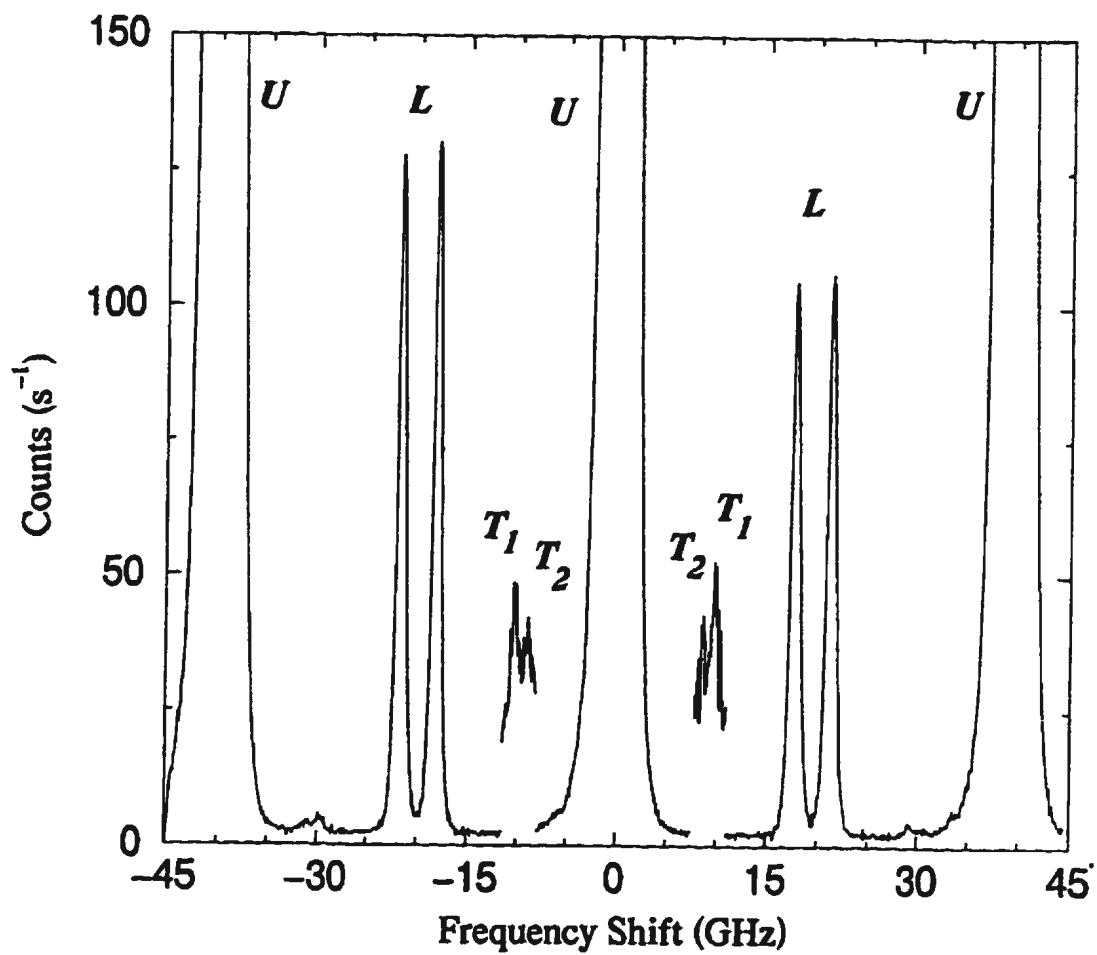


**Table 5.2 (a)**  
**Brillouin Frequency Shifts (GHz) Ice VI**  
**Crystal # 1 ( $\theta=24.71^\circ$ ,  $\phi=68.01$ ,  $\chi=1.74^\circ$ )**

	$\Delta\phi$ (degrees)	L	$T_1$	$T_2$
1	0	17.50	-	9.02
2	10	17.62	9.79	8.70
3	20	17.80	9.74	-
4	40	18.32	9.57	-
5	50	18.41	9.42	-
6	60	18.49	9.28	-
7	80	18.13	9.62	-
8	90	17.88	10.18	8.60
9	100	17.62	10.57	8.54
10	110	17.55	10.73	8.69
11	120	17.63	10.55	8.60
12	130	17.89	10.08	8.66
13	140	18.19	9.62	-
14	160	18.49	9.08	8.77
15	180	18.26	9.41	-
16	200	17.71	9.70	8.56
17	220	17.42	-	8.78
18	240	17.45	-	8.80
19	260	17.48	-	8.74
20	280	17.46	9.07	-
21	300	17.48	-	-
22	320	17.48	9.14	-
23	340	17.39	-	8.88
24	350	17.42	-	8.90

**Table 5.2 (b)**  
**Brillouin Frequency Shifts (GHz) Ice VI**  
**Crystal # 2 ( $\theta=142.28^\circ$ ,  $\phi=40.71^\circ$ ,  $\chi=32.61^\circ$ )**

	$\Delta\phi$ (degrees)	L	$T_1$	$T_2$
	P = 6.5 kbar			
1	10	17.55	10.59	8.87
2	30	17.74	10.01	8.47
3	50	17.92	9.65	8.62
4	170	17.48	9.32	-
5	190	17.41	9.89	8.80
6	210	17.38	-	8.81
7	250	17.68	10.23	8.69
8	270	18.40	9.23	-
9	290	19.03	-	8.79
10	310	19.00	-	8.44
11	330	18.36	9.43	-
12	350	17.74	10.57	8.66
	P = 7.2 kbar			
1	0	17.74	10.60	8.82
2	10	17.59	10.83	8.79
3	20	17.59	10.61	-
4	30	17.82	10.04	8.065
5	40	17.84	9.88	8.76
6	50	17.99	9.68	8.45
7	60	17.95	9.72	8.56
8	70	17.82	9.74	-
9	80	17.73	9.66	-
10	90	17.55	9.36	-
11	100	17.52	9.21	-
12	120	17.54	8.91	-
13	140	17.59	-	-
14	160	17.58	9.01	-
15	180	17.54	9.15	-
16	200	17.56	-	9.07
17	210	17.47	-	8.93
18	220	17.51	-	8.94
19	230	17.49	10.26	8.86

20	240	17.52	10.36	8.77
21	250	17.91	10.25	8.87
22	260	18.05	10.11	-
23	270	18.45	9.40	-
24	280	18.64	-	9.10
25	290	19.03	9.05	-
26	300	19.14	8.78	-
27	310	18.98	8.70	-
28	320	19.03	-	8.58
29	330	18.44	9.37	-
30	340	18.31	9.57	-
31	350	17.77	10.63	8.64

**Table 5.2 (c)**  
**Brillouin Frequency Shifts (GHz) Ice VI**  
**Crystal # 3 ( $\theta=129.30^\circ$ ,  $\phi=299.36^\circ$ ,  $\chi=197.64^\circ$ )**

	$\Delta\phi$ (degrees)	L	$T_1$	$T_2$
	P = 6.2 kbar			
1	0	17.52	9.61	-
2	20	17.21	9.33	-
3	40	17.27	-	8.85
4	60	17.33	9.25	-
5	80	17.32	-	-
6	100	17.25	9.37	-
7	120	17.47	9.57	-
8	140	17.61	9.61	-
9	160	17.45	9.85	-
10	180	17.31	-	8.82
11	200	17.54	10.04	8.86
12	220	18.13	9.43	-
13	240	18.43	9.19	-
14	300	17.36	-	8.81
	P = 7.2 kbar			
1	0	17.56	9.58	-
2	10	17.54	9.68	-

3	20	17.37	-	9.08
4	30	17.38	-	8.94
5	40	17.36	-	8.71
6	50	17.40	9.17	-
7	60	17.51	9.04	-
8	70	17.44	-	-
9	80	17.36	-	8.78
10	90	17.47	9.30	-
11	100	17.40	9.30	-
12	110	17.51	9.48	-
13	120	17.65	9.68	-
14	130	17.69	9.57	-
15	140	17.66	9.70	-
16	150	17.71	9.68	8.55
17	160	17.54	9.97	8.86
18	170	17.53	-	8.84
19	180	17.42	10.48	8.76
20	190	17.56	10.12	8.85
21	200	17.78	9.97	8.75
22	210	18.10	9.56	-
23	230	18.52	9.26	-
24	250	18.36	-	9.29
25	270	17.78	10.01	-
26	290	17.45	10.22	8.81
27	310	17.55	9.89	8.72
28	340	17.84	9.70	-
29	350	17.72	9.68	-

**Table 5.2 (d)**  
**Brillouin Frequency Shifts (GHz) Ice VI**  
**Crystal # 4 ( $\theta=148.09^\circ$ ,  $\phi=86.41^\circ$ ,  $\chi=48.93^\circ$ )**

	$\Delta\phi$ (degrees)	L	$T_1$	$T_2$
	P = 7.7 kbar			
1	0	17.68	10.02	8.90
2	20	17.78	9.67	8.73

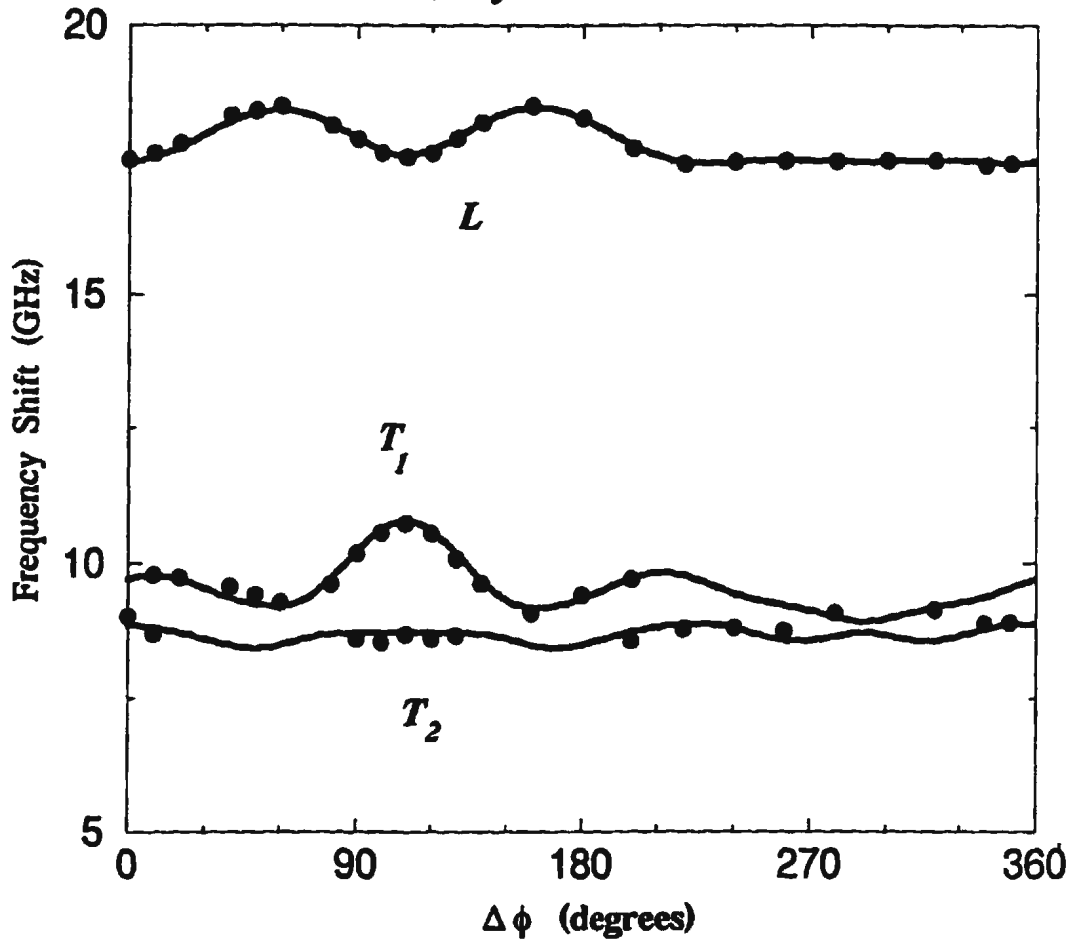
3	40	17.83	9.51	8.41
4	60	17.69	9.26	-
5	80	17.63	8.79	-
6	100	17.61	-	-
7	120	17.66	8.95	-
8	140	17.72	9.51	-
9	160	17.86	9.78	8.32
10	170	17.89	9.68	8.48
11	180	17.95	9.82	8.69
12	190	17.89	10.07	8.84
13	200	17.77	10.38	8.83
14	210	17.73	-	8.85
15	220	17.72	10.77	8.79
16	230	17.99	10.63	8.77
17	240	18.26	10.11	8.67
18	260	18.93	8.90	-
19	280	19.35	-	8.68
20	300	18.95	-	8.94
21	320	18.22	10.12	-
22	340	17.72	10.57	8.78
	P = 8.2 kbar			
1	10	17.88	9.92	8.88
2	30	17.88	9.74	8.68
3	50	17.78	9.69	-
4	70	17.68	-	8.93
5	90	17.77	-	-
6	110	17.75	-	8.95
7	130	17.78	9.43	-
8	150	17.94	9.62	-
9	170	18.08	9.83	8.60
10	190	17.99	10.15	8.88
11	210	17.85	-	8.89
12	230	18.08	10.66	8.77
13	250	18.74	9.52	-
14	270	19.48	-	8.69
15	290	19.48	-	8.71
16	310	18.73	9.54	8.41
17	330	18.03	10.54	8.80
18	350	17.77	-	8.92

**Fig. 5.4 Frequency Shift versus  $\Delta\phi$**

Plots showing the variation of Brillouin frequency shift as a function of rotation angle  $\Delta\phi$  about the laboratory z-axis. The circles represent the experimentally determined frequency shifts and the curves have been calculated from the best fit elastic constants given in Table 5.3.

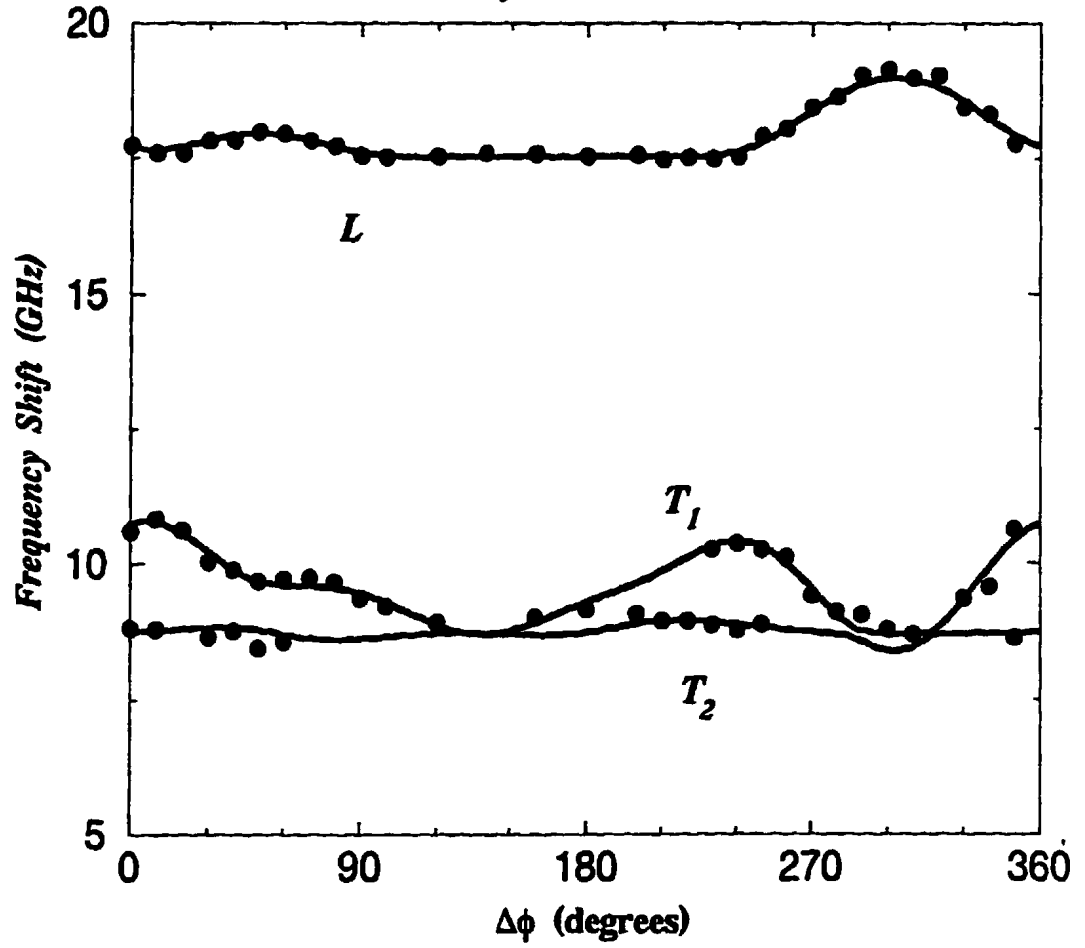
# Frequency Shift vs. $\Delta\phi$

*Ice VI, crystal #1, P=7.2 kbar*



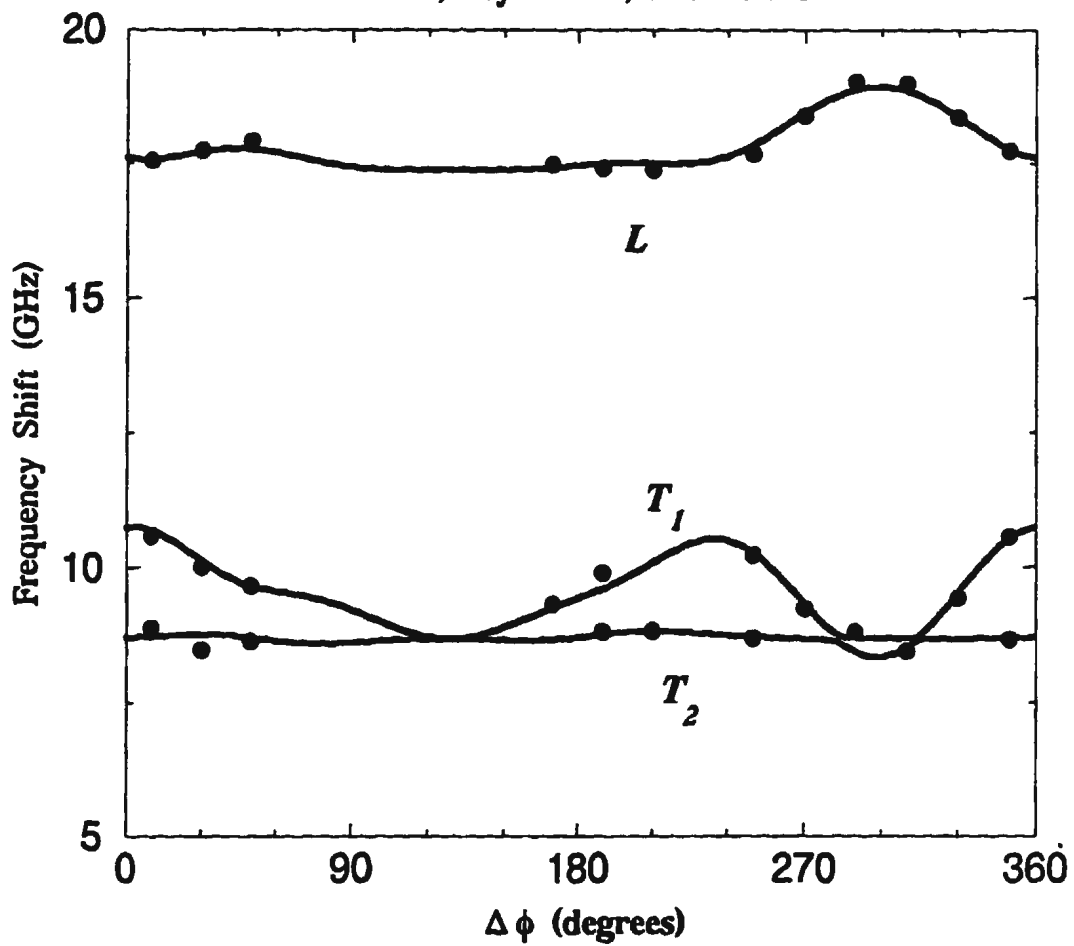
# Frequency Shift vs. $\Delta\phi$

*Ice VI, crystal #2, P=7.2 kbar*



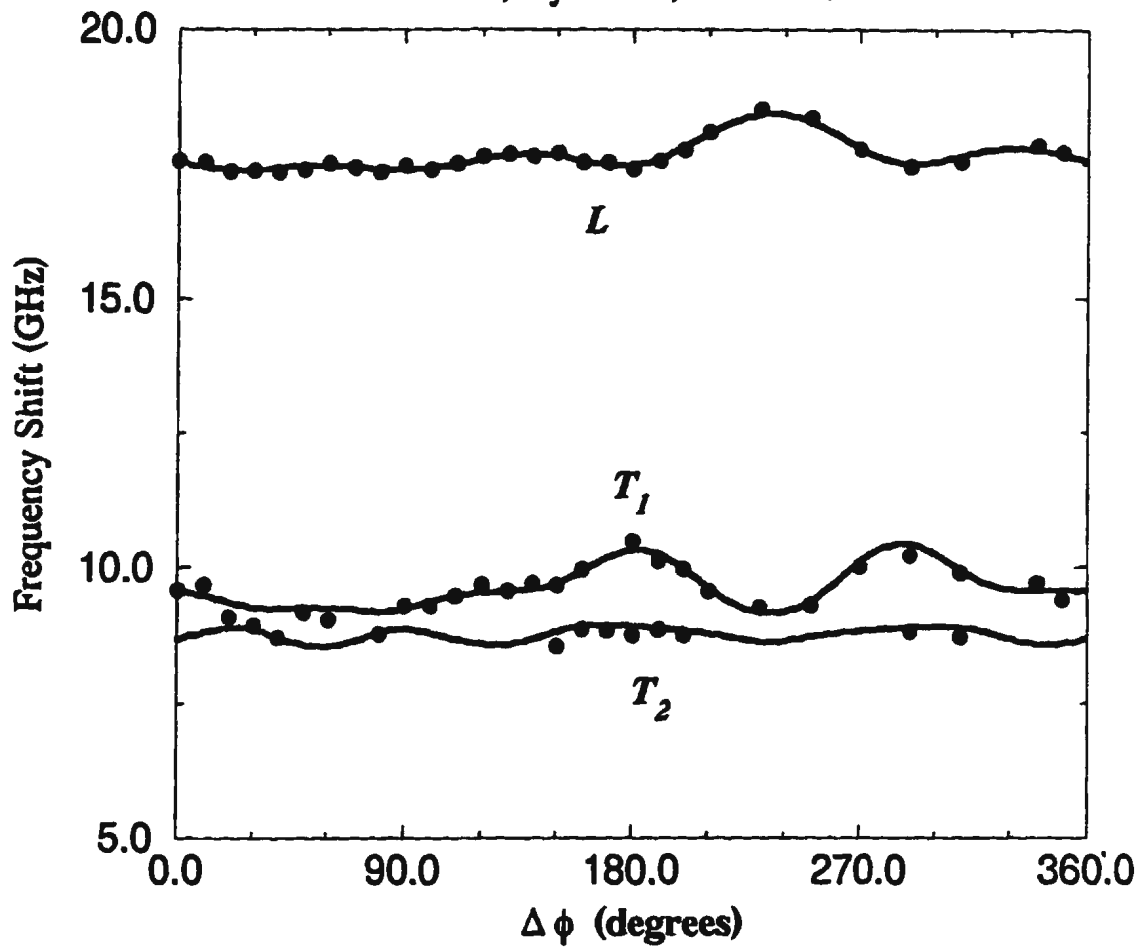
# Frequency Shift vs. $\Delta\phi$

Ice VI, crystal #2, P=6.5 kbar



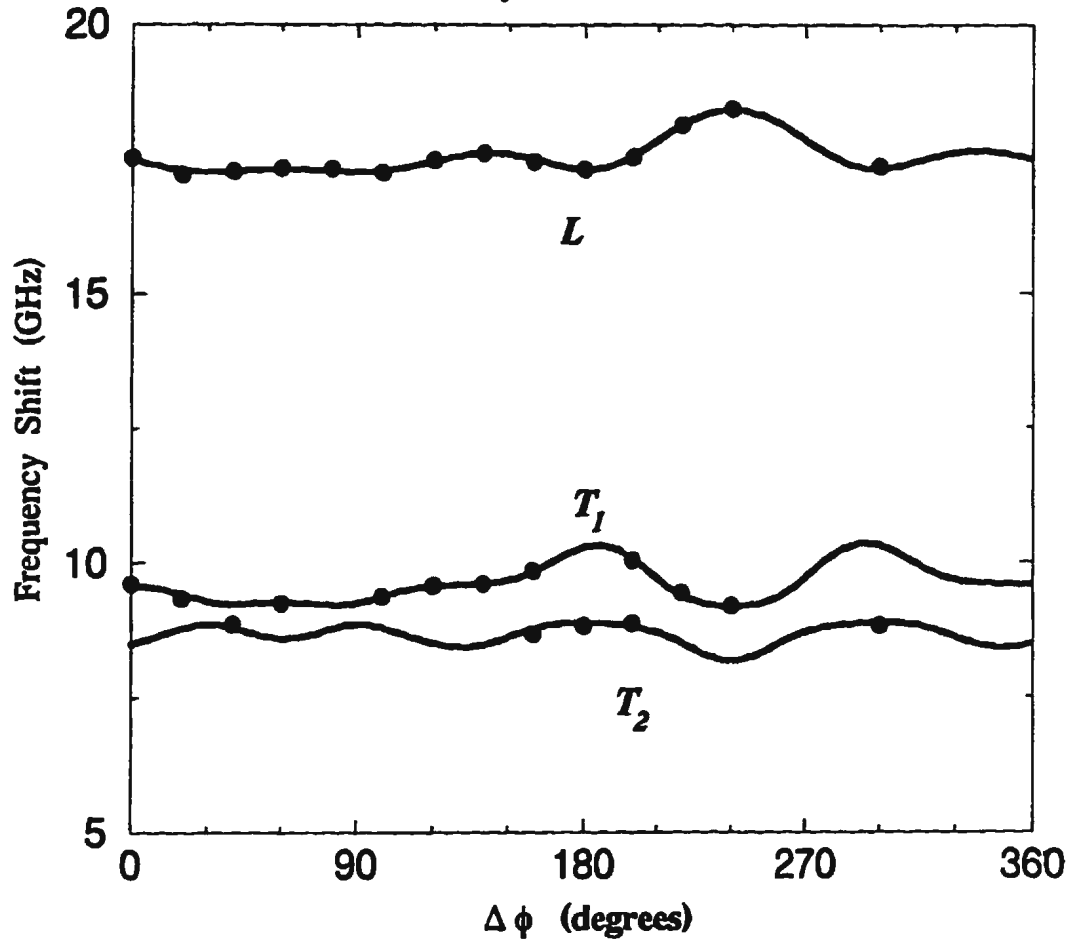
# Frequency Shift vs. $\Delta\phi$

Ice VI, crystal #3, P= 7.2 kbar



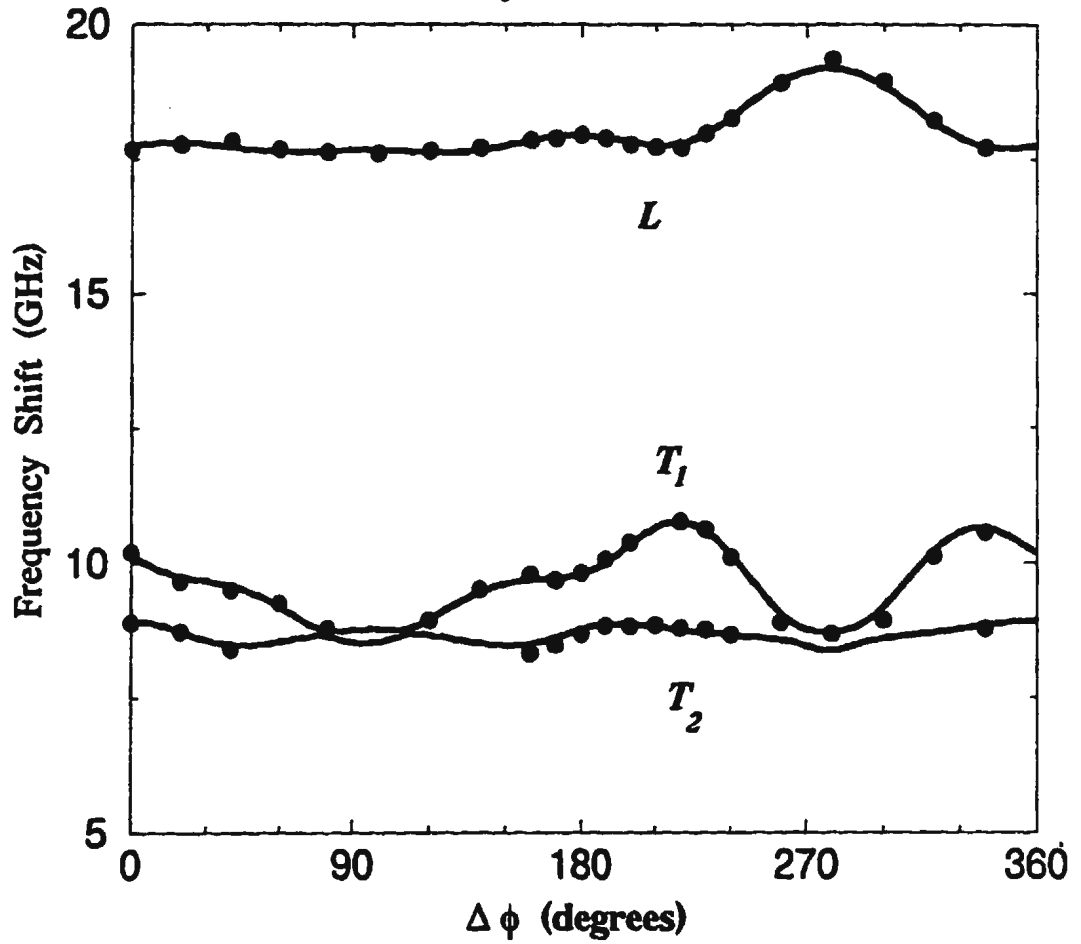
# Frequency Shift vs. $\Delta\phi$

Ice VI, crystal #3, P=6.2 kbar



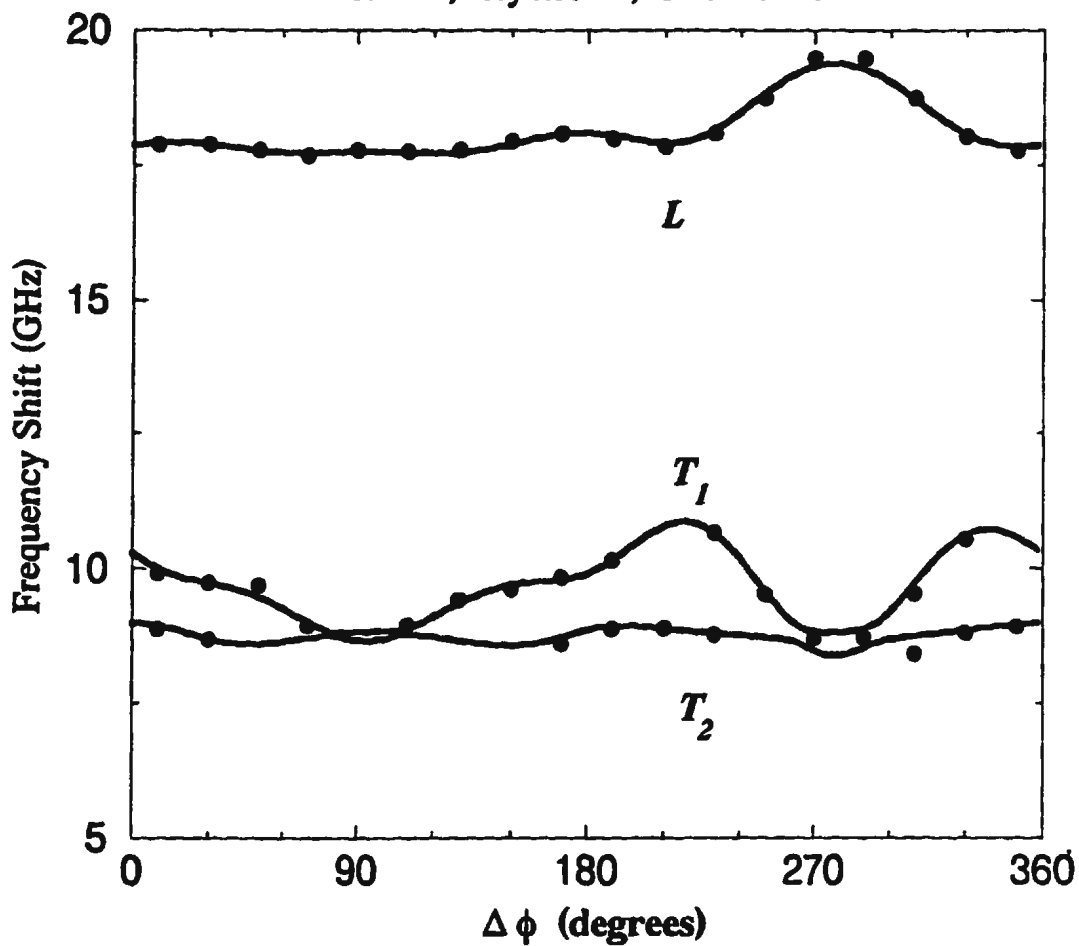
# Frequency Shift vs. $\Delta\phi$

Ice VI, crystal #4, P=7.7 kbar



# Frequency Shift vs. $\Delta\phi$

Ice VI, crystal #4,  $P=8.2$  kbar



to-day and led to slight variations in the data. This effect was kept to a minimum by checking and, if necessary, adjusting the pressure 8 to 10 times per day.

The elastic constants were first fitted to each crystal system independently. The initial parameters used in the non-linear least squares routine were: (1) the elastic constants of ice III, (2) the Euler angles found from the birefringent measurements and (3)  $\chi=45^\circ$ . The resulting elastic constants, see Table 5.3, were found to be very consistent with the exception of  $C_{12}$ , which varied by approximately 2%. The quality of the fit (especially in regions where  $T_1$  and  $T_2$  are nearly degenerate) was found to be very sensitive to  $C_{12}$  and slight differences in frequency shift resulted in significant differences in  $C_{12}$ . The data from all three of the crystals at  $-2^\circ\text{C}$  and 7.2 kbar were then combined and the non-linear least squares routine run again to calculate a final set of elastic constant values. When the three Euler angles  $\theta$ ,  $\phi$  and  $\chi$  were uniquely determined the elastic constants were calculated independently using the Elcon program. The errors quoted in Table 5.3 represent one standard deviation in the best fit parameters and are caused by uncertainties in the frequency shift and crystal orientation. There is an additional systematic error of about 1% caused by uncertainty in the scattering angle and refractive index (see section 3.1.4).

In measuring acoustic velocities in polycrystalline samples, Polian and Grimsditch<sup>76</sup> noted that some experimental data were collected from very small single crystal samples, and that the longitudinal frequency shift was independent of whether the sample was single

**Table 5.3**  
**Elastic Constants of Ice VI**  
 Elastic constants are given in units of  $\times 10^4$  bar at  
 $T = -2^\circ\text{C}$ , and  $P = 7.2$  kbar.

	$\theta$	$\phi$	$\chi$	$C_{11}$	$C_{12}$	$C_{13}$	$C_{33}$	$C_{44}$	$C_{66}$
Ice VI (a)	24.71	68.01	1.74	26.69	14.73	12.94	26.18	6.31	10.38
Ice VI (b)	142.28	40.71	32.61	26.89	14.57	12.82	26.37	6.36	10.33
Ice VI (c)	129.30	299.36	197.64	26.95	14.17	12.81	26.20	6.19	10.54
Ice VI <sup>†</sup>				26.84 $\pm 0.8\%$	14.52 $\pm 2.0\%$	12.82 $\pm 1.8\%$	26.21 $\pm 1.0\%$	6.31 $\pm 1.1\%$	10.38 $\pm 1.4\%$
				$S_{11}$	$S_{12}$	$S_{13}$	$S_{33}$	$S_{44}$	$S_{66}$
Ice VI <sup>‡</sup>				57.39	23.23	-16.97	54.76	158.5	96.34

<sup>†</sup> All data analyzed together.

<sup>‡</sup> Elastic compliance constants in units of  $\times 10^4$  kbar<sup>-1</sup> with average error of 2.5%.

or polycrystalline. From this they suggest that ice VI may be elastically isotropic, a conclusion which may also be made by noting the small variation in the measured frequency shifts with  $\Delta\phi$  in the present study. Polian *et al.* approximate  $C_{11}$  by assuming ice VI to be isotropic such that  $V = (C/\rho)^{1/2}$  with  $C = C_{11} = 28 \times 10^4$  kbar. This is in rough agreement with the present results. Polian and Grimsditch discuss evidence in their paper which suggests that there was a preferred orientation of crystal growth in the diamond anvil cell.

The elastic constants at pressures between 6.2 and 8.2 kbar were found using the non-linear least squares routine with the values of the elastic constants at 7.2 kbar and  $-2^\circ\text{C}$  as initial parameters. These elastic constants and the corresponding pressures are given in Table 5.4. The pressure dependence of the elastic constants was then found by fitting the experimentally determined elastic constants to linear equations which are quoted below

$$C_{11} (P) = 0.9739 P_{\text{kbar}} + 19.94$$

$$C_{12} (P) = 0.5966 P_{\text{kbar}} + 10.80$$

$$C_{13} (P) = 0.5440 P_{\text{kbar}} + 8.97$$

$$C_{33} (P) = 0.7998 P_{\text{kbar}} + 20.54$$

**Table 5.4**  
**Elastic Constants,<sup>†</sup> Density<sup>‡</sup> and Refractive Index**  
**of Ice VI, T = -2 °C, in the Pressure Range 6.2-8.2 kbar**

Pressure (kbar)	$\rho$	n	$C_{11}$	$C_{12}$	$C_{13}$	$C_{33}$	$C_{44}$	$C_{66}$
6.2	1.3427	1.4447	25.88	14.83	12.14	25.49	6.45	10.09
6.5	1.3478	1.4463	26.44	14.60	12.76	25.77	6.42	10.09
7.2	1.3535	1.4480	26.84	14.52	12.82	26.21	6.31	10.38
7.7	1.3596	1.4499	27.53	15.51	13.25	26.84	6.21	10.60
8.2	1.3629	1.4509	27.90	15.91	13.36	27.04	6.44	10.67

<sup>†</sup> in units of  $\times 10^4$  bar.

<sup>‡</sup> in units of  $\text{g cm}^{-3}$ .

$$C_{44} (P) = - 0.0460 P_{\text{kbar}} + 6.69$$

$$C_{66} (P) = 0.3258 P_{\text{kbar}} + 8.03 \quad . \quad 4.2$$

The units of the elastic constants in the above equations are  $10^4$  bar. Fig. 5.5 illustrates graphically the pressure dependence of the elastic constants and the best fit lines.

#### ***5.4.2 Derived Polycrystalline Elastic Properties***

As with the other phases of ice studied, the isotropic elastic properties of polycrystalline ice VI have been calculated from the single crystal elastic constants and compared to values measured directly from polycrystalline samples. These calculations closely follow the method outlined in chapter II. Equation 3.11 was used to calculate the bulk modulus, and the average longitudinal acoustic velocity was found by calculating acoustic velocities in crystallographic directions covering the solid angle  $4\pi$  and then performing a weighted average (see equation 2.17). From the bulk modulus and  $\bar{V}_L$  other isotropic elastic properties were calculated. These values at 7.2 kbar and  $-2^\circ\text{C}$  are given in Table 5.5. Agreement between the values calculated from the present single crystal elastic constant data and the values obtained directly from experiments with polycrystalline samples<sup>31</sup> is good.

**Fig. 5.5 Elastic Constants of Ice VI as a Function of Pressure**

Plots showing the variation of the elastic constants of ice VI at  $-2^{\circ}\text{C}$  between 6.2 and 8.2 kbar. The lines represent the lines of best fit given by Eq. 5.2.

## Elastic Constants vs. Pressure

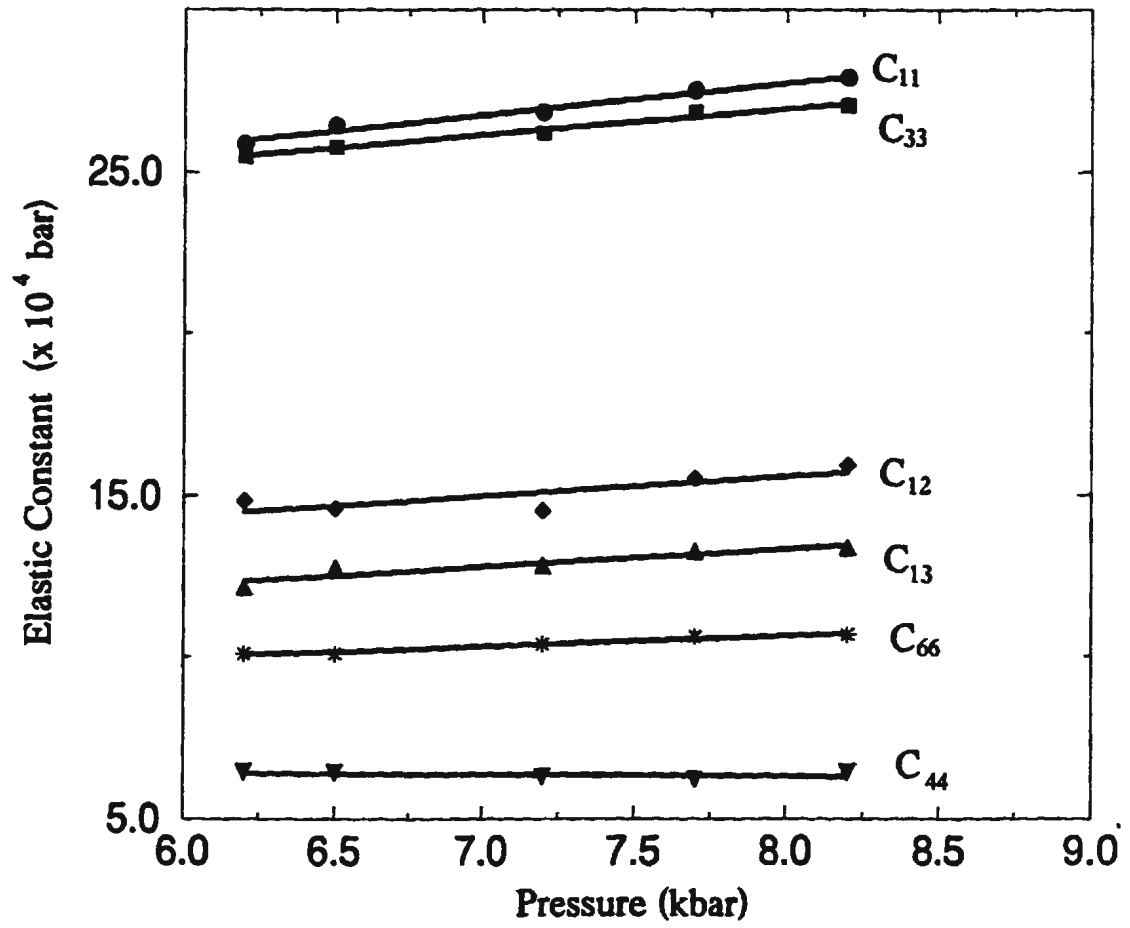


**Table 5.5**  
**Elastic Properties of Isotropic**  
**Polycrystalline Ice VI**

	P = 7.2 kbar T = -2°C	P = 7.2 kbar T = -35°C
$\bar{V}_L$ (m/s)	4473	4517
$\bar{V}_T$ (m/s)	2272	2316
$B_s$ (kbar)	177.7	179.3
$\mu$ (kbar)	69.9	72.6
$\lambda$ (kbar)	131.1	130.9
$E$ (kbar)	185.4	191.9
$\sigma$	0.326	0.321

The elastic constants given in Table 5.4 were subsequently used to find the pressure dependence of the elastic properties of isotropic polycrystalline aggregates of ice VI. The equations best representing pressure dependence of the isotropic polycrystalline elastic properties may be written as,

**Bulk Modulus:**

$$B_s(P)_{\text{kbar}} = 6.7804 P_{\text{kbar}} + 130.77 \quad 5.3$$

**Young's Modulus:**

$$E(P)_{\text{kbar}} = 3.0278 P_{\text{kbar}} + 163.18 \quad 5.4$$

**Average Acoustic Velocity:**

$$\bar{V}_L(P)_{\text{m/s}} = 49.82 P_{\text{kbar}} + 4126$$

$$\bar{V}_T(P)_{\text{m/s}} = 7.46 P_{\text{kbar}} + 2219 \quad 5.5$$

**Poisson's Ratio:**

$$\sigma(P) = 3.551 \times 10^{-3} P_{\text{kbar}} + 0.3026 \quad 5.6$$

**Lamé Constants:**

$$\mu(P)_{\text{kbar}} = 0.9574 P_{\text{kbar}} + 62.74$$

$$\lambda(P)_{\text{kbar}} = 6.1325 P_{\text{kbar}} + 89.01 \quad 5.7$$

The acoustic velocity in several crystallographic planes has also been calculated and plotted in polar coordinates in Fig. 5.6. The plots suggest that ice VI is quite acoustically isotropic, as discussed earlier, especially in the (010) plane. There is some variation in the longitudinal acoustic velocity in the (001) plane, Fig. 5.6 (a), the maximum,  $V_{\text{max}} = 4650 \text{ m s}^{-1}$  in the [110] and  $[\bar{1}\bar{1}0]$  directions, and the minimum,  $V_{\text{min}} = 4380 \text{ m s}^{-1}$  in the [100] and [010] directions. The narrow longitudinal Brillouin line width in the experiments performed on polycrystalline samples by Gagnon *et al.*<sup>31</sup> suggests that the randomly oriented crystal grains in the scattering region produce roughly the same acoustic frequency shift, thereby indicating acoustic isotropy.

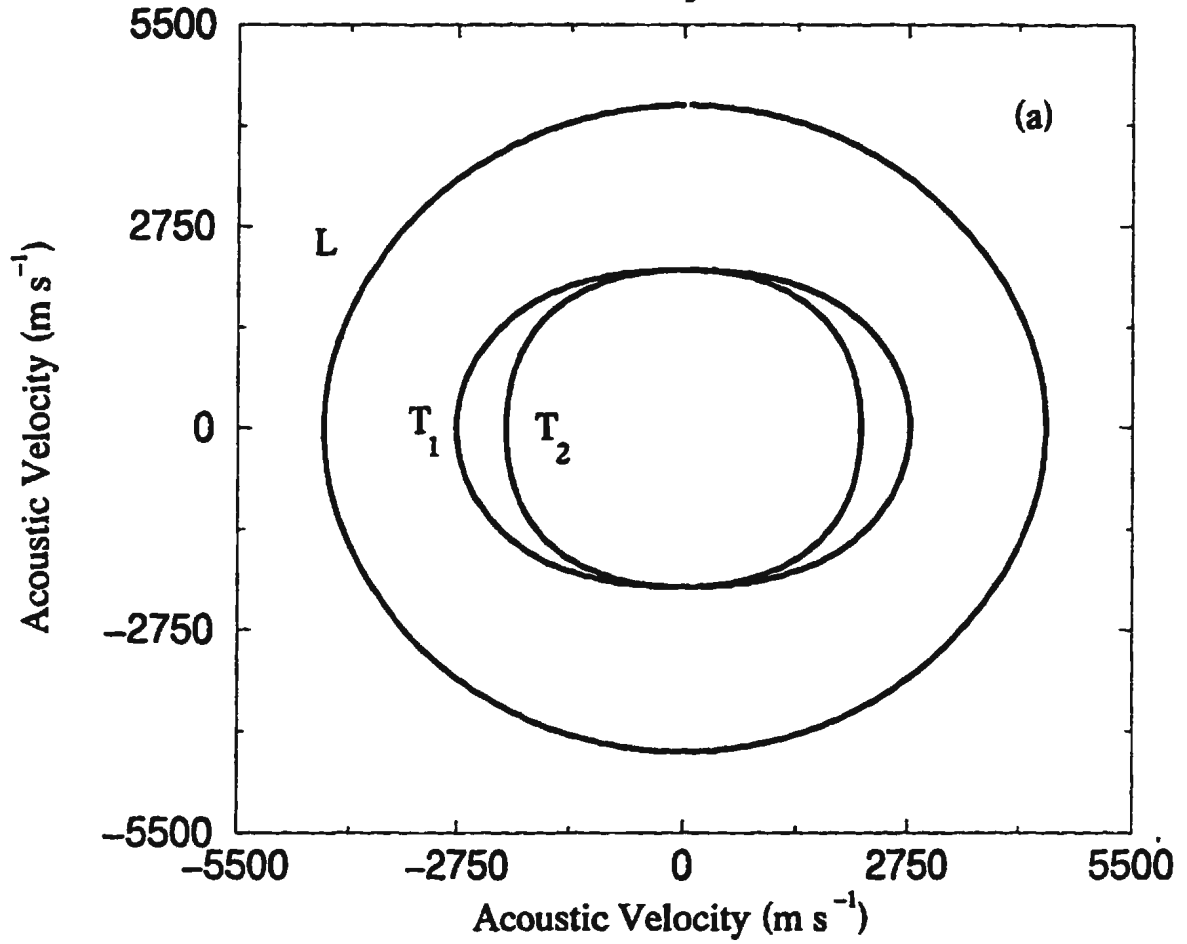
The elastic constants of ice VI have been studied at pressures between 10.5 and 21 kbar by Shimizu *et al.*<sup>77</sup> The elastic constants found in the present study can be extrapolated to 12.3 kbar and compared with the results of Shimizu *et al.* (in brackets) as follows;  $C_{11} = 31.9$  (32.8),  $C_{12} = 18.14$  (11.8),  $C_{13} = 15.66$  (14.7),  $C_{33} = 30.38$  (27.8),  $C_{44} = 6.12$  (6.12) and  $C_{66} = 12.03$  (5.9)  $\times 10^4$  bar. It should be noted that the samples used in the study by Shimizu *et al.* were produced in a diamond anvil cell and were necessarily very small. It is quite likely the elastic properties of such small samples are subject to surface effects. In addition, Shimizu *et al.* collected data from only one sample and it was evident from the present work that at least two independent systems are required to fix all the elastic constants with any certainty.

**Fig. 5.6 Acoustic Velocity in High Symmetry Planes of Ice VI**

Plots of acoustic velocity of ice VI in polar coordinates calculated from the best fit elastic constants. Two crystallographic planes are shown, namely (a) (001) plane; (b) (010) plane.

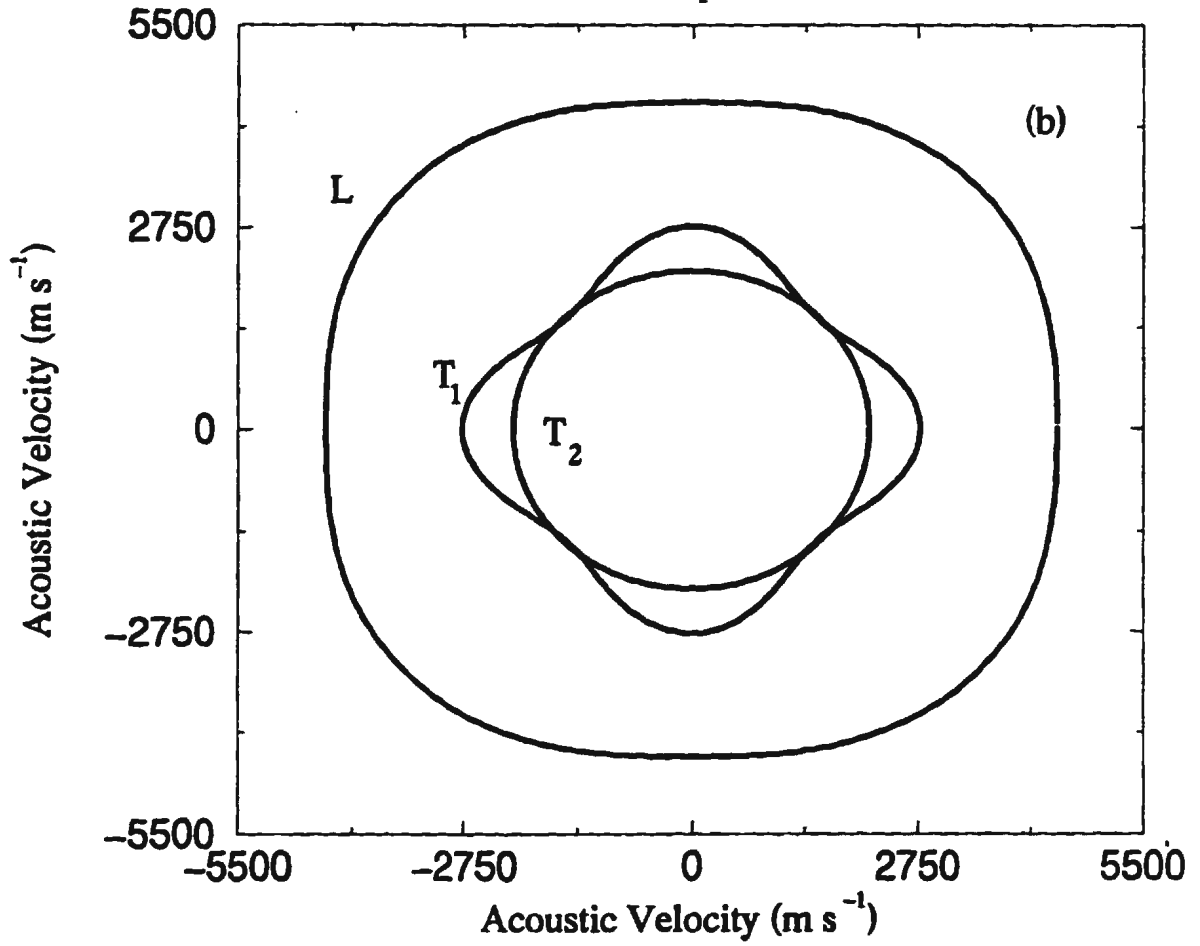
# Acoustic Velocity

(010) plane



# Acoustic Velocity

(001) plane



Various technical difficulties encountered during the present experiment and the methods by which they were overcome are discussed in the next chapter. In addition, brief comparison of the acoustic behaviour of ice III and ice VI (which both have tetragonal crystal symmetry) is made.

# Chapter VI

## Conclusions

### *6.1 Experimental Difficulties*

During the course of the present set of experiments various experimental difficulties were encountered and many successfully overcome. For example, more than an entire year was devoted exclusively to the development of the technique used to produce single crystals of ice III, V and VI. In addition, almost an entire year was taken in attempts to produce high quality single crystals of ice II. This section describes many of the difficulties and discusses the various attempts to overcome experimental problems.

#### *6.1.1 Determination of Crystal Growth procedure*

The first sample containment cell was made from a long glass tube closed at one end and cut to fit nicely into the high pressure chamber. The cell was not attached to the rotation stem and as a result the sample could not be rotated while under pressure. The sole purpose of the cell was to develop a method of growing suitable samples and in rough form was totally unsuitable for Brillouin spectroscopy. Cylindrical samples were cut from a single crystal of ice Ih. The ice was melted until its diameter was smaller than that of the sample containment cell, which was filled with cold Monoplex™ hydraulic oil. The sample was inserted into the glass containment cell so that no air bubbles were present.

Once placed in the high pressure chamber, the glass cell and specimen were cooled and pressurized.

As mentioned in previous chapters, high pressure phases were initially produced by simply pressurizing ice Ih at approximately  $-30^{\circ}\text{C}$ . Phase transitions were evidenced by viewing samples with the aid of a microscope, video camera and video monitor. The resulting high pressure polymorphs were always fine grained polycrystals and extremely cloudy due to infiltration of the surrounding oil into the specimen. It was clear that any method used to produce single crystals suitable for Brillouin spectroscopy would include measures to ensure that no oil penetrated the specimen upon pressurization.

In an attempt to reduce oil penetration, samples were placed in a glass cell filled with cold liquid water rather than oil. The excess water was frozen so that ice Ih completely filled the glass cell. Upon pressurization through the ice Ih - ice III phase transition much less oil penetrated into the specimen, however, still far too much for successful light scattering experiments. It became evident that such a method did not produce the necessary single crystals and instead resulted in fine grained polycrystalline samples. It was required that high quality samples be grown from liquid water.

Samples were subsequently produced by pressurizing ice Ih into ice III and heating the high pressure cell to the ice III - liquid water phase boundary, as determined from the phase diagram, Fig. 1.2. The pressure was reduced until the sample started to melt. It was

found that the melting rate was very sensitive to slight changes in pressure. This meant that single crystals would likely be produced if the sample could be melted and regrown when only a small single crystal seed remained. Note that the bottom of the glass cell was well below the viewing windows and therefore the seed crystal was completely out of view. Several attempts were made to estimate the melt rate in order to predict when the sample would melt completely and repressurize at the right moment to catch a single crystal seed. This always led to one of two possible results: (1) regrowth of a polycrystalline seed resulting in another polycrystalline sample, or (2) the sample melted completely before repressurization. It was clear that in order to grow a single crystal the bottom of the cell must be visible through the viewing windows and the pressure increased at precisely the moment before the sample melted completely.

A sample containment cell was designed with great care to ensure that the bottom could be viewed through the windows. Several cells were handmade and the most suitable used in the experiment. A coupling was also designed to fix the sample cell to the rotation stem such that the sample could be rotated as required to keep the seed crystal in view. The successful design led to a seed crystal which was clearly visible and was in contrast with the background (this design is described in chapter II). With practice large single crystals were produced. Significant quantities of oil still penetrated into the sample during the ice I<sub>h</sub> - ice III transition. The samples were subsequently isolated from the oil by a thin silicone disk seated inside the glass cell and on top of the sample (see Fig. 2.5). It was subsequently discovered that very little oil penetrated the specimen if liquid water

was first pressurized and then cooled directly into the desired phase, thus high quality, oil free single crystals could be grown. Once a single crystal high pressure sample had been produced it could not be melted and refrozen without significant amounts of oil penetrating into the glass containment cell. After each experimental run, therefore, the cell was heated to room temperature, dismantled, cleaned and the water sample replaced. This greatly increased the time and effort required to perfect the crystal growth technique. On one occasion a spent sample was melted while under pressure and upon depressurization the sample refroze into ice Ih causing the cell to fracture. This led to more than a week down time while another glass cell was being made.

The bottom of the sample cell covered up to one third of the viewing window. The amount of ice visible through the windows was therefore reduced creating some difficulty when focusing the collecting lens of the Fabry-Perot. This problem was overcome by placing a plane glass plate in front of the collecting lens. Tilting the plate caused the focus of the collecting lens to be slightly displaced, thus fine adjustments of the optical alignment were possible. Such a glass plate was often used to ensure light scattered from a suitable sample volume was passed through the Fabry-Perot.

### ***6.1.2 Efforts to Grow Single Crystals of Ice II***

Several attempts were made to produce single crystals of ice II suitable for Brillouin spectroscopy. Some attempts have been briefly described in chapters III and IV. Since ice II does not share a common border with liquid water the main task was to induce a slow

phase transformation to ice II from one of the neighbouring solid phases. Cooling the high pressure cell to temperatures low enough to induce the phase transition was difficult. It was thought that cooling a single crystal of ice III or ice V would result in a slow phase transition and consequently result in a single crystal of ice II. As discussed earlier the cell was cooled by thermoelectric modules attached directly to the side of the high pressure cell. A temperature gradient is created in the thermomodules as current is supplied. The higher the current, the higher the thermal gradient, however, self heating effects take over as the current is increased beyond ~ 10 amps. The warmer sides of the thermal modules were cooled by passing a mixture of methanol and water at ~ -20° C from a Neslab circulating cooler through tubes acting as a heat sink. Since the thermal gradient is approximately constant, at a given current I, the temperature of the cell may be controlled in two ways, (1) by controlling the temperature of the coolant supplied to the thermoelectric modules and (2) by controlling the current supplied to the thermoelectric modules. As designed, the lowest temperature which could be achieved was approximately -35°C, which was not cold enough to induce the phase transition to ice II from either ice III or ice V.

In an attempt to induce the transition to ice II from a single crystal of ice III the temperature of the cell was reduced well below -35° C. The first attempt to reduce the temperature involved circulating a methanol/water coolant mixture through a container of cold nitrogen vapour produced by liquid nitrogen boil off. This, however, did not significantly reduce the temperature of the coolant and had little affect on the temperature

of the high pressure cell and sample. The coolant was then passed through a liquid nitrogen bath. This succeeded in reducing the temperature of the coolant, however it always resulted in the coolant freezing in the portion of the tube submerged in the nitrogen bath. As a result the current supplied to the thermal modules was automatically shut off to prevent overheating; the temperature of the high pressure cell increased and on several occasions the sample was almost lost.

The next attempt to reduce the sample temperature involved passing liquid nitrogen through a coiled tube submerged in the methanol/water coolant bath. This brought the temperature of the bath down to approximately  $-45^{\circ}\text{C}$ . The flow rate of the liquid nitrogen was closely monitored during the entire process. Subsequently the temperature of the high pressure cell was reduced to  $\sim -50^{\circ}\text{C}$ . This temperature was maintained for several days with no sign of an imminent phase transition.

In order to further reduce the temperature of the high pressure cell a system was designed so that cold nitrogen gas could be forced through the coils used as a heat exchanger with thermoelectric modules. During crystal growth the thermoelectric cooling system was used as before. When a single crystal of ice III had been produced the thermoelectric cooling system was shut down and the coolant tubes were used to carry the cold nitrogen gas which then directly cooled the high pressure cell. The thermal transfer between the fast moving nitrogen gas and the high pressure cell was not sufficient to reduce the temperature below  $-55^{\circ}\text{C}$ . As a result liquid nitrogen was passed through the tubes. The

temperature of the cell quickly dropped to approximately  $-75^{\circ}\text{C}$ . The rate of flow of liquid nitrogen was constantly monitored and manually adjusted in an attempt to maintain control of temperature fluctuations. The temperature was held between  $-70^{\circ}\text{C}$  and  $-80^{\circ}\text{C}$  for up to 18 hours.

A phase transition to ice II from a single crystal of ice III did occur, as evidenced through the microscope and video monitor. The ice II crystal was, however, not single and large amounts of oil had penetrated into the sample. It is evident that if single crystals of ice II are to be produced a more permanent automated liquid nitrogen temperature control system is needed. It may be possible to produce a single crystal of ice II by pressurizing ice Ih at temperatures between  $-80^{\circ}\text{C}$  and  $-100^{\circ}\text{C}$ . The slower reaction rate may cause the ice Ih to transform to ice II as a single crystal.

In addition to the problems encountered while trying to produce samples of various phases there were also many technical difficulties which had to be overcome. On one occasion the high pressure feed through (the coupling between the high pressure supply line inside and outside the plexiglass housing) developed a hairline fracture resulting in immediate loss of pressure. Such fractures were not visible to the naked eye and were extremely difficult to find. This problem was finally diagnosed by cleaning all excess oil from all high pressure tubes and fittings repressurizing the cell, as much as possible, while waiting for oil to visibly leak through the faulty component. The hairline fracture in the high pressure feed-through required that more maraging steel be purchased and

shipped to Memorial, a new high pressure feed through built in the local machine shop and then sent to be hardened. This caused a delay of close to two months. Numerous quartz windows developed small fractures and required replacement. Cracked windows often caused the window mounts to partially fill with oil, thus obscuring the view of the sample and making this particular problem easy to diagnose. Replacing broken windows, however, was difficult. It was crucial that the window mounts be kept almost perfectly flat so that when placed in contact with the quartz window a proper seal formed, thus preventing oil leaks (see chapter II). At one point the edge of the window mount accidentally chipped off removing with it a portion of the flat surface. Many unsuccessful attempts were made to create a seal between the window and the damaged mount. This process is complicated and time consuming since it was required that the high pressure cell be disassembled, the window replaced, the cell then reassembled and pressurized before it could be determined if an adequate seal had been made. Eventually, after several days, a successful seal was formed.

## **6.2 Results**

The present results of the elastic constants of ice III, ice V and ice VI are reported in Table 6.1 along with the respective temperatures and pressures. Note that the elastic constants common to ice III, V, and VI increase in each consecutively higher polymorph. The only exception is  $C_{44}$  which is slightly higher in ice V than in ice VI. These results represent the first experimental elastic constant values obtained from ice III and ice V and

**Table 6.1 Elastic Constants of ice III, ice V and ice VI**

	Ice III	Ice VI		Ice V
	P=2.2 kbar T=-20° C	P=7.2 kbar T=-2°C		P=3.0 kbar T=-35°C
$C_{11}$	$15.37 \pm 0.5$	$26.84 \pm 0.2$	$C_{11}$	$21.4 \pm 1.2$
$C_{33}$	$11.55 \pm 0.7$	$26.21 \pm 0.2$	$C_{22}$	$19.3 \pm 1.2$
$C_{44}$	$4.46 \pm 0.2$	$6.31 \pm 0.1$	$C_{33}$	$21.1 \pm 1.3$
$C_{66}$	$5.68 \pm 0.4$	$10.38 \pm 0.1$	$C_{44}$	$7.5 \pm 0.7$
$C_{12}$	$9.95 \pm 0.6$	$14.52 \pm 0.3$	$C_{55}$	$3.7 \pm 0.5$
$C_{13}$	$6.51 \pm 0.6$	$12.82 \pm 0.2$	$C_{66}$	$7.5 \pm 0.7$
			$C_{12}$	$12.2 \pm 1.2$
			$C_{13}$	$9.5 \pm 1.1$
			$C_{15}$	$0.17 \pm 0.4$
			$C_{23}$	$11.8 \pm 1.1$
			$C_{25}$	$-0.1 \pm 0.8$
			$C_{35}$	$-0.3 \pm 0.6$
			$C_{45}$	$-2.1 \pm 0.3$

the first experimental elastic constants of ice VI below 10.5 kbar. Ice VI elastic constants above 10.5 kbar were reported in a paper published in Physical Review B (Shimizu *et al.*<sup>77</sup>) while the paper reporting the present the elastic constants was in press. It is thought that the results of the present experiments, *i.e.* knowledge of the elastic constants of different phases of ice may be of importance in many areas of science and technology including the following:

1) The elastic constant results of the present study may be of significant value as a test of intermolecular potentials which model molecular bonding in liquid water and ice. As mentioned in Chapter I, there presently exists no one potential function which can accurately reproduce all the physical and chemical properties of all phases of water. The determination of accurate water-water interaction potentials is presently an active area of research in many laboratories throughout the world and the present results will contribute significantly to such efforts.

2) The elastic constants of ice III may also be of importance in certain ice engineering fields. Explosive loading of ice Ih may, under the proper temperature conditions, result in a phase transformation from ice Ih to ice III in the close proximity of the explosive charge. Such a phase transformation would result in significantly different elastic properties of ice and hence significantly different shockwave behaviour. The elastic constants of ice III would be required to fully understand and accurately model the results.

3) During collisions involving icy stellar bodies it is widely thought that phase transformations among the high pressure polymorphs of ice occur. Such collisions may involve the impact of comets with solar bodies such as the planet Jupiter. Knowledge of the elastic properties of the solids involved will lead to more fundamental understanding of the processes involved.

4) It is widely known that significant amounts of clathrate hydrates exist under pressure in many regions of the ocean floor. Such clathrates trap significant amounts of hydrocarbons and are of great interest to energy companies around the world. Knowledge of the elastic and molecular behaviour of ice under pressure may lead to significant advances in understanding and possible recovery of such hydrocarbons.

As mentioned in chapter V, ice VI is the most acoustically isotropic of the three phases studied in the present experiment. A high degree of elastic isotropy in ice VI has also been suggested by the experiments of Polian and Grimsditch mentioned in chapter III. Elastic properties of isotropic media depend only on two elastic constants. These elastic constants (see section 2.1.4) may be thought of as  $C_{66}$  and  $C_{44}$  with all others set to zero. The two transverse acoustic wave polarizations in an isotropic media are degenerate and depend only on the elastic constant  $C_{44}$  through the equation,  $V_{T1,2} = (C_{44}/\rho)^{1/2}$ . Equation 5.2 gives  $C_{44}$  as a function of pressure and shows that  $C_{44}$  is almost constant (slope  $\sim 0.04 \text{ m s}^{-1} \text{ kbar}^{-1}$ ). The transverse acoustic velocity is somewhat isotropic in the (010) plane (see Fig. 5.6), and is only degenerate in certain directions. Note that the average

transverse acoustic velocities given by Eq. 5.5, only increase slightly with pressure, exactly as expected from the above equation regarding transverse acoustic velocity in isotropic solids with nearly constant  $C_{44}$ .

Despite the structural similarity, Fig. 3.9 shows that ice III is less isotropic than ice VI with regard to both longitudinal and transverse acoustic polarizations. It is quite possible that the higher acoustic isotropy of ice VI may be due to non-hydrogen bonding between the two interpenetrating lattices which form the "self-clathrate" structure. There has been little work done toward determining the exact form of the interaction between the two interlocking lattices of ice VI. It now appears as though such an interaction may play a significant role in the acoustic properties of ice VI.

In conclusion, the present study may be nicely complemented by conducting additional Brillouin scattering studies of several high pressure polymorphs of ice. In particular, experiments should be conducted on single crystals of ice V at higher pressures and the results compared with those of the present studies. Experiments investigating the phase transition from ice VI to ice V could be conducted. Single crystals of ice VI could be depressurized and the acoustic properties measured through the transition to ice V. Elastic softening of the  $C_{44}$  elastic constant would be indicative of ferroelastic behaviour. If such experiments were conducted at temperatures between  $-40^{\circ}$  C and  $-60^{\circ}$  C the phase transition may proceed slowly resulting in a single crystal of ice V and better results.

In addition, experiments should be conducted to investigate the elastic properties of ice VI at higher pressures. There appears to be a slight discrepancy between the  $C_{66}$  elastic constant of Shimizu *et al.*<sup>77</sup> and the present value when extrapolated to 12.3 kbar. An experimental high pressure cell, similar to that used in the present study, may be used to grow large single crystals ice VI at pressures above 10 kbar. Elastic constants values obtained from large crystals would indicate if the small crystal size of Shimizu's sample affected the results. As with the present work, such experiments would be very interesting and contribute greatly to our overall understanding of water.

## References

1. D. Eisenberg and W. Kaumann, *The Structure and Properties of Water*, Oxford Press, 1969.
2. F. Franks, *Water*, The Royal Society London (1983).
3. P. Flubacher, A.J. Leadbetter and J.A. Morrison, *J. Chem. Phys.*, **33**, 1751 (1960).
4. D.C. Ginnings and R.J. Corruccini, *J. Res. Natn. Bur. Stand.*, **38**, 583 (1947).
5. G.A. Jeffery and R.K. McMullan, *Prog. Inorg. Chem.*, **8**, 43-108.
6. T. Owen, In *Physics and Chemistry of Ice*, E. Whalley, S.J. Jones and L.W. Gold Eds. (Royal Society of Canada, Ottawa 1973) pp. 117-126.
7. P.H. Hepburn, *J. Br. Assoc.*, **33**, 244 (1923).
8. R.N. Clarke and P.D. Owensby, *Icarus*, **46**, 354 (1981).
9. D. Morrison, D.P. Cruikshank, C.B. Pilcher and G.H. Rieke, *Astron. J.*, **207**, 213 (1976).

10. U. Fink, H.P. Larson, T.N. Gautier and R.R. Trefers, *Astroph. J.*, **207**, 63 (1976).
11. D.M. Janes and S.W. Squyres, In *Physics and Chemistry of Ice*, N. Maeno, T. Hondoh Eds. (Hokkaido University Press, 1992). pp. 219-224.
12. H. Kieffer, *Science*, **194**, 1341 (1976).
13. H. Kieffer, *J. Geophys. Res.*, **84**, 8263 (1979).
14. J.M. Greenberg, In *Comets*, L.L. Wilkening, Ed. (University of Arizona Press, Tucson, 1982) pp. 131-163.
15. A.G.G.M. Tielens, In *Interstellar Dust*, L.J. Allamandola and A.G.G.M. Tielens, Eds. (Kluwer, Dordrecht, 1989) pp. 239-262.
16. D. Blake, L. Allamandola, S. Sandford, D. Hudgins and F. Freund, *Science*, **254**, 548 (1991).
17. F.L. Whipple, *Astrophys. J.*, **111**, 375 (1950).
18. J. Klinger, *Science*, **209**, 271 (1980).
19. H. Patashnick, G. Rupprecht and D.W. Schuerman, *Nature*, **250**, 313 (1974).

20. N. H. Fletcher, *The Physics and Chemistry of Ice*, (Cambridge University Press, 1970) pp. 38-49.
21. K. M. Van De Graaff and S.I. Fox, *Concepts of Human Anatomy and Physiology* (Wm. C. Brown Publishers, 1992) pp. 44-45, 58-63.
22. H.C. Anderson, *J. Chem. Phys.*, **72**, 2384 (1980).
23. M. Parrinello and A. Rahman, *Phys. Rev. Lett.*, **45**, 1196 (1980).
24. C. Lee, D. Vanderbilt, K. Laasonen, R. Car and M. Parrinello, *Phys. Rev. B*, **47**, 4863 (1993).
25. L. Ojamäe, K. Hermansson, R. Dovesi, C. Roetti and V.R. Saunders, *J. Chem. Phys.*, **100**, 2128 (1994).
26. J.R. Reimers, R.O. Watts and M.L. Klein, *Chemical Physics*, **64**, 95 (1982).
27. W.L. Jorgenson, J. Chandrasekhar, J.D. Mandura, R.W. Impey and M.L. Klein, *J. Chem. Phys.*, **79**, 926 (1983).
28. R. W. Impey, M.L. Klein and J.S. Tse, *J. Chem. Phys.*, **81**, (1984).

29. W.L. Jorgensen, *J. Chem. Phys.*, **77**, 4156 (1982).
30. J. S. Tse and D.D. Klug, *Phys. Rev. Lett.*, **70**, 174 (1993).
31. R.E. Gagnon, H. Kieft, M.J. Clouter and E. Whalley, *J. Chem. Phys.*, **92**, 1909 (1990).
32. D.M. Bishop and M. Randic, *Molec. Phys.*, **10**, 517 (1966).
33. R. Moccia, *J. Chem. Phys.*, **40**, 2186 (1964).
34. F.O. Ellison and H. Shull, *J. Chem. Phys.*, **23**, 2348 (1955).
35. J.A. Pople, *Proc. Roy. Soc. Lond.*, **A202**, 323, (1950).
36. R. McWeeny and K.A. Ohno, *Proc. Roy. Soc. Lond.*, **A255**, 367 (1960).
37. W.S. Benedict, N. Gailar and E.K. Plyler, *J. Chem. Phys.*, **24**, 1139 (1956).
38. A.B.F. Duncan and J.A. Pople, *Trans. Faraday Soc.*, **49**, 217 (1953).
39. S.J. La Placa and B. Post, *Acta Crystallogr.*, **13**, 503 (1960).

40. R. Brill and A. Tippe, *Acta Crystallogr.*, **23**, 343 (1967).
41. S.W. Peterson and H.A. Levy, *Acta Crystallr.*, **10**, 70 (1957).
42. L. Pauling, *J. Am. Chem. Soc.*, **57**, 2680 (1935).
43. A. Polian and M. Grimsditch, *Phys. Rev. Lett.*, **52**, 1312 (1984).
44. J.D. Bernal and R.H. Fowler, *J. Chem. Phys.*, **1**, 515, (1933).
45. S.W. Peterson and H.A. Levy, *Acta Crystallogr.*, **10**, 70 (1957).
46. P. Hobbs, *Ice Physics*, Clarendon Press, Oxford Press, 1974.
47. K.R. Hirsch and W.B. Holzappel, *Physics Letters.*, **101A**, 142 (1984).
48. K.R. Hirsch and W.B. Holzappel, *J. Chem. Phys.*, **84**, 2771 (1986).
49. K.S. Schweizer and F.H. Stillinger, *J. Chem. Phys.*, **80**, 1230 (1984).

50. Ph. Pruzan, *J. Mol. Struct.*, **322**, 279, (1994).
51. O. Mishima, L.D. Calvert and E. Whalley, *Nature*, **310**, 393 (1984).
52. M.A. Floriano, E. Whalley, E.C. Svensson, and V.F. Sears, *Phys. Rev. Lett.*, **57**, 3062 (1986).
53. Y.P. Handa, O. Mishima and E. Whalley, *J. Chem. Phys.*, **84**, 2766 (1986).
54. J.S. Tse and D.D. Klug, *Can. J. Phys.*, **73**, 253 (1995).
55. J.A. Ghormley and C.J. Hochanandel, *Science*, **171**, 62 (1971).
56. E. Mayer and P. Bruggeller, *Nature*, **298**, 715 (1982).
57. J. Dubochet and A.W. McDowell, *J. Microsc.*, **124**, RP3 (1981).
58. G. Tammann, *Annl. phys.*, **2**, 1 (1900).
59. P.W. Bridgman, *Proc. Am. Acad. Arts Sci.*, **47**, 441 (1912).
60. P.W. Bridgman, *Proc. Am. Acad. Arts Sci.*, **48**, 309 (1912).

61. P.W. Bridgman, *J. Chem. Phys.*, **3**, 597 (1935).
62. P.W. Bridgman, *J. Chem. Phys.*, **5**, 964 (1937).
63. R.L. McFarlan, *J. Chem. Phys.*, **4**, 60 (1936).
64. W.B. Kamb and S. K. Datta, *Nature*, **187**, 140 (1960).
65. J.E. Bertie and E. Whalley, *J. Chem. Phys.*, **40**, 1646 (1964).
66. M. J. Tayler and E. Whalley, *J. Chem. Phys.*, **40**, 1660 (1964).
67. G.J. Wilson, R. K. Chan, D.W. Davidson, and E. Whalley, *J. Chem. Phys.*, **43**, 2384 (1965).
68. E. Whalley, J.B.R. Heath and D.W. Davidson, *J. Chem. Phys.*, **48**, 2362 (1968).
69. W.C. Hamilton, B. Kamb, S.J. Laplaca and A. Prakash, In *Physics of Ice*, N. Riehl, B. Bullemer, and H. Engelhardt Eds. (Plenum Pres, New York 1969). pp. 44-58.
70. G.H. Shaw, *J. Chem. Phys.*, **84**, 5862 (1986).

71. B. Kamb, *Science*, **150**, 205 (1965).
72. J.E. Bertie, L.D. Calvert and E. Whalley, *J. Chem. Phys.*, **38**, 840 (1963).
73. J.E. Bertie, H.J. Labbé, and E. Whalley, *J. Chem. Phys.*, **49**, 2141 (1969).
74. E. Whalley, In *Physics of Ice*, N. Riehl, B. Bullemer and H. Engelhardt, Eds. (Plenum Press, New York 1969) pp. 19-43.
75. G. P. Johari and E. Whalley, *J. Chem. Phys.*, **70**, 2094 (1979).
76. A. Polian and M. Grimsditch, *Phys. Rev. B*, **27**, 6409 (1983).
77. H. Shimizu, T. Nabetani, T Nishiba and S. Sasaki, *Phys. Rev. B*, **53**, 6107 (1996).
78. J.F. Nye, *Physical Properties of Crystals*, (Clarendon Press, Oxford, 1957).
79. L.D. Landau and E.M. Lifshitz, *Theory of Elasticity*, (Pergamon, Oxford, 1970).
80. H.B. Huntington, *The Elastic Constants of Crystals*, (Academic Press, New York, 1958).
81. M.J.P. Musgrave, *Crystal Acoustics*, (Holden-Day, San Francisco, 1970).

82. M.J.P. Musgrave, *Proc. Roy. Soc., A* **226**, 339 (1954).
83. A.G. Every, *Phys. Rev. B*, **22**, 1746 (1980).
84. W. Voigt, *Lehrbuch der Kristallphysik* (Teubner, Leipzig, 1910).
85. A. Reuss, *Z. Angew. Math Mech.*, **9**, 55 (1929).
86. P.L. Gould, *Introduction to Linear Elasticity*, (Springer-Verlag, New York, 1983).
87. W. Hayes, *Contemp. Phys.*, **16**, 69 (1975).
88. L. Brillouin, *Ann. Phys.*, **17**, 88 (1922).
89. L.I. Mandelshtam, *Zh. Russ. Fiz. Khim. Ova.*, **58**, 381 (1926).
90. M. Born and K. Huang, *Dynamical Theory of Crystal Lattices*, (Clarendon, Oxford, 1954).
91. H.Z. Cummins, P.E. Schoen, In *Laser Handbook*, Eds. F.T. Arecchi and E.O. Schultz-dubois (North Holland, Amsterdam, 1972) Vol. II p. 1030.
92. G.B. Benedek and K. Fritsch, *Phys. Rev.*, **149**, 647 (1966).

93. D.F. Nelson, P.D. Lazay, and M. Lax, *Phys. Rev. B*, **6**, 3109 (1972).
94. E. Gross, *Nature*, **129**, 722 (1932).
95. R.S. Krishnan, *Proc. Ind. Acad.*, **A41**, 91 (1955).
96. J.R. Sandercock, In *Light Scattering in Solids III*, Eds. M. Cardona and G. Güntherodt, (Springer-Verlag, 1982) pp. 173-206.
97. H. Shimizu, E.M. Brody, H.K. Mao and P.M. Bell, *Phys. Rev. Lett.*, **47**, 128 (1981).
98. C.H. Whitfield, E.M. Brody and W.A. Basset, *Rev. Sci. Instrum.*, **47**, 942 (1976).
99. M. Krishnamurthi and M. Suryanarayana, In *Physics of the Solid State*, (Academic Press, London, 1969) pp. 487-509.
100. A. Griffin, *Rev. Mod. Phys.*, **40**, 167 (1968).
101. H. Kiefte and M.J. Clouter, *J. Chem. Phys.*, **62**, 4780 (1975).
102. H. Kiefte and M.J. Clouter, *J. Chem. Phys.*, **64**, 1816 (1976).
103. P.H. Gammon, H. Kiefte and M.J. Clouter, *J. Chem. Phys.*, **70**, 810 (1978).

104. S.F. Ahmad, H. Kiefte and M.J. Clouter, *J. Chem. Phys.*, **69**, 5468 (1978).
105. R.E Gagnon, H. Kiefte, M.J. Clouter and E. Whalley, *J. Chem. Phys.*, **89**, 4522 (1988).
106. J.M. Vaughan, *The Fabry-Perot Interferometer*, (Adam Hilger, Bristol, 1989).
107. E. Hecht, *Optics*, (Addison-Wesley Publishing Co., Reading Massachusetts, 1987).
108. W.H. Press, B.P. Flannery, S.A. Teukolsky and W.T. Vetterling, *Numerical Recipes: The Art of Scientific Computing*, (Cambridge University Press, Cambridge, 1986).
109. K. Vedam and P. Limsuwan, *J. Chem. Phys.*, **69**, 4762 (1978).
110. H. Goldstein, *Classical Mechanics* (Addison-Wesley Publishing Co., Reading Massachusetts, 1980).
111. G. Arfken, *Mathematical Methods for Physicists* (Academic Press, San Diego, 1985).
112. R.E. Stoiber, A. Morse, *Microscopic Identification of Crystals* (Ronald Press Co., New York, 1972).
113. N.H. Hartshorne, A. Stuart, *Practical Optical Crystallography*, (American Elsevier Publishing Co., New York, 1969).

114. P. Gay, *An Introduction to Crystal Optics*, (Longmans, Green and Sons, London, 1967).

115. E.E. Wahlstrom, *Optical Crystallography*, (John Willey and Sons, New York, 1960).

116. F.A. Jenkins and H.E. White, *Fundamentals of Optics*, (McGraw-Hill, New York, 1957).

117 A.J. Krupnyi, V.V. Alchikov, K.S. Aleksandrov, *Kristallografiya*, **16**, 801 (1971).

118 V.F. Teslenko, A.P. Ryzhenkov, T.V. Ryzhova, K.S. Aleksandrov, A.I. Kitaigorodski, *Kristallografiya*, **10**, 895 (1965).

# Appendix A

## Extinction Angle Measurements of Ice V

Orientation of optically biaxial crystals by birefringence techniques similar to those discussed in chapter IV is greatly complicated by the presence of two optic axes. Further complications are introduced when the exact orientation of the two optic axes in the crystallographic frame of reference is not known. Measurements of the extinction angles in single crystals of ice V were obtained in the present study; however, due to the difficulties discussed in chapter IV these measurements were not used in the analysis of the acoustic data. It is, nevertheless, thought that this data is useful, and that more specific experiments may be developed which attempt to orient biaxial crystals using birefringence data. Such an experiment may include the design of a unique apparatus to obtain extinction angle measurements from biaxial crystals of known orientation and hence the development of a reliable method of data analysis. The birefringence data collected in the present study is therefore presented in table A1 and plotted in Fig. A1. The smooth curves in Fig. A1 were found using the Biot-Fresnel law. The set of best fit polar angles (which may be related to the optic axes) are;  $\theta_1=103.9^\circ$ ,  $\theta_2=151.9^\circ$ ,  $\phi_1=199.7^\circ$  and  $\phi_2=149.1$  for crystal #1;  $\theta_1=14.1^\circ$ ,  $\theta_2=-62.8^\circ$ ,  $\phi_1=50.6$  and  $\phi_2=-1.49^\circ$  for crystal #2; and  $\theta_1=169.2^\circ$ ,  $\theta_2=57.7^\circ$ ,  $\phi_1=-10.1^\circ$  and  $\phi_2=136.8^\circ$  for crystal #3.

**Table A1****Extinction Angle Versus Crystal Orientation Data  
Ice V**

Crystal #1	$\Delta\phi$ (degrees)	Cos(extinction angle)
1	0	-0.6915
2	20	-0.7518
3	50	-0.6327
4	80	0.1132
5	110	0.4482
6	140	0.5577
7	170	0.6211
8	200	0.6871
9	230	0.6225
10	360	-0.6915
11	380	-0.7518
12	410	-0.6327
<b>Crystal #2</b>		
1	20	-0.3649
2	80	-0.2965
3	100	0.0981
4	130	0.2377
5	160	0.3665
6	180	0.4147
7	210	0.4286
8	230	0.3786
9	260	0.2672
10	290	-0.1023
11	320	-0.2869
12	350	-0.3288
<b>Crystal #3</b>		
1	30	-0.3649
2	50	-0.3746
3	80	-0.3486
4	110	-0.3123
5	140	-0.0035
6	170	0.2011

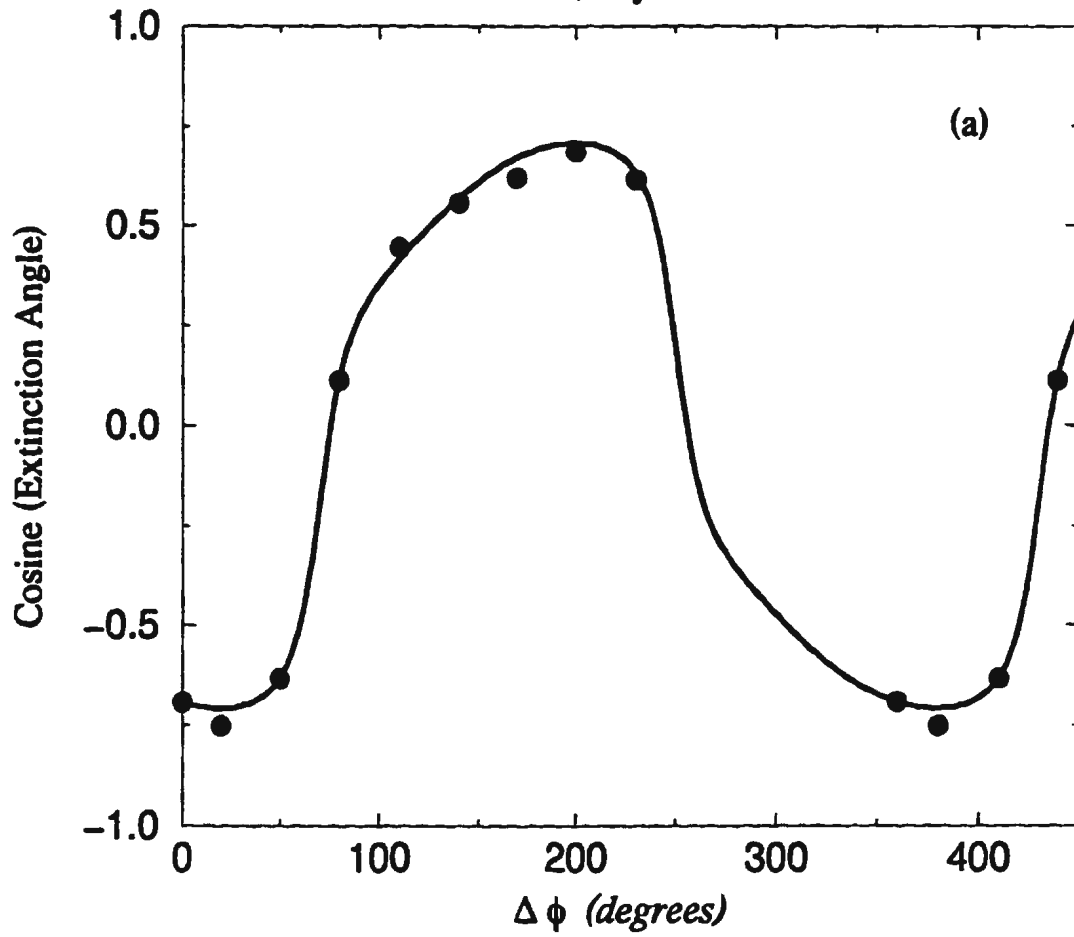
7	200	0.2974
8	230	0.3502
9	260	0.3272
10	290	0.2740
11	320	-0.0819
12	350	-0.2940

**Figure A1 Extinction Angle versus  $\Delta\phi$**

Plots showing the birefringent extinction angles collected from single crystal samples of ice V. The solid circles represent experimental data and the smooth curves are best fits using the Biot-Fresnel law, see chapter IV.

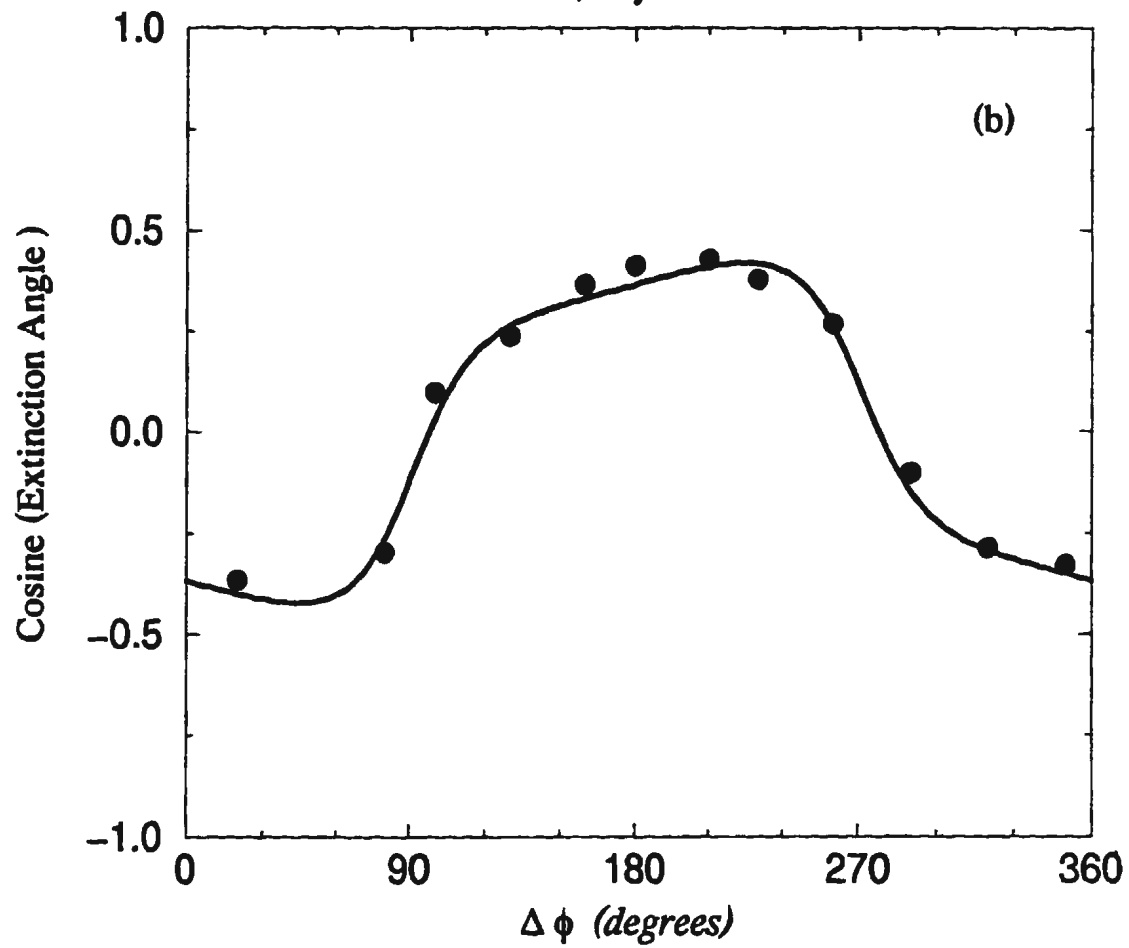
# Orientation Data

IceV, Crystal #1



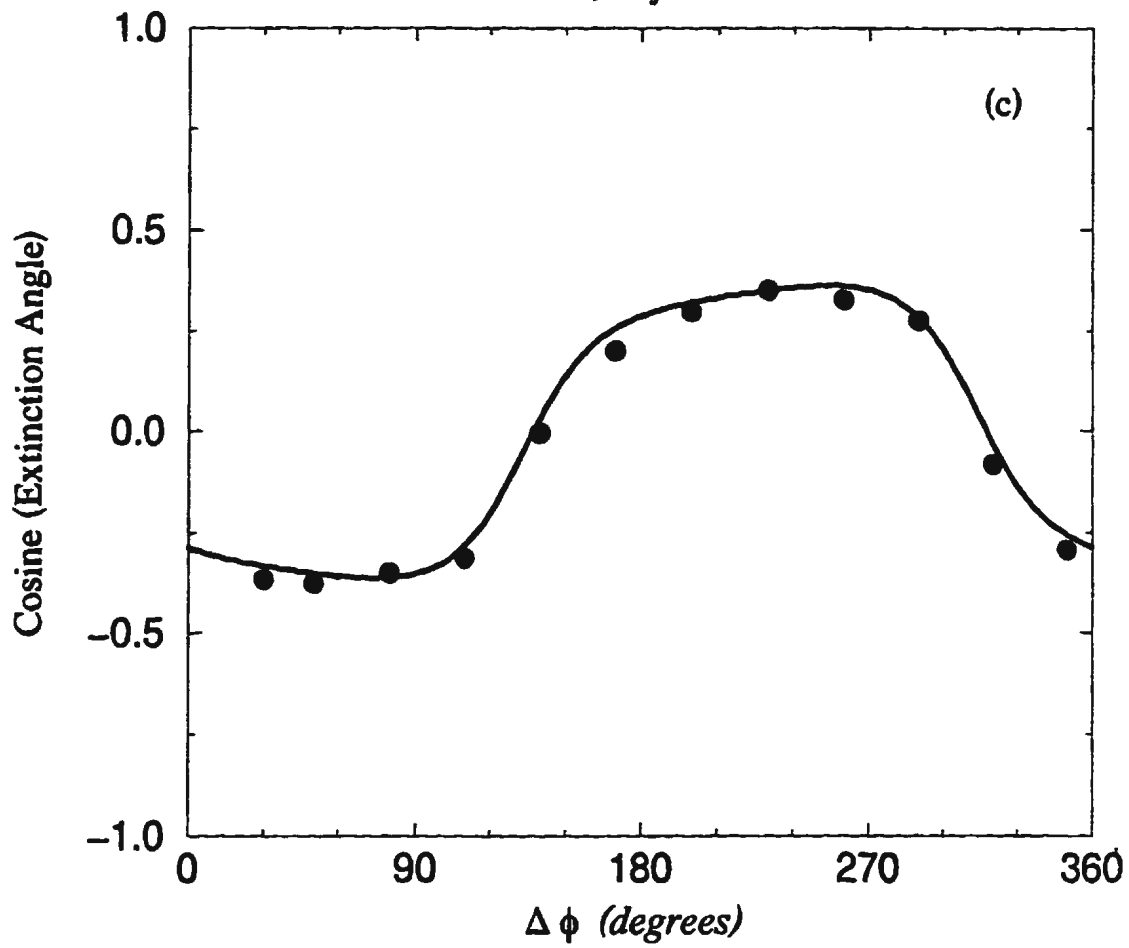
# Orientation Data

IceV, Crystal #2



# Orientation Data

IceV, Crystal #3



# Appendix B

## Neutron Scattering Studies of Excess Low Frequency Excitations in Ice

### B.1 Introduction

Vibrational spectra of crystalline and amorphous forms of the same substance show the greatest difference in the low frequency portion of the spectrum. Amorphous phases exhibit an excess of low energy states, *i.e.* the density of states exceeds that predicted by the Debye model which can be used to describe the low temperature behaviour of crystalline solids. These excess low frequency vibrations also serve to increase the low temperature specific heat in amorphous solids<sup>B1</sup> including incommensurate dielectrics.<sup>B2</sup> In the case of vitreous silica the excitations have been studied by inelastic neutron scattering and have been attributed to a relative rotation of the SiO<sub>4</sub> tetrahedra.<sup>B3,B4</sup> Other authors conclude, based on inelastic neutron scattering experiments used to obtain the density of states  $g(\nu)$ , that amorphous solids should be considered over a certain scaling range to be fractal systems.<sup>B5</sup> The vibrational spectrum of a glass formed by soft spheres has been investigated by computer simulation.<sup>B6</sup> The simulation showed the existence of localized (or quasi-localized) modes in the low frequency part of the spectrum. The modes form around atoms whose local environment differs significantly from the surrounding amorphous materials. Therefore the modes may form due to some weak interaction arising from regions in the solid which have a higher than average coordination number. The precise cause of the excess low frequency modes

is still a matter of great debate.

It has, however, been suggested that the general form of the low energy vibrational spectrum of vitreous solids is universal. When the low energy spectra, determined by inelastic neutron scattering, of  $\text{SiO}_2$ ,  $\text{As}_2\text{S}_3$  and the metallic glass  $\text{Mg}_{70}\text{Zn}_{30}$  are scaled in energy by  $E_{\text{max}}$  and plotted on the same graph it becomes evident that the peak shape is identical for all three materials in spite of the marked difference in structure.<sup>B7</sup> In addition the excess low frequency modes may also increase the mean square atomic displacement from that of the crystalline form of the same material.<sup>B8</sup>

## ***B.2 Inelastic Incoherent Neutron Scattering Experiments***

The author has spent 2 months at the Atomic Energy of Canada/Chalk River laboratories conducting experiments which investigate excess low frequency excitations in ice. A brief discussion of the experiment is given below.

As high density amorphous (hda) ice is heated from liquid nitrogen temperature it undergoes a phase transition at  $\sim 119$  K to another form of amorphous ice of lower density (lda), which is also metastable at low temperatures. Upon further heating lda transforms at  $\sim 145$  K to a cubic crystalline phase ice Ic (see Table 1.1), also metastable at low temperature. Ice Ic transforms to stable ice Ih at  $\sim 225$  K. Therefore ice provides an excellent substance for the study of the temperature dependence of the low frequency excitation which can be easily compared with spectra of the crystalline phases collected

from the same sample. The goal of the present study is to measure the temperature dependence of the excess low frequency modes through the density of phonon states,  $g(\nu)$ , in high density amorphous (hda) and low density amorphous ice (lda) and to compare the results with  $g(\nu)$  measurements of the two crystalline polymorphs, ice Ic and ice Ih. Measurements of  $g(\nu)$  have been made from the amorphous phases of ice in the frequency range 0-30 THz (*i.e.* from the elastic peak out to the libration bands).<sup>B9</sup> Separate studies of the low frequency excitation in amorphous ice indicate that the excess low frequency modes disappear as the temperature is raised.<sup>B10</sup> Measurements were made from hda and crystalline ice Ih samples at 11 K and at 80 K. The energy resolution at the elastic peak was 0.05 THz with momentum transfer  $Q=2.5 \text{ \AA}^{-1}$ . The spectrum was collected across the elastic peak and covered the transverse acoustic mode,  $-0.10 \leq \nu \leq 3.66 \text{ THz}$ . The spectra collected at 11 K exhibited excess low frequency modes and the measurements at 80 K indicate that the excess modes have essentially disappeared. A detailed study of the disappearance of the low frequency modes with increasing temperature was thus required.

In the present study, which is not yet complete, samples of hda H<sub>2</sub>O ice were made at NRC/Steacie Institute for Molecular Sciences in Ottawa by pressurizing ice Ih at 77 K to 13 Kbar. The sample was a thin disk of 69.5 mm in diameter by 2 mm thick. It was held at liquid nitrogen temperature and transferred to Chalk River Laboratories. Inelastic incoherent neutron scattering data were collected from four polymorphs of ice at atmospheric pressure in the temperature range 5 - 120 K. Spectra were collected from

each phase at  $T = 5\text{K}, 20\text{K}, 40\text{K}, 60\text{K}, 80\text{K}$  and  $120\text{K}$  using the N5 triple axes spectrometer at Chalk River Laboratories in collaboration with E. Svensson, J. Katsaras from AECL and D.D. Klug and J. Tse from NRC/Steacie Institute for Molecular Sciences. The instrumental resolution was  $\sim 0.05$  THz at  $\nu = 0$ . The scattered neutrons were collected at constant momentum transfer  $Q \approx 2.5 \text{ \AA}$  in the frequency range  $-0.12 \leq \nu \leq 4.1$  THz. The frequency interval was set to include the elastic and transverse acoustic peak, however, since only a small region  $0.14 \leq \nu \leq 1.02$  THz sufficiently covers the portion of the spectrum containing the excess modes, shorter scans were set to repeatedly cover this region. This considerably increased statistical accuracy.

The room background radiation, neutron flux inhomogeneity of the beam cross-section and empty cell scattering will be subtracted from the raw scattered intensity and  $g(\nu)$  will be calculated and include corrections for multiphonon and multiple scattering. This will enable comparison of the spectra collected at different temperatures and between different polymorphs. It is quite evident from cursory inspection of the raw data (see Fig. B1), that the excess vibrational modes in hda are strongly temperature dependent. The intensity of the excess modes drop off significantly as the temperature is raised to 80 K. Low density amorphous ice also exhibits excess low frequency modes between 5 K and 80 K but, in contrast to hda, they are much less pronounced. The temperature dependence of the excess modes can be seen in the raw data and is shown in Fig. B2. As the temperature increases the "hump" which indicates the excess modes seems to disappear. The overall intensity of this region of the spectrum increases due to an increase in thermal phonon population.

As expected the two crystalline forms exhibit no excess modes in the temperature range. The neutron spectrum of lda ice resembles the crystalline phases (the transverse acoustic peak is less broad and there is less evidence of low frequency excitations even at 5K) this indicates that there may be a great deal of structure inherent in the lda phase. It must be noted that the  $g(v)$  calculations have not yet been performed and the above statements are merely conjecture based on the general form of the scattered neutron intensity data. It is, however, clear that any potential used to describe the interaction responsible for creating such excess modes will have to be weak causing low frequency oscillations which are strongly temperature dependent.

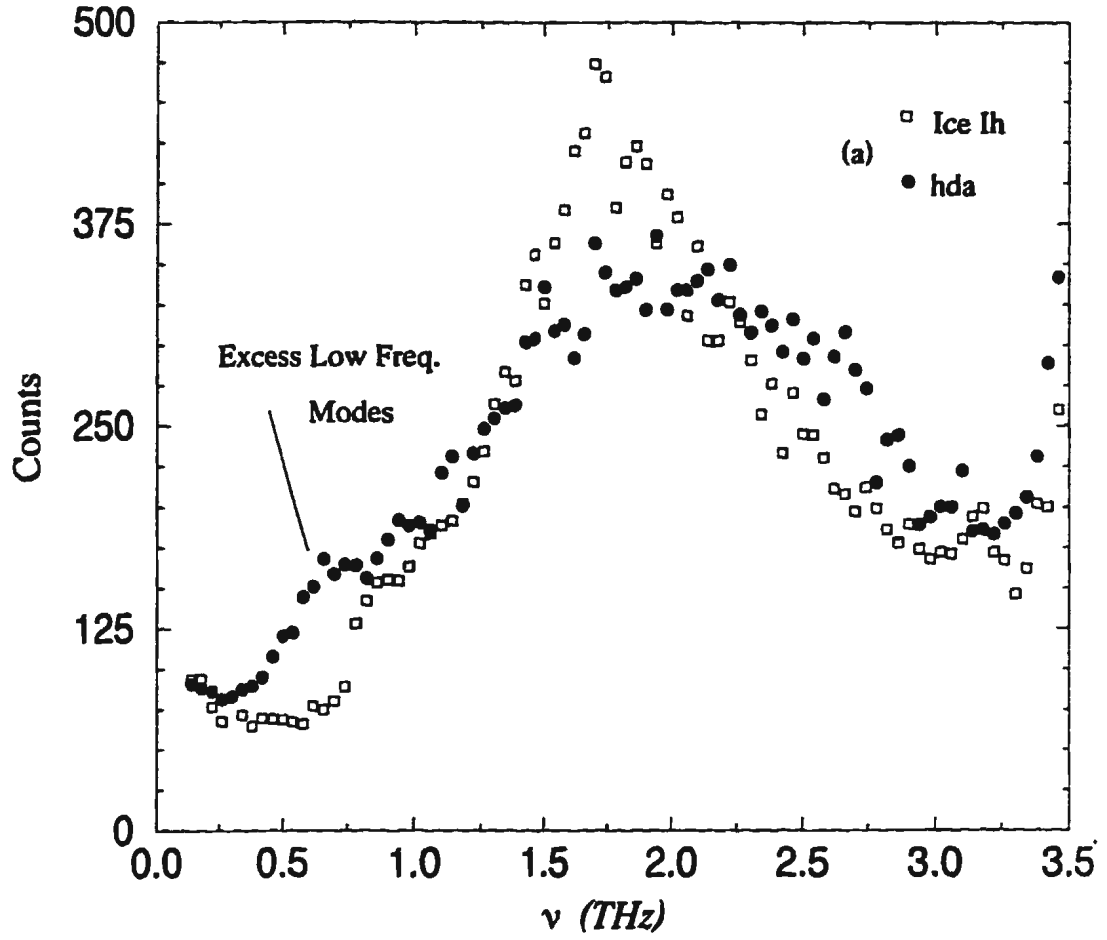
2

**Figure B1 Neutron Scattering Data, Transverse Acoustic Peak.**

Complete scan of the transverse acoustic peak; (a) compares ice Ih with hda at 5K, notice that the hda transverse acoustic mode is much broader than the crystalline phase and the excess low frequency modes are quite evident at 5K; (b) compares ice Ih with lda at 5K, notice that the lda peak resembles the ice Ih peak in width and the excess low frequency modes are much less pronounced.

# Transverse Acoustic Peak

hda and Ice Ih



# Transverse Acoustic Peak

Ida and Ice Ih

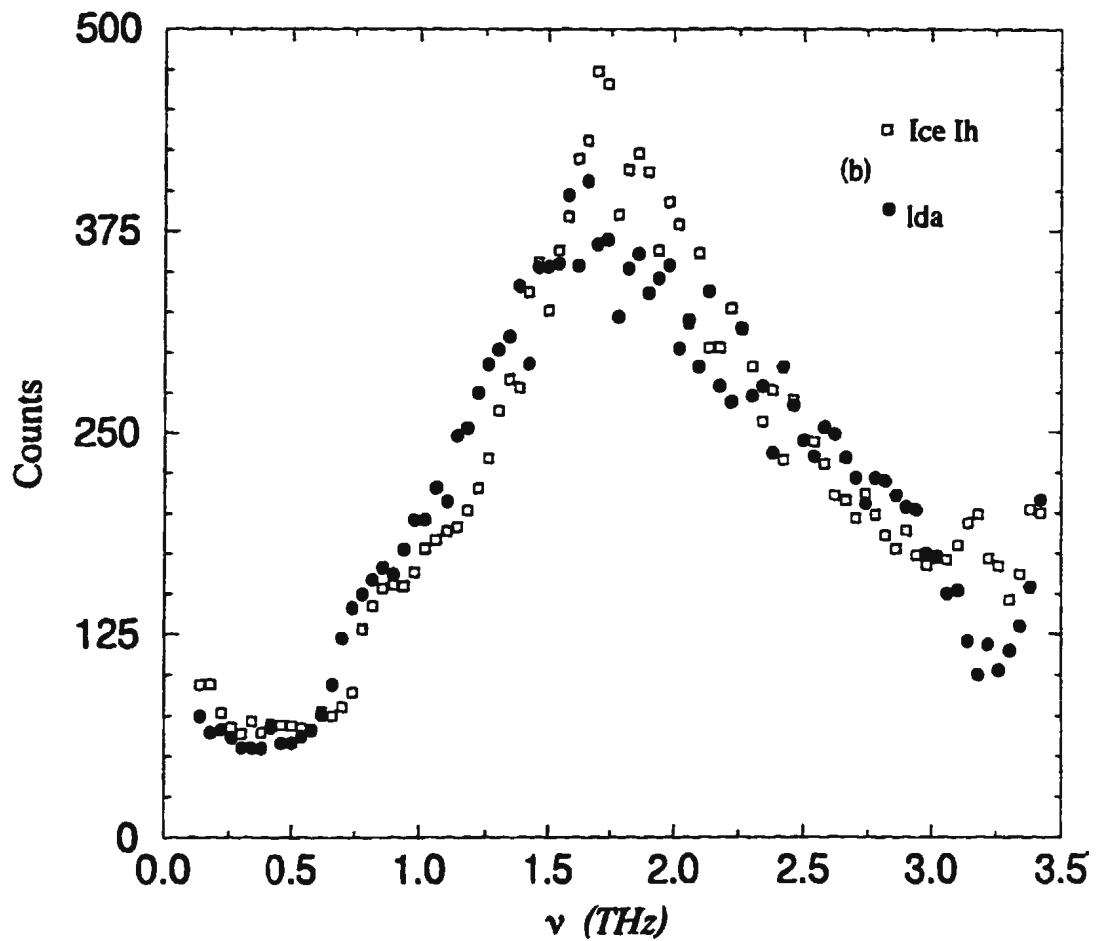
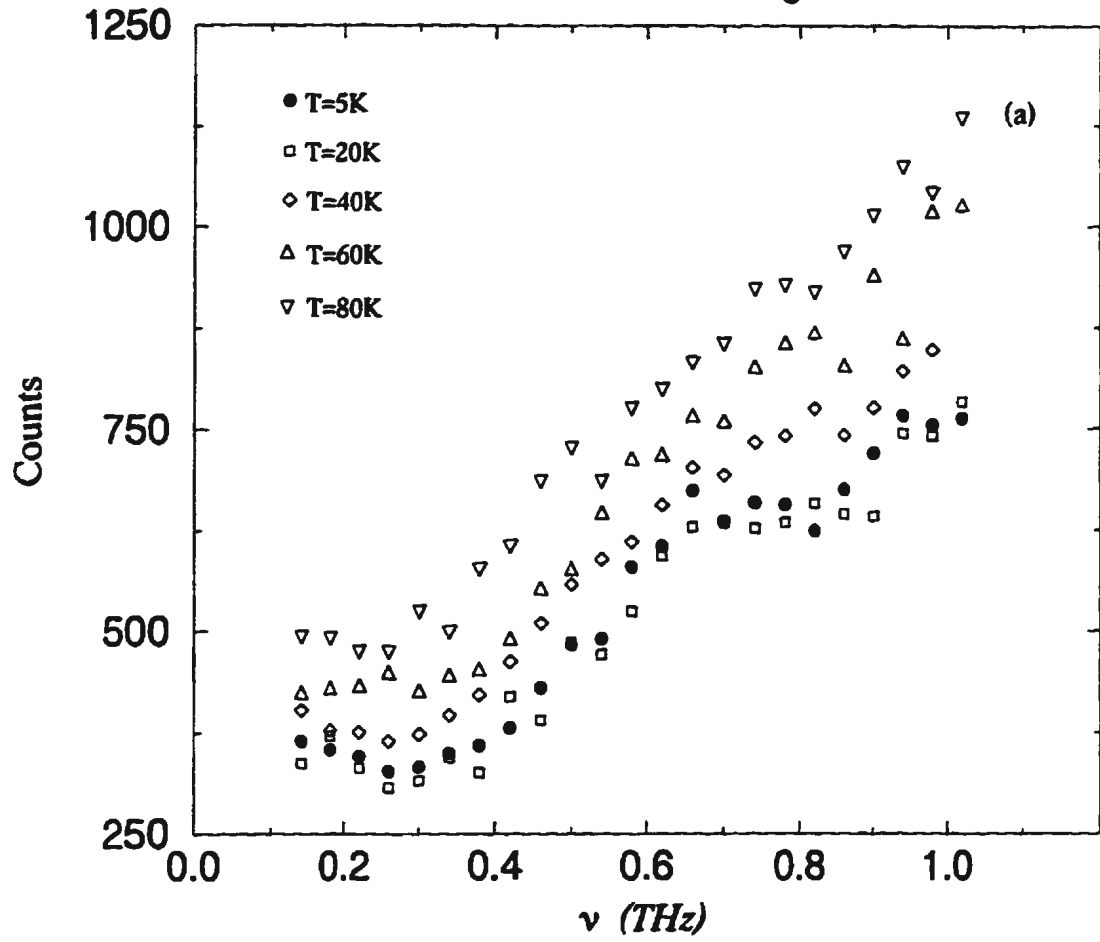


## **Figure B2 Excess Low Frequency Modes**

**Excess low frequency modes with temperature in the spectral region of interest, (a) illustrates hda ice, (b) illustrates lda ice. The excess modes are very well pronounced in hda at 5 K, however, as the temperature is raised the modes tend to disappear. The excess modes are much less pronounced in lda ice at 5 K and are totally gone at 120K. Note that the overall intensity increases with temperature due to the higher thermal population of phonons at higher temperatures.**

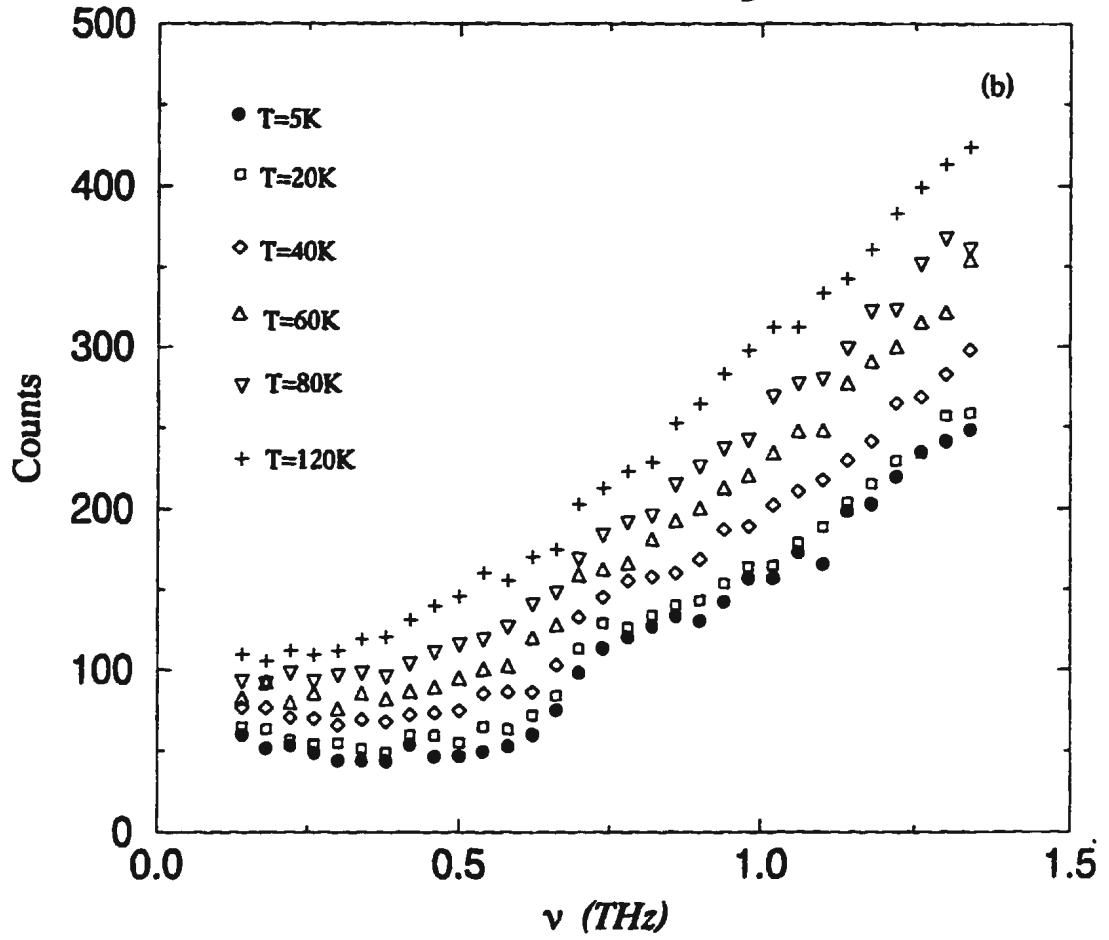
# Transverse Acoustic Peak

hda, Excess Mode Region



# Transverse Acoustic Peak

Ida, Excess Mode Region



## **References**

- B1. R.C. Zeller and R.O. Pohl, *Phys. Rev. B*, **4**, 2029 (1971).
- B2. J. Etrillard, J.C. Lasjaunias, K. Biljakovic, B. Toudic and G. Coddens, *Phys. Rev. Lett.*, **2334** (1996).
- B3. U. Buchenau, N. Nücker and A.J. Dianoux, *Phys. Rev. Lett.*, **53**, 2316 (1984).
- B4. U. Buchenau, M. Prager, N. Nücker, A.J. Dianoux, N. Ahmad, W.A. Phillips, *Phys. Rev. B*, **34**, 5665 (1986).
- B5. A.J. Dianoux, J.N. Page and H.M. Rosenberg, *Phys. Rev. Lett.*, **58**, 886 (1987).
- B6. H.R. Schober and B.B. Laird, *Phys. Rev. B*, **44**, 6746 (1991).
- B7. V.K. Malinovsky, V.N. Novikov, P.P. Parshin, A.P. Sokolov and M.G. Zemlyanov, *Europhys. Lett.*, **11**, 43 (1990).
- B8. V. K. Malinovsky and V.N. Novikov, *J. Phys. Condens. Matter*, **4**, L139, (1992).
- B9. D.D. Klug, E. Whalley, E.C. Svensson, J.H. Root and V.F. Sears, *Phys. Rev. B*, **44**, 841 (1991).

**B10. E.C. Svensson, W. Montfrooij, V.F. Sears and D.D. Klug, *Physica B*, 194-196, 409 (1994).**







